UPPSALA UNIVERSITY
Department of Radiation Sciences
Box 535, S-751 21 Uppsala, Sweden
http://www.tsl.uu.se/

Internal report

ISV-6/97
August 1996

Theoretical Investigations of Tomographic Methods used for Determination of the Integrity of Spent BWR Nuclear Fuel

S. Jacobsson[1]

Dept. of Radiation Sciences, Uppsala University, Box 535, S-751 21 Uppsala, Sweden

Abstract: Tomographic reconstructions of the activity distribution within nuclear fuel assemblies have been accomplished from simulated gamma-ray intensity patterns. The possibilities of detecting a missing fuel rod in the inner parts of an assembly have been examined. Three algebraic reconstruction algorithms have been tested. The algorithms rely on contribution coefficients, depending on attenuation and geometric conditions, describing to what extent emitted gamma-rays from each picture element reaches the detector in various positions. Methods of determining the contribution coefficients have been described. Various measurement strategies have been examined. The removal of a fuel rod might imply replacement by some other material. It has been shown that the detection of a missing rod is complicated due to the fact that attenuation of fuel will be assumed in that position, since the removal is to be considered unknown. The reconstructions indicate that the detection of a missing rod in the inner parts of an assembly should be possible.

[1] staffan.jacobsson@tsl.uu.se

Table of contents

1. Introduction

In all the nuclear power plants around the world, high-level radioactive waste is produced. In Sweden the purpose is to store the waste in capsules several hundred meters down in the ground. There the radioactivity will decrease during thousands of years until it has reached about the same level as the background activity. Since the radioactive waste is such a hazard to the environment it is very important that no part of it is left outside the storage system. Therefore a survey equipment is planned, making possible to control if the fuel assemblies are intact. There are several possible scenarios behind the removal of nuclear fuel rods:

-Removal of damaged or heavily burned out rods is in accordance with normal operation. Such removals are normally accurately declared, and are in general of no concern in this context. However, there exists a small risk that the information about such a reconstruction might be lost.

-Another possible scenario is malicious intents of stealing radioactive waste, maybe to make nuclear explosives of it. In this case no external information of missing rods can be expected, and one has to rely on adequate measurements on the fuel assembly.

The different scenarios cause different circumstances for the detection of missing rods. If a rod is removed and not replaced by fuel-like material, a change of weight of the assembly will occur. If just one rod out of 63 is missing (a typical BWR fuel assembly is described in section 2.1), the change of weight can be hard to detect, but not impossible. If, on the other hand, a rod is removed due to malicious intents it will most likely be replaced with material with fuel-like properties. One can also think of adding extra weight to the assembly in other positions, giving about the same weight to the assembly. In all cases, a tomographic safeguard measurement must be made with enough accuracy to detect missing rods no matter what scenario has caused the possible removal.

One way to control if the fuel assemblies are intact is to use tomography to make sure that all the positions really contain fuel rods. Tomography is widely used in medicine, and it is also getting more frequently used in industrial applications. There are various tomography techniques and in this special case a technique called SPECT (Single Photon Emission Computed Tomography) is the one examined. This technique is based upon the emission of great amounts of gamma radiation from the extremely radioactive waste. Since the waste itself provides large attenuation of the gamma radiation, it is not possible to detect a missing inner rod by just examining the radiation intensities in different directions. By applying tomography though, it might be possible to determine if there are rods missing even if the empty positions are situated in the middle of the assembly. This is accomplished by using a large number of intensity measurements in various positions around a fuel assembly and reconstructing the activity distribution within the assembly using tomographic algorithms.

In this work, simulations of the radiation from a fuel assembly have been made. The simulated intensities have been used for reconstructions of the activity distribution within the simulated assembly. Various measurement strategies have been simulated, and three different tomographic algorithms have been used for the reconstructions. The simulations have been made using the same geometry as an 8x8 BWR fuel assembly placed in the experimental equipment located at CLAB[*] in Oskarshamn, Sweden, since the first goal was to check the possibilities of using that equipment for tomography. The equipment is described in section 2.2.

2. Background

2.1 Construction of an 8x8 BWR fuel assembly

The examinations in this work have been based upon nuclear fuel of the 8x8 BWR type. It consists of 8x8 fuel rod positions, where normally one of the positions contains a water channel, and the other 63

[*] CLAB = ‘Centralt Mellanlager för använt bränsle’.

contain fuel rods. The rods are made up by cylindrical fuel pellets contained in zircaloy tubes. In the position of the water channel, there is a zircaloy tube containing water. The cross section of an 8x8 BWR fuel assembly is shown in figure 2.1. Typical dimensions of an assembly are:

-Fuel radius:	5,22 mm
-Zircaloy tube radius:	6,125 mm
-Distance between rod centres:	16,00 mm
-Fuel length	3600 mm

A unit cell is defined as a square with 16 mm side centred around a fuel rod. The fuel is marked as grey zones in figure 2.1. The surrounding zircaloy tubes are also marked.

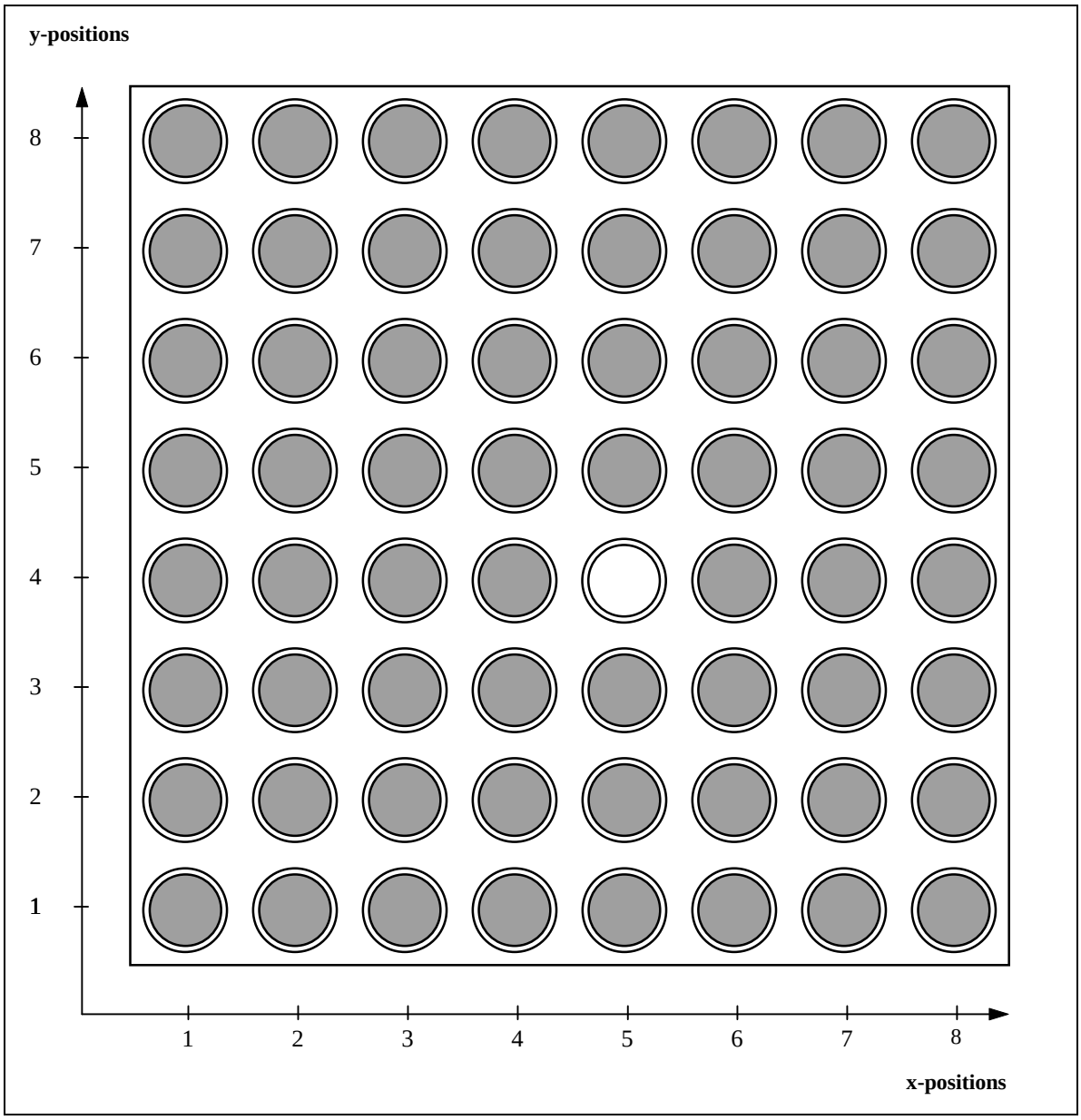

Figure 2.1. Cross section of an 8x8 BWR fuel assembly.

In figure 2.1, a system of coordinates for the positions of the fuel rods is introduced. The figure shows that the position of the water channel is set to (5,4) in the standard element.

2.2 Existing measurement equipment

The purpose of this work was to examine the possibilities of performing tomographic measurements on nuclear fuel using the existing measurement equipment at CLAB in Oskarshamn, Sweden. The equipment can be found in figures 2.2 and 2.3. All simulations and reconstructions in this work are based upon the geometric conditions given in these figures. The equipment is not optimised for tomographic measurements, since it was built for other purposes, i. e. gamma scanning, see ref. (8). Suggestions of how to improve the set-up for the issue of tomography can be found in section 8.

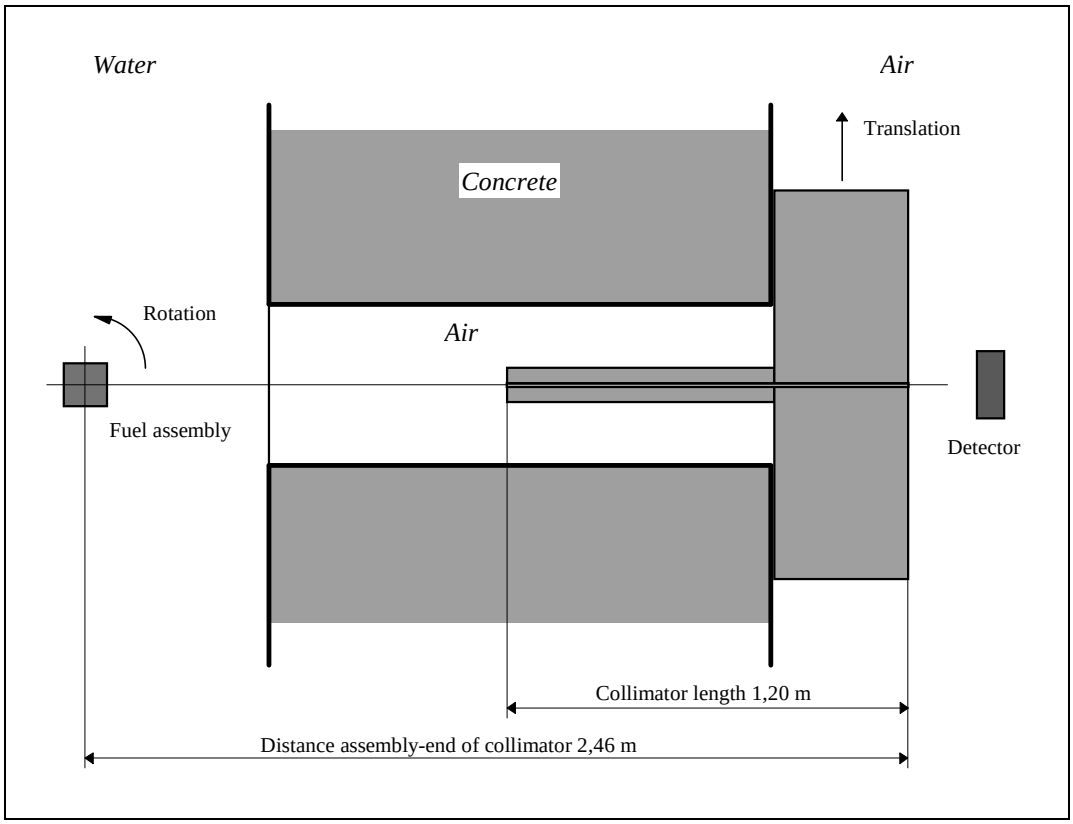

Figure 2.2. Experimental equipment. Schematic view from above.

As can be seen in figure 2.2, the distance between the fuel assembly and the opening of the collimator is 2,46 m. The assembly is placed in the rotation equipment to the left, giving possibilities of performing measurements in various projection angles. The detector and the collimator can be laterally translated to cover the whole projection of the assembly. Collimators with widths between 1 and 5 mm are available at the measurement site. Between the detector end and the assembly end of a collimator, the height increases from 8,2 to 23,4 cm, implying a total height of sight of the assembly of about 55 cm. In this work, however, only a thin section of the assembly has been considered. At about every 0,5 m of the height of the assembly, the rods are positioned by spacers. Measurements are planned to be performed between two spacers. The vertical positioning is made using an elevator equipment, shown in figure 2.3.

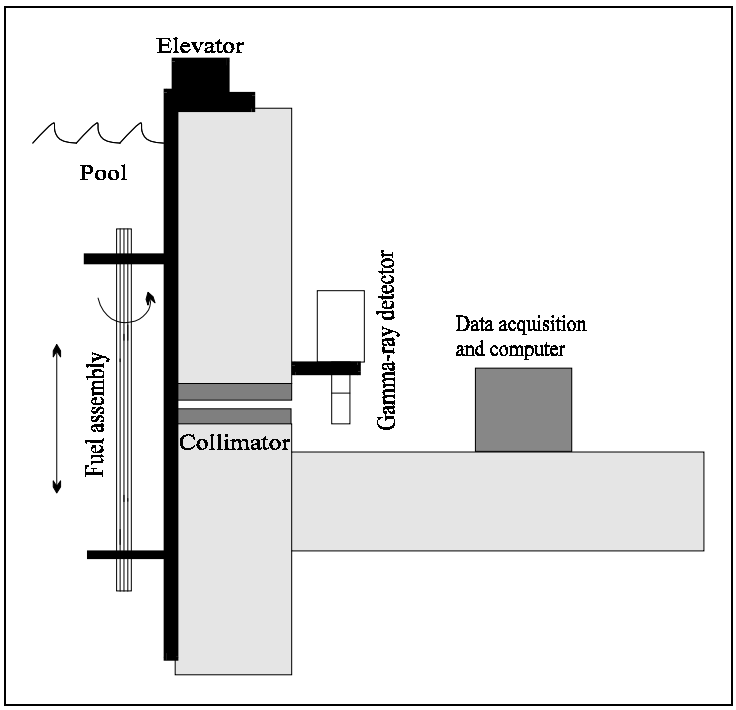

Figure 2.3. Schematic side view of the experimental equipment.

The positioning of an assembly does not allow the adjustment of the centre of rotation to coincide with the centre of the assembly. Anyway, in the simulations in this work, the two centres have been assumed to coincide, but an examination of how to correct for such a displacement has been made. (See appendix 3.)

The usage of a high resolution germanium detector is planned. The combination with a multi-channel analysing system will give the possibility of measuring gamma intensities within small energy intervals.

2.3 The gamma radiation

The fission products in nuclear power plants are neutron-rich nuclides, since uranium contains proportionally more neutrons than the fission products and only a few neutrons are emitted in the fission process. The most common decay mode of these products is beta-decay, where a neutron is converted into a proton through the process:

$$n \rightarrow p^+ + e^- + \overline{\nu}_e$$

After irradiating a fuel assembly, it contains various fission products of which most have a very short decay time. Measurements of the fuel assemblies before storage are planned to take place after cooling times of about 30 to 40 years. Most fission products will have decayed by then, and only a few still remain to an extent to be feasible for measurements. Tomography also requires radiation penetrating enough to escape from the inner parts of the object. For the case of tomography of a nuclear fuel assembly shown in figure 2.1, a high gamma energy is required since the attenuation is considerable. The most feasible fission products for tomographic measurements are:

Cs-137 with a half-life of 30 years
Eu-154 with a half-life of 8.5 years

Parts of the decay schemes of Cs-137 and Eu-154 can be found in figures 2.4 and 2.5. The complete decay schemes can be found in ref. (5).

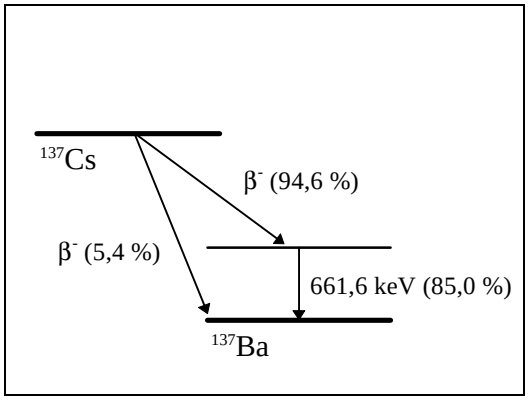

Figure 2.4. The decay of Cs-137.

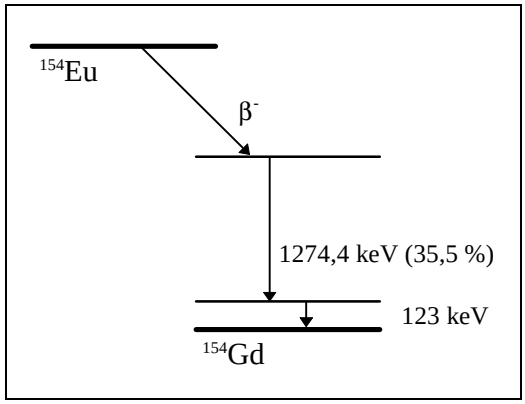

Figure 2.5. The decay of Eu-154.

There are several other decay modes for Eu-154, but the one shown in figure 2.5 is the most interesting one due to the relatively large penetrability of the gamma radiation with as high an energy as 1274,4 keV.

Nuclear decay is governed by the exponential law $N(t) = N(0)\, e^{-\lambda t}$, where N = the number of nuclei and λ = the decay constant. This makes the number of disintegrations per second distributed according to a Poisson distribution. If the expectation value of a Poisson distributed quantity is M, the standard deviation is equal to the square root of M, determining the statistical noise afflicting the measured gamma intensities.

2.4 Gamma-ray attenuation

The volume composition of a fuel assembly described in section 2.1 is typically: 33,4 % UO_2
12,6 % zircaloy
54,0 % water

For gamma radiation with energies 662 keV (Cs-137) and 1274 keV (Eu-154), the attenuation coefficients can be found in table 2.1, as can the average attenuation, μ_{ave}, of a fuel assembly described in section 2.1.

Table 2.1. Attenuation coefficients in various materials for gamma-rays from Cs-137 and Eu-154.

Attenuation coefficients [m^{-1}]		
Material	662 keV	1274 keV
UO_2	108,43	57,12
Zircaloy	56,91	43,25
Water	8,377	6,198
Average	47,91	27,87

The values of the attenuation coefficients in UO_2 and water are taken from ref. (5). The attenuation coefficients in zircaloy are approximated with the attenuation coefficients in steel, taken from ref. (6).

The gamma radiation from a certain rod is attenuated within the assembly approximately along the path between the rod centre and the edge of the assembly. Outside the assembly, all gamma radiation of the same energy is equally attenuated. Assuming equal activity for all rods gives the relative intensity from different rows, in a view orthogonal to the assembly side, as:

$$I_n = I_0 * e^{-\mu_{ave}*(a/2+n*a)}$$

where a = the side of a unit cell
n = number of rods to pass on the way to the detector
I_0 = intensity without attenuation
μ_{ave} = average attenuation coefficient of a unit cell

The contributions from the rods in different positions under those conditions can be found in table 2.2.

Table 2.2. Gamma-ray contributions from different rows in % of total for Cs-137 and Eu-154.

Contribution of total [%]		
Row	662 keV	1274 keV
1	53,7	37,0
2	24,9	23,7
3	11,6	15,2
4	5,4	9,7
5	2,5	6,2
6	1,2	4,0
7	0,5	2,5
8	0,2	1,6

If an outer rod is replaced by water or other material, it will be possible to detect a decrease in intensity by just measuring the intensity profiles along the sides of the assembly. From an inner rod though (4^{th} or 5^{th} row), the contribution to the total intensity is of the same order of magnitude as the expected activity variation between different rods. For that case, a decrease in intensity may be difficult to detect. It should be noted that if there is water instead of a rod in a position, the intensities from the rods behind the missing one will increase due to decreased attenuation, yielding even less possibilities of detecting the total intensity decrease. It is shown in table 2.2 that the contributions from the inner parts of an assembly is larger for gamma-rays with the higher energy from Eu-154 than from Cs-137.

For a tomographic measurement, every rod is measured many times, and all measurements are used for making reconstructed activities match with measured intensities, giving larger possibilities of detecting missing rods.

2.5 The effect of assuming attenuation of fuel in the position of a missing rod

As pointed out in the introduction, there can be several scenarios behind the removal of a fuel rod. Since possible empty positions must be presumed unknown, attenuation of fuel will be assumed in such positions. The algebraic algorithms described in section 3.1 rely on contribution coefficients strongly dependent on the assumed attenuation matrix. If a missing rod has been replaced by fresh fuel, lead or some other fuel-like material, the attenuation will be almost the same as before the removal, benefiting the tomographic reconstruction procedure. The presence of water in a fuel rod position will on the other hand cause the assumed attenuation matrix to be incorrect. This can be expected to influence the reconstructed activities in pixels at or near the position of the erroneous attenuation.

As a simple case to illustrate the discussion, one can consider the effects upon the reconstructed activities when the intensity from the fuel rods positioned behind a missing rod is increased due to attenuation in water instead of in a fuel-like material. To simplify the study, all rods are assumed to contain equal activity, A_0. Another simplification limits the consideration to views approximately orthogonal to the side of the assembly, causing the travel length through every unit cell to be 16 mm. Solid angle effects are omitted. In figure 2.6, the transmission of a gamma-ray through a fuel assembly where one rod is replaced with water is visualised. The following notations of the transmission through different parts of the assembly are used:

T_{ave}: average transmission through a unit cell
T_{miss}: transmission through the empty position (containing water)
T_{source}: transmission through the source rod
T_{rest}: transmission through the rest of the assembly and along the distance to the detector

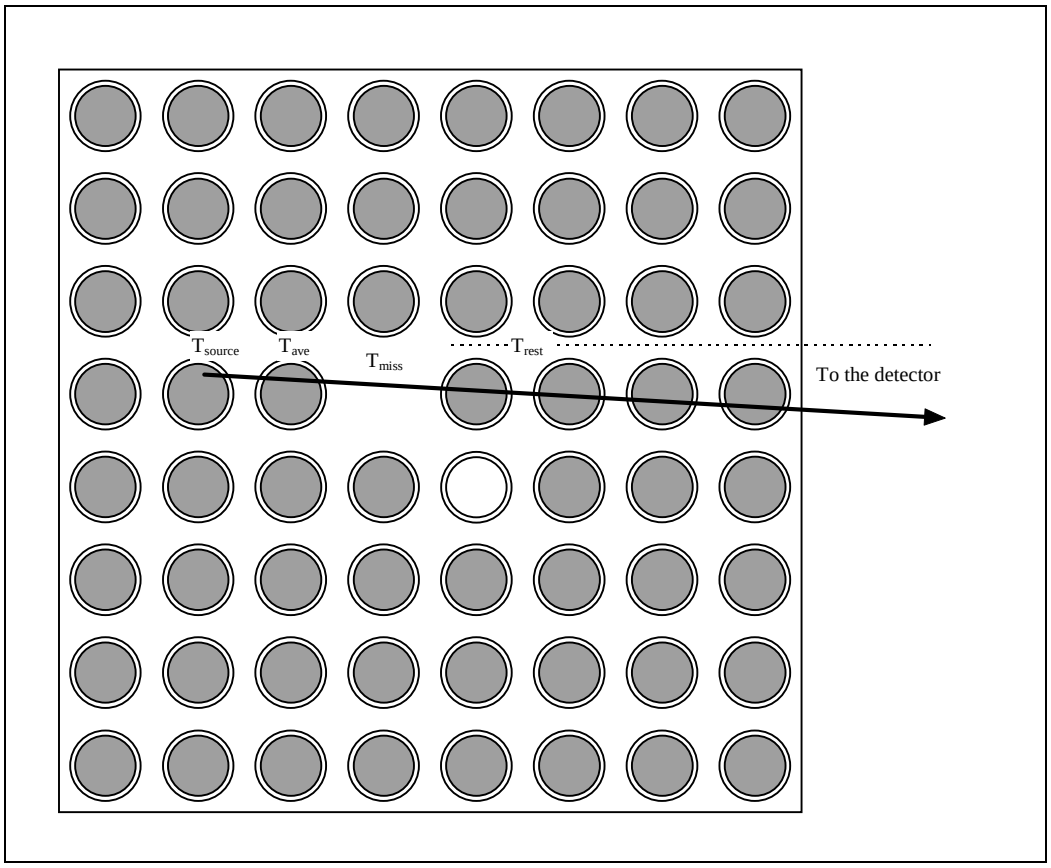

Figure 2.6. Transmission of a gamma-ray through a fuel assembly where one rod is replaced with water.

The measured intensity from the positions in front of the missing rod, I_{front}, will not be affected by the rods behind. The number of terms describing the total measured intensity depend on the number of rods behind the missing position. If the removal of an inner rod is considered, the case of having 3 or 4 rods behind the missing one is of current interest. The total measured intensity will be:

$$I_{measured} = I_{front} + A_0*T_{source}*T_{missing}*T_{rest} + A_0*T_{source}*T_{ave}*T_{miss}*T_{rest} + A_0*T_{source}*(T_{ave})^2*T_{miss}*T_{rest} + ...$$

The tomographic algorithms are constructed to find a solution where the measured and reconstructed intensities are matched. In the ideal case, the positions behind the missing rod will get correct reconstructed activity, A_0, since those positions are seen in many other projections too. The reconstructed activity distribution will then be consistent with the reconstructed intensity:

$$I_{reconstructed} = I_{front} + A_0*T_{source}*T_{ave}*T_{rest} + A_0*T_{source}*(T_{ave})^2*T_{rest} + A_0*T_{source}*(T_{ave})^3*T_{rest} + ... + A_{miss}*T_{source}*T_{rest}$$

where A_{miss} = reconstructed activity in the position of the missing rod.

Setting measured and reconstructed intensities equal yields the following equation:

$$I_{measured} = I_{reconstructed}$$

$$\Updownarrow$$

$$I_{front} + A_0*T_{source}*T_{miss}*T_{rest} + A_0*T_{source}*T_{ave}*T_{miss}*T_{rest} + A_0*T_{source}*(T_{ave})^2*T_{miss}*T_{rest} + ... =$$
$$A_0*T_{source}*T_{ave}*T_{rest} + A_0*T_{source}*(T_{ave})^2*T_{rest} + A_0*T_{source}*(T_{ave})^3*T_{rest} + ... + A_{miss}*T_{source}*T_{rest}$$

This gives the reconstructed value of A_{miss}:

$$A_{miss} = A_0*(T_{miss}(1 + T_{ave} + (T_{ave})^2 + ...) - T_{ave}(1 + T_{ave} + (T_{ave})^2 + ...)) \qquad (*)$$

The number of terms depend on the number of rods behind the missing one. The transmission values for gamma-rays passing a unit cell of 16 mm are shown in table 2.3. The values are obtained by using the same typical volume composition as in section 2.4 and the attenuation coefficients from table 2.1

Table 2.3. Transmission values for gamma-rays passing a fuel assembly unit cell.

	Transmission through a unit cell	
	662 keV	1274 keV
T_{ave}	0,465	0,640
T_{miss}	0,875	0,906

By applying equation (*) and the transmission values in table 2.3, the expected reconstructed activity in the position where a rod has been replaced with water can be calculated. The reconstructed activity, depending on the number of rods behind the missing one and the gamma-ray energy, can be found in table 2.4.

Table 2.4. Reconstructed activity in a position containing water under the assumption of attenuation of fuel.

Reconstructed activity [% of A_0]		
No of rods behind missing	662 keV	1274 keV
1	41	27
2	60	44
3	69	54
4	73	61

The probability of the largest values in table 2.4 is quite small, since the rods in the 8th row likely contribute to the total intensity in the same order as the statistical noise and since the reconstructed activities in the rods closest to the missing position ought to be affected. Views of a missing inner rod are also likely to have contributions from more than one rod behind the missing one, causing less probability of the smallest values. Therefore, for the Cs-137 gamma-ray energy, one can expect a reconstructed activity in the position of a missing central rod of between 50 and 70 % of the activity of the surrounding rods. The corresponding value for the Eu-154 energy is between 35 and 55 %.

The possibilities of detecting a missing rod obviously deteriorates if the rod is replaced with water instead of a fuel-like material., although the possibilities are increased if gamma-rays from Eu-154 are used. A missing inner rod should be more difficult to detect than an outer one due to the smaller contribution to the total intensity. The case with more than one rod missing is so far not examined.

2.6 Required precision of the reconstructions

Concluding the discussion in section 2.5, the reconstructions must be made with enough accuracy to discern a position with as little as 30 % less activity than the surrounding positions. The value of 30 % less activity is used while it is the theoretically largest value of the reconstructed activity in the position of a missing rod.

Since the reconstruction process cannot be expected to return the exact true activity values of the fuel rods, a certain standard deviation, S, added from the reconstruction, is introduced. The true activities also vary between the rods, e. g. according to a gradient variation, depending on the position in the core. In this work, the reconstructed activities are compared to the average activity of the rods. To give an estimate of the demands of the reconstructions, the true activity variation is taken to be

described by a statistic distribution with a standard deviation of 5 %. The total standard deviation, σ, will then be:

$$\sigma = \sqrt{5^2 + S^2}\ \%$$

This is true if the deviations can be considered not correlated. (See ref. (7).) In this work, it is taken as a reasonable level for the missing rod to be confidently discerned that the reconstructed activity in the position of a missing rod must be at least three standard deviations lower than the average. Therefore, if only 30 % less reconstructed activity is yielded in the position of a missing rod (see section 2.5), the introduced standard deviation, S, must be less than about 8 %.

Another imperfection introduced by the reconstruction process is the expected inability of reconstructing the activity in the position of a missing rod to zero, even if a correct attenuation matrix is assumed. The introduction of another parameter describing the quality of a reconstruction is therefore justified, namely the ratio, R, of the reconstructed activity in the position of a missing rod to the average of the other positions. Assuming R to be 6 % for the case of correctly assumed attenuation might lead to a value of R of 76 % for an unknown replacement of the rod with water, according to section 2.5. S must then also be limited to 6 % with the requirement of a reconstructed value three standard deviations smaller than the average,. As a first approach it seems convenient to use equal limits of the parameters S and R, whereby the requirements on the reconstructions are set to the maximum values:

S = 6 %
R = 6 %

The maximum value of R is defined for correctly assumed attenuation. The parameters S and R, chosen to be the figures of merit of the reconstructions, are further discussed in section 5.1. It can also be noted that S is the most critical parameter, since if S exceeds 8 %, an empty position might not be discerned no matter the value of R. The same limit for R is 15 %.

3. Theory

3.1 Tomographic algorithms

Tomography means reconstructing a picture of the inner regions of an object from measurements outside the object. In this case, emitted gamma quanta (see section 2.3) are detected and used for reconstructing a picture of the activity distribution within the object, so called “Single Photon Emission Computed Tomography” (SPECT). A large number of measurements are used, from one or several detectors in various positions around the object.

There are two main types of tomographic algorithms; analytic and algebraic. The analytic tomographic algorithms are based on the Radon transform introduced by Radon in 1917, but the applicability for tomography was not discovered until the 1960’s. The theory of the Radon transform can be found in almost any book dealing with tomography, for example in ref. (1) and (2). For the case of objects with large non-uniform attenuation, no analytic solution based upon the Radon transform has yet been found. (See ref. (1).) Consequently this approach is not applicable for the case of performing tomography upon nuclear fuel assemblies.

For this case algebraic methods must be used. By dividing the object into picture elements, pixels, it is possible to determine to what extent the emitted gamma quanta from each pixel reaches the detector, for every position of the detector. Contribution coefficients, w_{mn}, can then be introduced, meaning that out of the total activity A_n in pixel n, only $A_n * w_{mn}$ gamma quanta reaches the detector in position m. The calculation of the contribution coefficients in this work is further described in section 3.2. Knowing the contribution from every pixel to the measured intensity in the detector in each position, a system of M equations with N unknowns is yielded, where M is the number of measurements and N is the number of pixels. The equation system can be written as:

$$\begin{pmatrix} w_{11} & w_{12} & w_{13} \dots & w_{1N} \\ w_{21} & w_{22} & w_{23} \dots & w_{2N} \\ w_{31} & w_{32} & w_{33} \dots & w_{3N} \\ \vdots & & & \\ w_{M1} & w_{M2} & w_{M3} \dots & w_{MN} \end{pmatrix} \begin{pmatrix} A_1 \\ A_2 \\ A_3 \\ \vdots \\ A_N \end{pmatrix} = \begin{pmatrix} I_1 \\ I_2 \\ I_3 \\ \vdots \\ I_M \end{pmatrix}$$

where w_{mn} = contribution coefficient to measurement m from pixel n
A_n = activity in pixel n
I_m = intensity of measurement m

The equation system should preferably be overdetermined in order to minimise the effects of possible measurement noise, implying a number of measurements, M, larger than the number of pixels, N.

The algebraic reconstruction procedure starts by setting a start value to the activity in each pixel. The activity values are then corrected to match with measured intensities. The corrections can be made in numerous ways. An iteration is finished when the pixel activities have been corrected for all measurements. Many iterations may be done until a sufficient solution is obtained. The pixel activities are preferably presented as the mean values during the last iteration, yielding values best adapted to all measurements.

In this work, some known information have been used to simplify the calculations. One such simplification is based upon the fact that not all pixels contain uranium. Such pixels therefore contain negligible activity, the activity in them accordingly being set to zero.

Choosing start activities of the pixels near the correct activities increases the possibilities of a successful reconstruction. In this work, one single start value, A_0, was chosen for all pixels containing uranium. To be consistent with the measured intensities, A_0 was set to:

$$A_0 = \frac{\sum_m I_m}{\sum_{m,n} w_{mn}}$$

The activity corrections have been made for one measurement at a time. Three different methods of making the activity corrections have been examined:

1. The pixels contributing to the intensity in the detector in position m are equally corrected independently of their contribution. This method will from now on be referred to as the "EAC" method (standing for "Equal Activity Correction").
2. The pixels are activity corrected proportionally to their contribution to the measured intensity. This method will from now on be referred to as the "CAC" method (standing for "Contributional Activity Correction").
3. The pixels are activity corrected using another contributional method called "ART" (standing for "Algebraic Reconstruction Technique"). The difference between the CAC and the ART methods is a scaling factor of the adjustments.

For all methods, the intensity difference, ΔI_m, between calculated intensity, I^{cal}_m, and measured intensity, I^{meas}_m, is determined for every measurement m according to:

$$\Delta I_m = I^{cal}_m - I^{meas}_m$$

where $I^{cal}_m = \sum_n A_n * w_{mn}$ is calculated from the reconstructed activity values.

The new activity values A_n are determined in different ways depending on which of the methods above being applied:

EAC: $$A_n(new) = A_n(old) - \frac{1}{\sum_n w_{mn}} * \Delta I_m$$

CAC: $$A_n(new) = A_n(old) - \frac{w_{mn}}{(\sum_n w_{mn})^2} * \Delta I_m$$

ART: $$A_n(new) = A_n(old) - \frac{w_{mn}}{\sum_n (w_{mn})^2} * \Delta I_m$$

It can be noted for both the EAC and the ART method, that the new calculated intensity from the reconstructed activity values will be equal to the measured intensity after each correction:

EAC: $$I^{cal}_m(new) = \sum_n \left(w_{mn} * (A_n(old) - \frac{1}{\sum_n w_{mn}} * \Delta I_m) \right) = I^{cal}_m(old) - \Delta I_m = I^{meas}_m$$

ART: $$I^{cal}_m(new) = \sum_n \left(w_{mn} * (A_n(old) - \frac{w_{mn}}{\sum_n (w_{mn})^2} * \Delta I_m) \right) = I^{cal}_m(old) - \Delta I_m = I^{meas}_m$$

This procedure is however sensitive to statistical noise, causing large fluctuations of the reconstructed values. It is therefore relevant to introduce a relaxation parameter, R_p, with a value between 0 and 1, to stabilise the iteration procedure. The fact that no activity can be negative is also applied, yielding:

EAC: $$A_n(new) = Max(A_n(old) - R_p * \frac{1}{\sum_n w_{mn}} * \Delta I_m) , 0)$$

CAC: $$A_n(new) = Max(A_n(old) - R_p * \frac{w_{mn}}{(\sum_n w_{mn})^2} * \Delta I_m , 0)$$

ART: $$A_n(new) = Max(A_n(old) - R_p * \frac{w_{mn}}{\sum_n (w_{mn})^2} * \Delta I_m , 0)$$

where the notation Max(x,y) means choosing the maximum value of x and y.

The EAC method has been examined in ref. (3) and found to give good results for emission computed tomography (ECT) of barrels with radioactive contents, an application quite similar to the situation of tomography of nuclear fuel assemblies. The difference though, is the variation of the attenuation within the object, being larger for nuclear fuel than for the barrels examined in ref. (3).

The CAC method can be seen as a modified version of the EAC method, where a varying relaxation parameter, $\left(w_{mn} \Big/ \sum_n w_{mn} \right) < 1$, has been introduced.

The ART method is treated in ref. (1). The fitting procedure is described as steps in an N-dimensional space towards the M hyperplanes made up from the measurement equations. For the case of tomography with an overdetermined equation system afflicted with statistical noise, the solution is also shown to vary in the neighbourhood of the intersections of the hyperplanes. (That is around the area where the activity values best match with measured intensities.) The only difference from the CAC method is the change of the scaling factor of the adjustments from $(\sum_n w_{mn})^2$ to $\sum_n (w_{mn})^2$.

In this work, the time of the iteration procedure has been in the order of a few seconds. However, the calculation of the contribution coefficients has been a much more time-consuming process. If the tomographic measurements are made under fixed geometrical conditions, though, the coefficients can be stored. If the object consists of a large number of pixels, the coefficient matrix will be very large, and considerable computer memory will be needed for the storage.

3.2 The contribution coefficients, w_{mn}

The contribution coefficients, w_{mn}, describe to what extent the emitted gamma quanta from pixel n reaches the detector in position m. In this work, attenuation and geometrical conditions (e. g. how large solid angle the detector covers for the different pixels) have been considered. This makes the coefficients consist of two parts:

Geometric effect: $A_{det}/4\pi R^2$ where A_{det} = detector area
R = distance between pixel and detector

Attenuation: $e^{-\sum_i \mu_i * l_i}$ where μ_i = attenuation of material i
l_i = beam's travel length in material i

This would give the intensity contribution from pixel n to the detector in position m:

$$A_n * w_{mn} = A_n * \frac{A_{det}}{4\pi R^2} * e^{-\sum_i \mu_i * l_i}$$

The fact that a pixel might be seen by only a part of the detector (penumbra) has also been taken into account by dividing the detector into several parts, see figure 3.1. The total coefficient of each pixel consists of the sum of the calculated coefficients for each part of the detector.

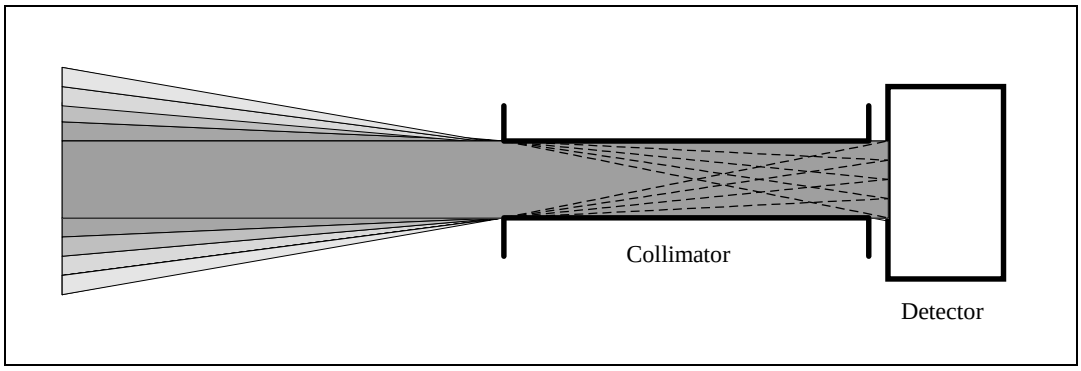

Figure 3.1. Penumbra effect, schematic view from above the equipment.

It was first determined for each pixel if emitted gamma quanta could pass the collimator and reach each detector part, by studying the geometry of the detector and collimator relative to the assembly. For those pixels, calculations of the attenuation and solid angle were carried out, otherwise the contribution coefficient was set to zero. The attenuation has been calculated in two different ways:

1. The distance between a pixel and the detector was divided into small steps, where each step added attenuation specific for the type of material.
2. The distance between a pixel and the detector was analytically studied, with respect to the distance a beam has to travel through different materials, whereby the total attenuation was calculated.

The two methods are thoroughly described in appendix 1, where they are shown to give similar results.

The calculations of the contribution coefficients can be performed more accurately by increasing the number of divisions of the detector. Other effects may be added, like for example intensity contributions from scattered gamma quanta. Since it is possible to choose a certain energy interval by using high-resolution gamma-ray spectroscopy, gamma quanta losing energy while being scattered will only have a small influence on the measured intensities. Contributions might also appear from elastically scattered gamma quanta in small angles. This, however, has not been considered in this report.

4. Simulations

The purpose of the simulations was to obtain gamma intensity patterns for testing the reconstruction procedure without performing time-consuming and expensive measurements. An additional purpose was to perform a theoretical determination of the detection level of a missing rod in the central part of an assembly. In the simulations, no effects of scattered gamma quanta have been considered. In this respect, the simulations are somewhat simplified.

4.1 Simulation procedure

When simulating the gamma-ray intensities around a nuclear fuel assembly, the assembly has been divided into pixels. Each pixel has been given a value of the activity, depending on the activity distribution to be simulated. The gamma-ray intensities are determined by using the contribution coefficients, w_{mn}, of section 3.2, describing to what extent emitted gamma quanta from pixel n reaches the detector in position m. If the activity in pixel n is set to A_n, the simulated intensity in the detector in position m will be:

$$I_n = \sum_n A_n * w_{mn}$$

The calculation of the contribution coefficients can be found in section 3.2. The attenuation was calculated in this context by dividing the distance between a pixel and the detector into small steps, referred to as method 1 in section 3.2. In order to achieve more accurate simulations, the assembly can be divided into a large number of pixels. In this work, the assembly has been divided into 400x400 pixels.

4.2 Simulation of statistical noise

When measuring the intensities experimentally, the measured data will be afflicted with statistical noise. According to section 2.3, the number of counts is Poisson distributed with a standard deviation equal to the square root of the number of counts.

In order to find out the measurement times needed to yield acceptable levels of statistical noise for the reconstructed activities, a method to add statistical noise to the simulated intensities was developed. If the number of counts is large, the Poisson distribution can be approximated with a normal distribution, meaning that the statistical noise is approximately normal distributed with a standard deviation equal to the square root of the number of counts. The normal distributed random numbers were obtained from random numbers between 0 and 1, using a method called the Box-Mueller method described in ref. (7). To achieve the effect of the same measurement time for all measurements, a maximum number of counts was chosen for the highest intensity measurement. This yields the statistically modified intensities:

$$I_{stat} = I_{simul} + N(0, \sqrt{maxcounts}) * \frac{I_{simul}}{maxcounts}$$

where I_{simul} denotes simulated intensities
I_{stat} denotes statistically modified intensities
$N(\mu,\sigma)$ denotes a normal distribution with expectation value μ and standard deviation σ

The experimental count rate is expected to be in the order of about 1000 counts/s for the equipment described in section 2.2. Therefore the maximum number of counts was chosen to 10 000, giving a measurement time in the order of 10 s and a standard deviation of 1 % for the measurement with the highest count rate (and larger standard deviation for the other measurements). For one simulation using a 5 mm collimator, the maximum number of counts was chosen to 40 000, giving a standard deviation of 0,5 % for the highest intensity measurement.

4.3 Simulated fuel assembly

The intensity patterns were simulated to correspond to 8x8 BWR fuel assemblies (see section 2.1). The activity was assumed to be evenly distributed within the individual rods, and all rods were assumed to contain equal amounts of activity. For the simulations, the activity concentration per unit height was tentatively set to 10^6 Bq/mm^2, which yields 85.6 * 10^6 Bq/rod. The even distribution within the rods is a simplification of reality, since it has been shown, for example in ref. (4), that especially Cs-137 tends to appear in higher concentrations at the surface than in the inner parts. The assumption of equal activity does not agree with reality either, since different parts of the core are exposed to different neutron flux during operation. This choice is more arbitrary though, since these are the values to reconstruct. The choice of simulating equal activities simplifies the analysis of the reconstructed activities.

Since a normal 8x8 BWR fuel assembly has a water channel in position (5,4) (see section 2.1), examinations can be made concerning whether the water channel can be revealed or not by simulating a normal fuel assembly. For future examinations the simulation program is prepared for the removal of more rods and the replacement with either water or fuel-like material.

4.4 Simulated intensity patterns

A number of different measurement situations were simulated, all using the same geometry as the experimental equipment at CLAB in Oskarshamn, Sweden, described in section 2.2. Some simulations (5 and 6 below) were made from angular and lateral positions determined from a study concerning how to get maximum contributions from the inner parts of the assembly. (See appendix 2.) In the other simulations the angular positions were evenly spaced between 0 and 360 degrees, and the lateral positions were evenly spaced between -90 and +90 mm. In all simulations, the simulated assembly had the appearance described in section 4.3. The following simulations were made:

1. ”Simul_Cs2”
   Gamma energy 662 keV (Cs-137) and a 2 mm collimator. The simulation consists of 120 projection angles and 120 collimator translations per angle.
2. ”Simul_Cs3”
   Gamma energy 662 keV (Cs-137) and a 3 mm collimator. The simulation consists of 120 projection angles and 60 collimator translations per angle.
3. “Simul_Cs5”
   Gamma energy 662 keV (Cs-137) and a 5 mm collimator. The simulation consists of 120 projection angles and 60 collimator translations per angle.
4. “Simul_Eu2”
   Gamma energy 1274 keV (Eu-154) and a 2 mm collimator. The simulation consists of 120 projection angles and 120 collimator translations per angle.
5. “Simul_Cs2_spec”
   Gamma energy 662 keV (Cs-137), a 2 mm collimator and specially chosen measurement positions, aiming to yield as much information from the inner parts of the fuel assembly as possible. 28 projection angles and 40 collimator translations per angle.
6. “Simul_Cs3_spec”
   Gamma energy 662 keV (Cs-137), a 3 mm collimator and specially chosen measurement positions, aiming to yield as much information from the inner parts of the fuel assembly as possible. 28 projection angles and 40 collimator translations per angle.

In appendix 4 some simulated projections can be found, showing views at 0^o and 45^o assembly rotation, using the simulated collimator widths 1, 2, 3 and 5 mm.

5. Reconstructions using simulated intensities

The goal of the reconstructions in this work has been to investigate if it is possible to detect a missing rod in a fuel assembly. The precise quantification of the activity is therefore not very important. With that in mind, some simplifications can be made. One such simplification is to use a small number of pixels in the reconstructed picture, yielding large areas where the activity concentration is set constant. The convergence of the determination of activity can then be improved at the expense of precision.

An assembly of the type shown in figure 1 in section 2.1, with a water channel in position (5,4), was simulated. Since possible replacements of fuel rods should be considered unknown (see section 1), the reconstructions were made both assuming correct attenuation (water in position (5,4)) and assuming a fuel rod in the water channel. The geometry of the simulated measurement equipment is described in section 2.2. The impact on the reconstructions have been studied from several parameters. These are:

-Type of reconstruction algorithm
-Number of pixels in the reconstructed picture
-Number of iterations
-Collimator width
-Relaxation parameter
-Number of measurements
-Distribution of angular positions of the assembly
-Distribution of lateral positions of the detector and the collimator

5.1 Figures of merit

The quantities chosen to be the figures of merit concerning the quality of the reconstructions were:

-The standard deviation of the activity of the positions containing fuel, S.
-The ratio of activity in the water channel to the average of the other positions, R.

Due to statistical reasons, S=0 will be impossible to achieve in practice. This means that the perfect picture would give R=0 and a small value of S. The goal of the reconstructions was thus to find strategies which minimise S and R. In section 2.6, maximum values of S and R were determined for an empty position to be revealed. The values of S and R should also stabilise after a number of iterations, since this forms a reasonable criterion that the reconstruction is complete.

5.2 Number of pixels in the reconstructed picture

The investigations on the influence of the number of pixels were made from simulated intensities using a 2 mm collimator. Statistics were added from the assumption of 10 000 counts in the highest intensity measurement, yielding 1% standard deviation for that measurement. Correct attenuation (with water in position (5,4)) was assumed in all reconstructions. All reconstructions were made using the EAC algorithm, described in section 3.1. In this work, the number of pixels has been varied between 64 (1 pixel per unit cell), 1024 (16 pixels per unit cell) and 4096 (64 pixels per unit cell). The pixel distribution for each case is shown in figure 5.1 for a unit cell. For the case of 16 pixels, some pixels have parts in more than one unit cell.

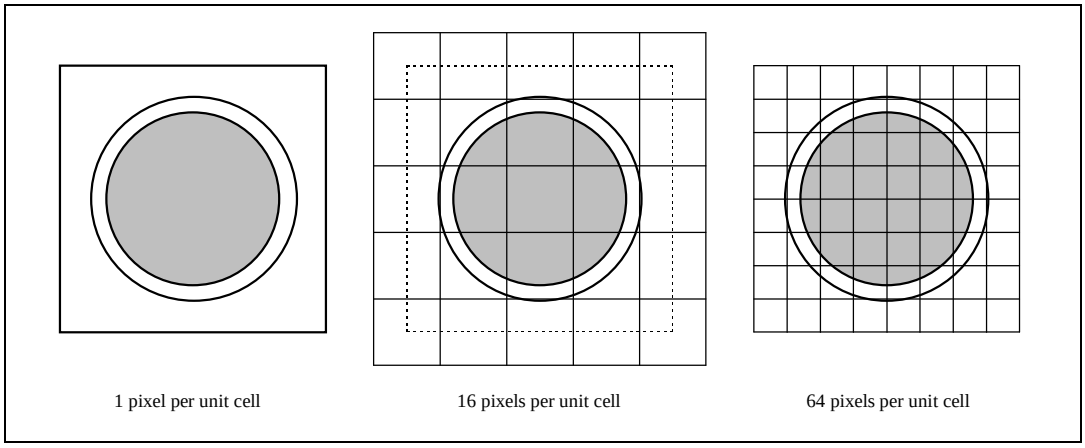

Figure 5.1. Pixel distribution.

The reconstructions were:

1x1 pixel: -EAC_Cs21_112: 60 projections and 120 translations per projection. 20 iterations with relaxation parameter R_p = 0,10.
-EAC_Cs21_113 60 projections and 60 translations per projection. 20 iterations with R_p = 0,10.

4x4 pixels: -EAC_Cs21_442: 60 projections and 120 translations per projection. 20 iterations with R_p = 0,10.
-EAC_Cs21_443 60 projections and 60 translations per projection. 20 iterations with R_p = 0,10.

8x8 pixels: -EAC_Cs21_882: 60 projections and 120 translations per projection. 20 iterations with R_p = 0,10.
-EAC_Cs21_883 60 projections and 60 translations per projection. 20 iterations with R_p = 0,10.

The figures of merit described in section 5.1, S and R, can be found in tables 5.1 and 5.2. They are also shown in figures 5.2 and 5.3 as functions of the number of iterations.

Table 5.1. S for reconstructions with various number of pixels.

S (%)						
No of iterations	EAC_Cs21_112	EAC_Cs21_113	EAC_Cs21_442	EAC_Cs21_443	EAC_Cs21_882	EAC_Cs21_883
2	5,1	3,2	1,9	2,3	1,6	2,2
4	9,7	2,8	2,6	2,2	1,5	1,8
6	20,4	2,7	3,9	2,5	1,7	1,7
8	39,0	2,8	5,5	2,8	2,1	1,7
10	47,9	2,8	7,3	3,1	2,5	1,7
15	48,2	2,8	11,6	4,0	3,7	1,9
20	48,2	2,8	14,7	5,7	4,8	2,0

Table 5.2. R for reconstructions with various number of pixels.

R (%)						
No of iterations	EAC_Cs21_112	EAC_Cs21_113	EAC_Cs21_442	EAC_Cs21_443	EAC_Cs21_882	EAC_Cs21_883
2	12,3	18,8	9,9	18,7	10,4	22,2
4	1,2	3,4	5,8	8,3	5,2	9,8
6	6,4	0,7	6,5	7,0	4,9	6,9
8	15,9	0,4	6,8	7,3	5,2	5,6
10	10,0	0,3	8,0	7,3	5,3	5,3
15	6,8	0,3	17,5	9,0	5,8	4,9
20	6,6	0,2	24,7	13,4	5,7	4,9

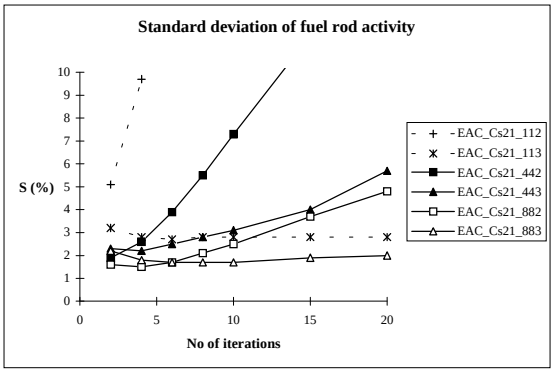

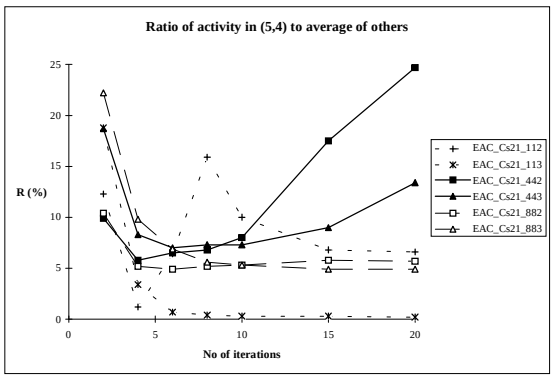

Figures 5.2 and 5.3. S and R for reconstructions with various number of pixels as functions of the number of iterations. Note the stability of reconstruction EAC_Cs21_113.

The reconstructions show instabilities for most cases. The exception is EAC_Cs21_113, giving small values of both S and R and then stabilising. The stabilisation even includes an almost constant reconstructed activity value of each pixel after each iteration. The instability of reconstruction EAC_Cs21_112, with a larger number of translations, might be due to consecutively made activity corrections for adjacent, densely placed, detector positions. This causes several consecutive corrections to the pixels values which, in turn, can cause large fluctuations. This might explain why EAC_Cs21_112 is unstable while EAC_Cs21_113 is not.

It can also be noted that the reconstructions with 8x8 pixels per unit cell show smaller values of both S and R than the reconstructions with 4x4 pixels. For these two types of reconstructions, the variation in reconstructed activities within a fuel rod is large, although the summed activities of the rods can show small variations. It is desirable to avoid such variations within the rods. It is also desirable to have few pixels in the reconstructions, due to the need of storing of a smaller number of contribution coefficients (see section 3.1). Since reconstruction EAC_Cs21_113 indicate possibilities of successful reconstructions using 1x1 pixel per unit cell, the further investigations were concentrated on that. The other options should still be considered, though, since it is reasonable to believe in better possibilities for them to deal with varying activity concentration within the rods. The CAC and ART algorithms might also improve the stability, as well as other measurement strategies.

5.3 Number of iterations and iteration strategy

The need of convergence of the reconstructions is obvious. As is shown in figures 5.2 and 5.3, the number of iterations might vary before a stable result is found. For reconstruction EAC_Cs21_113, the reconstructed picture stabilises after about 10 iterations. After stabilisation the number of iterations is of less importance. The number of iterations needed for stabilisation depends on the number of measurements, since more measurements implies more activity corrections per iteration. The number also varies with the relaxation parameter, since a small relaxation parameter implies small activity corrections. Examples of this can be found in section 5.5. In all stable reconstructions performed in this work, stability is obtained within 200 iterations, implying iteration times in the order of a few seconds.

The strategy during an iteration can also be varied. In order to renew the information content between consecutive projections, the projections may be varied in large steps, for example 70 degrees, until all projections have been used. In this way smoother corrections can be achieved, according to ref. (1). A too short translation step might cause an overcorrection of the reconstructed activities in some pixels, due to several corrections before surrounding pixels are considered. Therefore the corrections can be made in steps of, for example, every second translation. In this work though, no improvements have been seen due to such a strategy. Therefore the activity corrections have been made in consecutive order in all the reconstructions accounted for in this work, except for a few reconstructions using a 5 mm collimator, described in section 5.4.3. There is also a possibility of making corrections to many measurements at a time, for example an entire projection, but that has not been studied in this work.

5.4 Various collimator widths

When decreasing the collimator width, more well-defined information is obtained. Since the count rate is decreased, though, the measurement times have to be increased in order to keep the statistical noise constant. It is therefore desirable to use as large a collimator as possible, still giving information well-defined enough for the algorithms. The larger the collimator, the more ways to adjust the pixel activities to the measurements, since more pixels contribute to the measured intensities. The size of the collimator influences the maximum number of pixels and vice versa. It should be noted that a wide collimator placed near the object gives similar result as a narrow collimator at a larger distance.

In this study, only the pixel distribution with 1x1 pixel per unit cell has been used. The width of the collimators available at the measurement site at CLAB vary between 1 and 5 mm. The simulations were performed using 2, 3 and 5 mm wide collimators. The stability seems to vary with the number of measurements (see section 5.8). Therefore the number of measurements has been varied, as has also the relaxation parameter. The reconstructions have been made using the EAC algorithm.

5.4.1 Collimator width 2 mm

In section 5.2, reconstruction EAC_Cs21_113 gave the parameter values S = 2,8 % and R = 0,2 %, using a 2 mm collimator. Since S and R should be less than about 6 %, according to the theoretical discussion in section 2.6, the demand is fulfilled. Further reconstructions using a 2 mm collimator were made to examine the effects of varying the relaxation parameter, measurement positions and gamma energy. The results can be found in sections 5.5-5.7.

5.4.2 Collimator width 3 mm

The results in section 5.2 indicate a risk of large fluctuations during the reconstructions if the collimator translations are placed too densely. The choice of a wider collimator implies a larger area seen from the detector, therefore a larger distance between adjacent positions should be used. The first reconstructions using a 3 mm collimator were made using a smaller number of measurements. An off-set angle, $\Phi(0)$, was also introduced in order to avoid views head-on a row of rods. The off-set angle is further examined in section 5.6. One of the first reconstructions using a 3 mm collimator is called EAC_Cs31_03. It was performed using:

-40 projections and 30 translations
-$\Phi(0) = 3^o$
-relaxation parameter 0,05.

100 iterations were made. The values of the parameters S and R during the iterations are shown in table 5.3 and figure 5.4. The simulated intensities come from simulation “Simul_Cs3” with added statistics of 1 % standard deviation in the simulated highest intensity measurement.

Table 5.3. Values of S and R during the iterations for a reconstruction using a 3mm collimator.

EAC_Cs31_11_03		
No of iterations	S (%)	R (%)
8	3,1	30,8
20	2,5	12,2
40	2,1	5,6
60	2,0	4,2
80	1,9	3,8
100	1,9	3,6

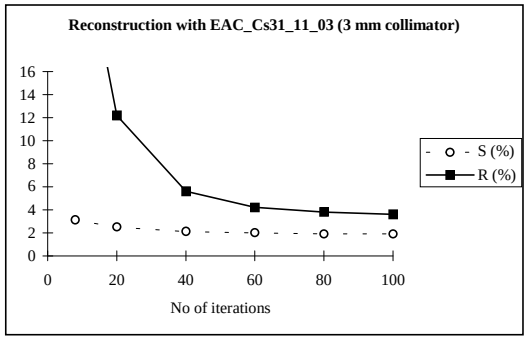

Figure 5.4. Values of S and R during the iterations, using a 3mm collimator.

As can be seen from the results, the reconstruction stabilises at values of S and R adequate for safeguard purposes according to section 2.6.

5.4.3 Collimator width 5 mm

For some reconstructions using a 5 mm collimator, the values of the parameters S and R during the iterations can be found in tables 5.4-5.5. The results are also shown in figures 5.5-5.6. All reconstructions have been made using the EAC algorithm (see section 3.1) and intensities from simulation "Simul_Cs5". The reconstructions are:

-EAC_Cs51_11_01: 60 projections and 30 translations. $\Phi(0) = 3^o$. $R_p = 0{,}05$.

-EAC_Cs51_11_02: 40 projections and 30 translations. $\Phi(0) = 3^o$. $R_p = 0{,}05$.

-EAC_Cs51_11_03: 60 projections and 20 translations. $\Phi(0) = 3^o$. $R_p = 0{,}05$.

-EAC_Cs51_11_04: 40 projections and 20 translations. $\Phi(0) = 3^o$. $R_p = 0{,}05$.

-EAC_Cs51_11_09: 120 projections and 60 translations. $\Phi(0) = 0^o$. $R_p = 0{,}03$.

-EAC_Cs51_11_10: 120 projections and 30 translations. $\Phi(0) = 0^o$. $R_p = 0{,}05$.

-EAC_Cs51_11_12: 60 projections and 15 translations. $\Phi(0) = 3^o$. $R_p = 0{,}05$.

-EAC_Cs51_11_13: 40 projections and 15 translations. $\Phi(0) = 3^o$. $R_p = 0{,}05$.

Table 5.4. S for some reconstructions using a 5 mm collimator.

S (%)								
No of iterations	EAC.._01	EAC.._02	EAC.._03	EAC.._04	EAC.._09	EAC.._10	EAC.._12	EAC.._13
2	3,9	3,3	3,2	2,4	4,5	4,6	4,4	3,7
6	5,3	4,8	4,6	4,1	6,2	6,0	5,5	4,9
10	5,8	5,3	5,3	4,8	7,5	6,9	6,0	5,5
20	6,7	5,7	6,5	6,1	11,9	11,1	6,8	6,3
30	8,0	6,2	7,9	7,3	17,7	17,8	7,5	7,3
40	10,3	6,8	9,4	8,8	25,7	26,9	8,2	8,3

Table 5.5. R for some reconstructions using a 5 mm collimator.

R (%)								
No of iterations	EAC.._01	EAC.._02	EAC.._03	EAC.._04	EAC.._09	EAC.._10	EAC.._12	EAC.._13
2	67,8	72,7	74,6	80,7	53,9	56,9	65,5	72,8
6	44,3	49,2	52,9	61,2	32,9	34,6	51,3	59,3
10	34,7	39,0	43,2	51,2	31,5	30,2	43,6	51,0
20	24,4	30,0	34,3	40,1	43,6	31,6	35,8	41,6
30	18,2	28,2	33,2	36,1	63,9	35,6	32,8	35,4
40	11,2	28,6	35,5	34,9	95,2	38,3	32,4	33,6

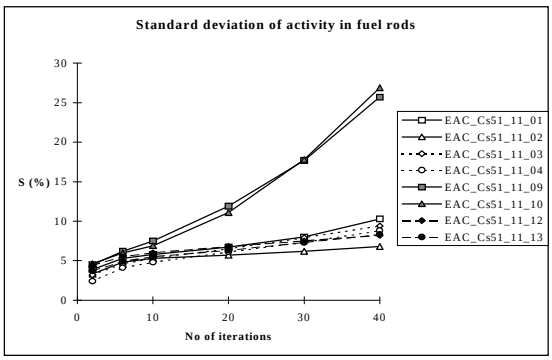

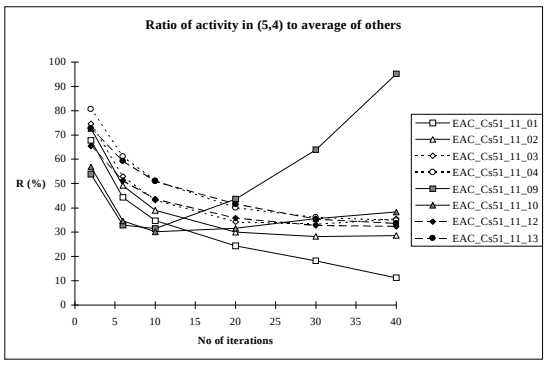

Figures 5.5 and 5.6. S and R as functions of the number of iterations for some reconstructions using a 5 mm collimator.

S steadily increases with the number of iterations. R seems to reach a minimum before increasing again, except for reconstruction EAC_Cs51_11_01, for which it decreases to an acceptable level according to section 2.6. S is still unacceptably high, though. A picture of EAC_Cs51_11_01 after 40 iterations can be seen in appendix 5, showing the inability of the reconstruction to fulfil reasonable requirements on quality.

Some more reconstructions have also been made using a 5 mm collimator in order to study the effects of varying relaxation parameter, iteration strategy and statistics. All of them were made using intensities from simulation "Simul_Cs5", with 40 projections, 30 translations and $\Phi(0) = 3^o$, since that strategy seemed to give the best results above. The following reconstructions were made:

-EAC_Cs51_11_05: $R_p = 0{,}10$.

-EAC_Cs51_11_06: $R_p = 0{,}01$.

-EAC_Cs51_11_07: $R_p = 0{,}05$.
Adjustment in steps of every 5th translation.

-EAC_Cs51_11_08: $R_p = 0{,}05$.
Adjustment in steps of every 5th projection.

-EAC_Cs505_11_01: $R_p = 0{,}05$.
0,5 % standard deviation (40 000 cts) at maximum intensity.

The results can be found in tables 5.6-5.7 and in figures 5.7-5.8. Reconstruction EAC_Cs51_11_02 is also included for comparison.

Table 5.6. S for some reconstructions using a 5 mm collimator.

S (%)						
No of iterations*	EAC_Cs51_11_02	EAC_Cs51_11_05	EAC_Cs51_11_06	EAC_Cs51_11_07	EAC_Cs51_11_08	EAC_Cs505_11_01
2	3,3	4,2	3,0	4,1	4,1	3,2
6	4,8	5,5	4,6	4,9	4,9	4,6
10	5,3	5,9	5,1	5,5	5,5	4,9
20	5,7	7,0	5,6	6,0	5,9	5,4
30	6,2	8,7	5,9	6,7	6,4	6,2
40	6,8	11,1	6,4	8,3	7,5	7,3

*For reconstruction EAC_Cs51_11_06 the iteration number should be multiplied by 4. This is made because of slower convergence due to a smaller relaxation parameter.

Table 5.7. R for some reconstructions using a 5 mm collimator.

R (%)						
No of iterations	EAC_Cs51_11_02	EAC_Cs51_11_05	EAC_Cs51_11_06	EAC_Cs51_11_07	EAC_Cs51_11_08	EAC_Cs505_11_01
2	72,7	60,7	75,9	63,0	63,2	73,1
6	49,2	36,3	53,8	48,1	47,8	50,6
10	39,0	29,4	43,2	35,5	34,4	40,8
20	30,0	27,2	32,5	29,9	27,8	31,5
30	28,2	29,6	29,5	29,2	26,5	29,7
40	28,6	32,5	29,2	32,1	28,2	30,4

*For reconstruction EAC_Cs51_11_06 the iteration number should be multiplied by 4. This is made because of slower convergence due to a smaller relaxation parameter.

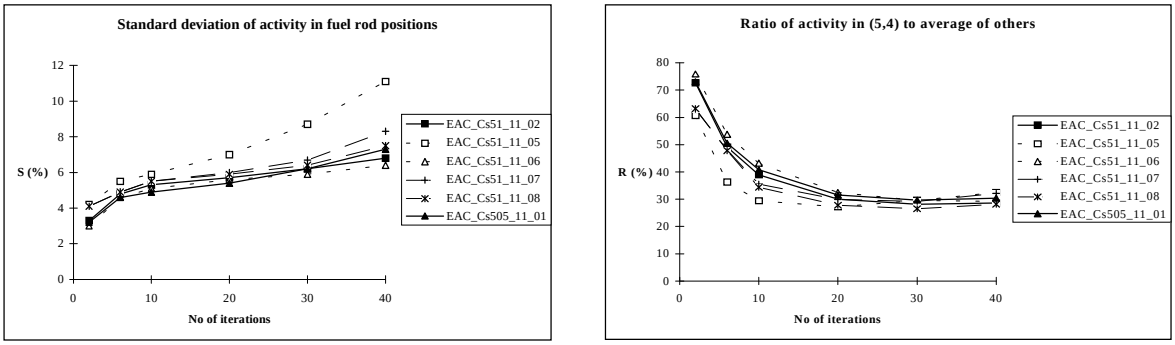

Figure 5.7 and 5.8. S and R as functions of the number of iterations for some reconstructions using a 5 mm collimator. Note the steadily increasing values of S and the relatively high values of R.

Neither changes in the relaxation parameter, nor in iteration strategy or statistics seem to improve the reconstructions. It is therefore likely that the 5 mm collimator is too wide for the algorithms.

5.4.4 Remarks and conclusions

Comparing the reconstructions from simulations using a 5 mm collimator in section 5.4.3 to the reconstructions using 2 and 3 mm collimators in section 5.4.1 and 5.4.2, the results are found to be more coherent with the requirements formulated in section 2.6 for the two latter cases. The reason why the 5 mm collimator is not applicable can probably be found in the lack of specification of the information. Too many pixels contribute in every measurement, yielding too many ways of adjusting to the measured intensities. It can be noted for the geometry used, that a collimator width of 5 mm implies a field of view of about 15 mm, or about as large as a unit cell, at the assembly.

The reconstructions made from simulated intensities using a 3 mm collimator were found to give almost as small values of S and R as the reconstructions made from simulations using a 2 mm collimator. Since it is desirable to use a wide collimator, due to the possibilities of getting more counts and therefore smaller statistic variations in shorter time, most of the following reconstructions from simulated intensities have been made using a 3 mm collimator.

5.5 Relaxation parameter

When adjusting the reconstructed activity distribution of the object to match with the measured intensities, the adjustments can be made smoother by the use of a relaxation parameter, R_p (see section 3.1). The optimal value of R_p likely varies between the three methods used for the activity corrections.

5.5.1 The EAC method

For the studies of the relaxation parameter using the EAC method, reconstructions were made from simulated intensities using a 2 mm collimator, 40 projections, 40 translations and $\Phi(0) = 3^o$ from

simulation “Simul_Cs2”. Statistic variations with 1 % standard deviation in the simulated highest intensity measurement were added. The reconstructions were:

-EAC_Cs21_11_07: $R_p = 0,10$.
-EAC_Cs21_11_08: $R_p = 0,05$.
-EAC_Cs21_11_11: $R_p = 0,01$.

The values of the parameters S and R can be found in tables 5.8-5.9. The convergence of each reconstruction has been visualised in figures 5.9-5.10.

Tables 5.8 and 5.9. S and R for three different values of the relaxation parameter, using the EAC method.

S (%)			
No of iterations	$R_p = 0,10$	$R_p = 0,05$	$R_p = 0,01$
4	2,2	2,6	1,7
8	1,7	2,1	2,5
12	1,6	1,7	2,9
20	1,7	1,5	3,2
30	1,7	1,5	3,2

R (%)			
No of iterations	$R_p = 0,10$	$R_p = 0,05$	$R_p = 0,01$
4	14,2	33,9	78,6
8	1,4	14,5	63,5
12	0,0	6,2	52,5
20	0,0	0,1	37,8
30	0,0	0,0	25,5

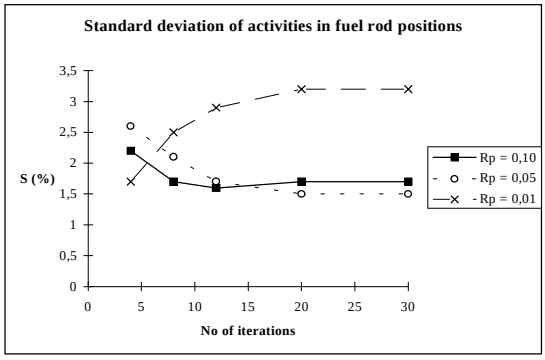

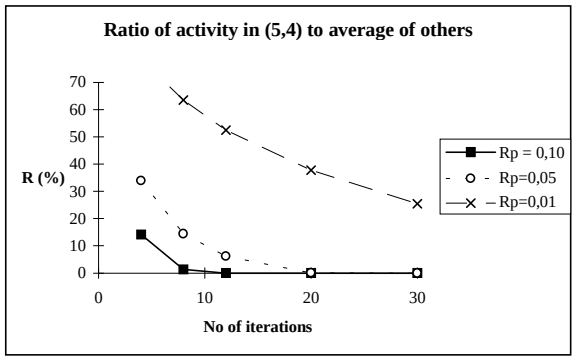

Figures 5.9 and 5.10. S and R as functions of the number of iterations for three different values of the relaxation parameter, using the EAC method. Note the slower convergence for smaller values of R_p.

As expected, the convergence is slower for reconstructions using smaller relaxation parameters. A somewhat surprising result is S getting larger for the smallest value of R_p. This might be due to large activity corrections of the positions next to the water channel, since the relatively slow activity correction from the initial activity, being equal for all pixels, of the position of the water channel might affect nearby positions. After 80 iterations, S has started decreasing again, indicating an increase of the activities in nearby positions as the activity in the empty position decreases.

When taking the mean values of S and R during the last iteration of each reconstruction, the values are as follows:

-$R_p = 0,10$ (30 iterations): S = 1,7 %
R = 0,6 %

-$R_p = 0,05$ (30 iterations): S = 1,5 %
R = 0,3 %

-$R_p = 0,01$ (80 iterations): S = 2,7 %
R = 10,2 %

From the results presented, $R_p = 0,05$ was chosen for the continuing reconstructions using the EAC method. This value offered both fast convergence and reasonably small values of S and R.

5.5.2 The CAC method

The tests with various values of the relaxation parameter for the CAC method were carried out using simulated intensities from simulation "Simul_Cs3_spec", i. e. using a 3 mm collimator and specially chosen measurement positions. (See appendix 2.) Statistic variations were added with 1 % standard deviation in the simulated highest intensity measurement. All 28 projections and 40 translations were used for the reconstructions. The reconstructions were:

-CAC_Cs31_102: $R_p = 1{,}00$
-CAC_Cs31_103: $R_p = 0{,}40$
-CAC_Cs31_104: $R_p = 0{,}10$

The values of S and R of the reconstructions can be found in tables 5.10-5.11. The results have been visualised in figures 5.11-5.12.

Tables 5.10 and 5.11. S and R for three different values of the relaxation parameter, using the CAC method.

S (%)			
No of iterations	$R_p = 1{,}00$	$R_p = 0{,}40$	$R_p = 0{,}10$
3	3,8	3,5	1,8
9	2,6	3,3	3,1
18	2,2	2,4	3,6
30	2,2	1,8	3,4
60	2,2	1,4	2,6
90	2,2	1,4	2,0
120	2,2	1,4	1,7

R (%)			
No of iterations	$R_p = 1{,}00$	$R_p = 0{,}40$	$R_p = 0{,}10$
3	26,7	48,4	80,6
9	9,1	21,9	56,5
18	3,1	11,1	37,8
30	1,1	5,7	25,8
60	0,5	1,8	13,7
90	0,5	1,0	8,6
120	0,5	0,8	5,7

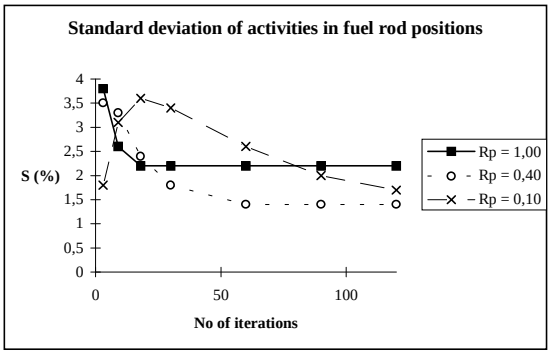

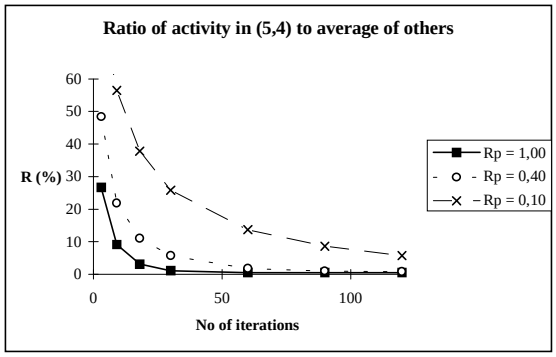

Figures 5.11 and 5.12. S and R as functions of the number of iterations for three different values of the relaxation parameter, using the CAC method.

As expected, the convergence is again slower for reconstructions using smaller relaxation parameters. The reconstruction using $R_p = 0{,}10$ has not yet stabilised, but does not seem to give significantly smaller standard deviation than $R_p = 0{,}40$. Due to the slow convergence, $R_p = 0{,}10$ does not seem like a suitable choice. When taking the mean values during the 120th iteration of each reconstruction, the values are as follows:

-$R_p = 1{,}00$: S = 1,4 %
R = 0,6 %

-$R_p = 0{,}40$: S = 1,1 %
R = 0,8 %

-$R_p = 0{,}10$: S = 1,6 %
R = 5,7 %

The reconstruction using R_p = 0,40 gives the smallest value of S, but a slightly larger value of R than the reconstruction using R_p = 1,00. Since both reconstructions give acceptable values of both S and R, but S is the parameter of most importance according to section 2.6, the choice of R_p would be 0,40. However, in order to obtain slightly faster convergence, R_p = 0,50 was chosen for the rest of the reconstructions using the CAC method.

5.5.3 The ART method

The tests with various values of the relaxation parameter for the ART method were made using the same simulated intensities as in section 5.5.2. Besides tests with different constant values of R_p, possibilities of varying R_p with the number of iterations have also been examined. Two ways of varying R_p have been tested; $R_p = (\text{iteration number})^{-1}$ and $R_p = (\text{ceil}(0{,}1*\text{iteration number}))^{-1}$, where ceil(x) denotes x rounded to the nearest higher integer. Both methods imply smaller values of R_p the more iterations that have been made. The reconstructions were:

-ART_Cs31_102a: R_p = 1,00
-ART_Cs31_102b: $R_p = (\text{iteration number})^{-1}$
-ART_Cs31_102c: $R_p = (\text{ceil}(0{,}1*\text{iteration number}))^{-1}$
-ART_Cs31_103: R_p = 0,40
-ART_Cs31_104: R_p = 0,10

The results can be found in tables 5.12-5.13 and in figures 5.13-5.14.

Table 5.12. S for various values of the relaxation parameter, using the ART method.

S (%)					
No of iterations	R_p = 1,00	$R_p = (\text{iteration number})^{-1}$	$R_p = (\text{ceil}(0{,}1*\text{iteration number}))^{-1}$	R_p = 0,40	R_p = 0,10
3	4,4	3,4	4,4	3,6	3,9
9	3,8	2,2	3,8	2,1	3,6
18	3,8	1,8	2,1	1,8	2,6
30	3,8	1,6	1,7	1,8	1,9
60	3,8	1,4	1,3	1,9	1,2
90	3,8	1,3	1,2	1,9	1,1
120	3,8	1,3	1,1	1,9	1,1

Table 5.13. R for various values of the relaxation parameter, using the ART method.

R (%)					
No of iterations	R_p = 1,00	$R_p = (\text{iteration number})^{-1}$	$R_p = (\text{ceil}(0{,}1*\text{iteration number}))^{-1}$	R_p = 0,40	R_p = 0,10
3	10,0	16,3	10,0	19,9	47,4
9	0,4	9,9	0,4	6,1	24,1
18	0,4	7,2	0,6	1,7	13,7
30	0,4	5,7	0,5	0,6	7,5
60	0,4	4,2	0,3	0,5	2,3
90	0,4	3,6	0,2	0,5	0,9
120	0,4	3,2	0,2	0,5	0,5

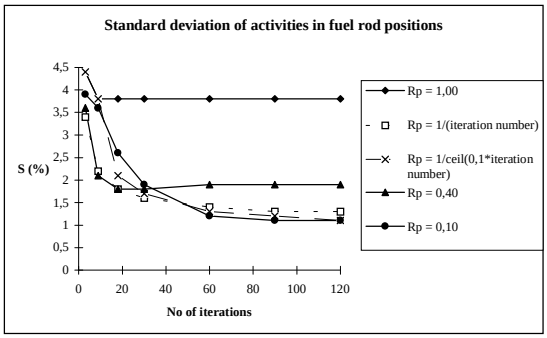

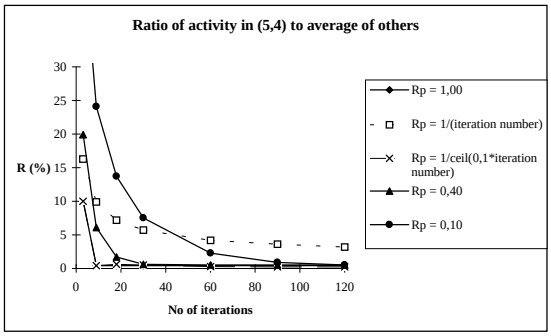

Figures 5.13 and 5.14. S and R as functions of the number of iterations for various values of the relaxation parameter, using the ART method.

The convergence is again slower for smaller relaxation parameters. For the reconstruction using R_p varying according to (iteration number)$^{-1}$, R is the largest, probably due to too few iterations with large values of R_p. When taking the mean activity values during the 120th iteration for each reconstruction, the values of S and R are as follows:

- R_p = 1,00: S = 2,3 %, R = 1,4 %
- R_p = (iteration number)$^{-1}$: S = 1,3 %, R = 3,2 %
- R_p = (ceil(0,1*iteration number))$^{-1}$: S = 1,1 %, R = 0,2 %
- R_p = 0,40: S = 1,4 %, R = 0,8 %
- R_p = 0,10: S = 1,1 %, R = 0,5 %

Using the mean activity values during the last iteration implies a remarkable decrease of S for the reconstruction with R_p = 1,00, although the value is still the largest. The reconstructions with R_p = 0,10 and R_p = (ceil(0,1*iteration number))$^{-1}$ seem to give the smallest values of both S and R, both fulfilling the demands of section 2.6. Since the latter has the advantage of faster convergence, that way of varying R_p seems to be of specific interest.

5.6 Choice of measurement positions

The first test concerning the effect of altering the measurement positions was carried out by just choosing different sets of measurements from the extensive simulation "Simul_Cs2", using a 2 mm collimator. The reconstructions were made from 40 projections and 40 translations, with evenly spaced projection angles between 0^o and 360^o. Varying sets of measurements were chosen by altering the angle of the first projection, $\Phi(0)$. The reconstructions were:

-EAC_Cs21_11_05: R_p = 0,10, $\Phi(0) = 0^o$
-EAC_Cs21_11_07: R_p = 0,10, $\Phi(0) = 3{,}0^o$

-EAC_Cs21_11_06: R_p = 0,05, $\Phi(0) = 0^o$
-EAC_Cs21_11_08: R_p = 0,05, $\Phi(0) = 3{,}0^o$

The results of the reconstructions can be found in table 5.14 and in figures 5.15-5.16.

Table 5.14. S and R for two different values of the first measurement angle, Φ(0).

	S (%)		R (%)	
	EAC_Cs21_11_05/07	EAC_Cs21_11_06/08	EAC_Cs21_11_05/07	EAC_Cs21_11_06/08
$\Phi(0) = 0^o$	6,3	6,1	2,5	1,1
$\Phi(0) = 3{,}0^o$	1,7	1,5	0,6	0,3

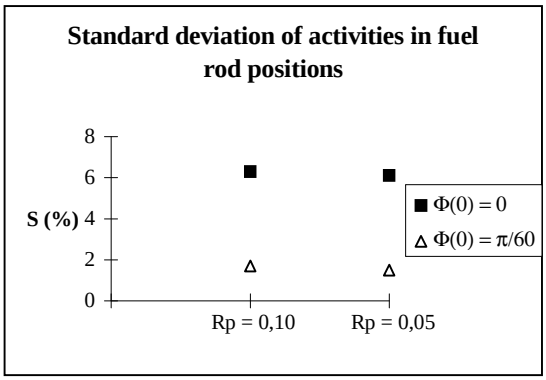

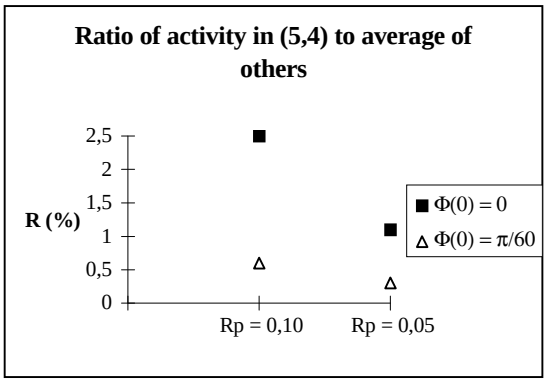

Figures 5.15 and 5.16. S and R for two different values of the first measurement angle, Φ(0). Note the smaller values of both S and R for the case of Φ(0) = 3,0°.

The results indicate the importance of the choice of measurement positions. Measurement data with much information from the inner parts of an assembly can be expected to be extra useful for the reconstructions. This is confirmed by the results above, with smaller values of both S and R if the views head-on a row of fuel rods are avoided. A special study have been carried out in order to determine measurement positions giving the most information from the inner parts of an assembly. (See appendix 2.) The study ended up at a set of measurement positions used for the simulations "Simul_Cs2_spec" and "Simul_Cs3_spec". The proceeding of this section consists of comparisons between reconstructions from simulations "Simul_Cs2" and "Simul_Cs3" on one hand, called "random contributions", and reconstructions from simulations "Simul_Cs2_spec" and "Simul_Cs3_spec" on the other, called "large contributions". The reconstructions used for this study were:

Using the EAC algorithm and a 2 mm collimator:

-EAC_Cs21_11_13: 30 projections and 40 translations from "Simul_Cs2". $\Phi(0) = 6{,}0^o$. 120 iterations with $R_p = 0{,}05$.

-EAC_Cs21_11_20: 28 projections and 40 translations from "Simul_Cs2_spec". 120 iterations with $R_p = 0{,}05$.

-EAC_Cs21_11_15: 24 projections and 40 translations from "Simul_Cs2". $\Phi(0) = 6{,}0^o$. 120 iterations with $R_p = 0{,}05$.

-EAC_Cs21_11_21: 24 projections and 40 translations from "Simul_Cs2_spec". 120 iterations with $R_p = 0{,}05$.

-EAC_Cs21_11_26: 24 projections and 20 translations from "Simul_Cs2". $\Phi(0) = 6{,}0^o$. 240 iterations with $R_p = 0{,}05$.

-EAC_Cs21_11_23: 24 projections and 20 translations from "Simul_Cs2_spec". 240 iterations with $R_p = 0{,}05$.

Using the EAC algorithm and a 3 mm collimator:

-EAC_Cs31_11_23: 30 projections and 40 translations from "Simul_Cs3". $\Phi(0) = 6{,}0^o$. 120 iterations with $R_p = 0{,}05$.

-EAC_Cs31_11_18: 28 projections and 40 translations from "Simul_Cs3_spec". 120 iterations with $R_p = 0{,}05$.

-EAC_Cs31_11_24: 24 projections and 40 translations from “Simul_Cs3”. $\Phi(0) = 6{,}0^{o}$. 120 iterations with $R_p = 0{,}05$.

-EAC_Cs31_11_19: 24 projections and 40 translations from “Simul_Cs3_spec”. 120 iterations with $R_p = 0{,}05$.

-EAC_Cs31_11_06: 30 projections and 20 translations from “Simul_Cs3”. $\Phi(0) = 6{,}0^{o}$. 150 iterations with $R_p = 0{,}05$.

-EAC_Cs31_11_20: 28 projections and 20 translations from “Simul_Cs3_spec”. 120 iterations with $R_p = 0{,}05$.

-EAC_Cs31_11_07: 24 projections and 20 translations from “Simul_Cs3”. $\Phi(0) = 6{,}0^{o}$. 200 iterations with $R_p = 0{,}05$.

-EAC_Cs31_11_21: 24 projections and 20 translations from “Simul_Cs3_spec”. 240 iterations with $R_p = 0{,}05$.

In order to make comparison possible, the reconstructions are placed in pairs with almost equivalent conditions except for the choice of measurement positions. The results from the reconstructions can be found in tables 5.15-5.16 and in figures 5.17-5.18.

Table 5.15. S for reconstructions from measurements with random contributions and with planned, large contributions from the inner parts of an assembly.

	S (%)						
	Cs21_13/15	Cs21_15/21	Cs21_26/23	Cs31_23/18	Cs31_24/19	Cs31_06/20	Cs31_07/21
Random contributions	4,1	1,4	2,9	2,1	2,3	2,5	4,7
Large contributions	2,1	2,1	3,0	2,1	2,4	2,6	2,5

Table 5.16. R for reconstructions from measurements with random contributions and with planned, large contributions from the inner parts of an assembly.

	R (%)						
	Cs21_13/20	Cs21_15/21	Cs21_26/23	Cs31_23/18	Cs31_24/19	Cs31_06/20	Cs31_07/21
Random contributions	9,4	0,2	1,0	0,4	1,0	0,2	0,1
Large contributions	1,5	2,0	0,2	1,2	0,8	0,1	0,1

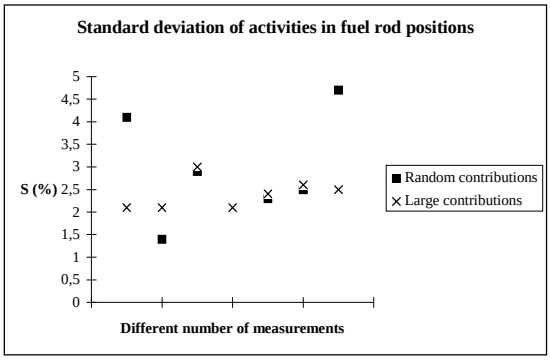

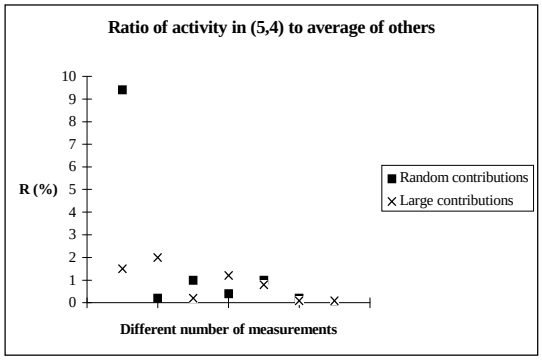

Figures 5.17 and 5.18. S and R for reconstructions from measurements with random contributions and with planned, large contributions from the inner parts of an assembly. Note the more stable behaviour for the case of large contributions.

The reconstructions from measurements in planned positions seem more reliable than the reconstructions with random contributions from the inner parts. It should be noted that in all reconstructions with random contributions, the sets used have not included the head-on views showing

the worst results in figures 5.15-5.16. Concluding this study, the choice of special measurement positions improves the reliability of the reconstructed activity distribution.

5.7 Effects of assuming attenuation of fuel in the water channel

In section 1, different scenarios behind the missing of fuel rods are discussed. So is the necessity of being able to detect missing rods even if attenuation of fuel is assumed where a rod has been replaced with water. The theoretical effect of this assumption can be found in section 2.5. In order to examine the possibilities of detection in a more realistic way, reconstructions have been made under the assumption of fuel in the existing water channel in a standard fuel assembly (see section 2.1).

5.7.1 Gamma energy 662 keV

The reconstructions in this investigation were made from simulated intensities using a 3 mm collimator and gamma energy 662 keV, corresponding to the decay of Cs-137. For comparison, the reconstructions were made in pairs of one reconstruction assuming correct attenuation and one reconstruction assuming attenuation of fuel in the water channel. The following reconstructions were made:

-CAC_Cs31_108: 24 projections and 20 translations from “Simul_Cs3_spec”. The CAC algorithm with R_p = 0,50. Correct attenuation assumed.

-CAC_Cs31_109: Same as CAC_Cs31_108, but assuming attenuation of fuel in (5,4).

-CAC_Cs31_103: 28 projections and 40 translations from “Simul_Cs3_spec”. The CAC algorithm with R_p = 0,40. Correct attenuation assumed.

-CAC_Cs31_110: Same as CAC_Cs31_103, but with R_p = 0,50 and assuming attenuation of fuel in (5,4).

-CAC_Cs31_107: 30 projections and 20 translations from “Simul_Cs3”. The CAC algorithm with R_p = 0,50. Correct attenuation assumed.

-CAC_Cs31_111: Same as CAC_Cs31_107, but assuming attenuation of fuel in (5,4).

-ART_Cs31_108: 24 projections and 20 translations from “Simul_Cs3_spec”. The ART algorithm with R_p varying according to $(\text{ceil}(0{,}1*\text{iteration number}))^{-1}$. Correct attenuation assumed.

-ART_Cs31_109: Same as ART_Cs31_108, but assuming attenuation of fuel in (5,4).

The results can be found in tables 5.17-5.18 and in figures 5.19-5.20.

Table 5.17. S under the assumption of correct attenuation and attenuation of fuel in the water channel.

	S (%)			
	CAC_Cs31_108/109	CAC_Cs31_103/110	CAC_Cs31_107/111	ART_Cs31_108/109
Correct attenuation	1,2	1,1	1,3	1,3
Attenuation of fuel in (5,4)	1,4	1,2	1,7	1,7

Table 5.18. R under the assumption of correct attenuation and attenuation of fuel in the water channel.

	R (%)			
	CAC_Cs31_108/109	CAC_Cs31_103/110	CAC_Cs31_107/111	ART_Cs31_108/109
Correct attenuation	0,0	0,8	0,1	0,0
Attenuation of fuel in (5,4)	58,9	62,8	54,1	59,2

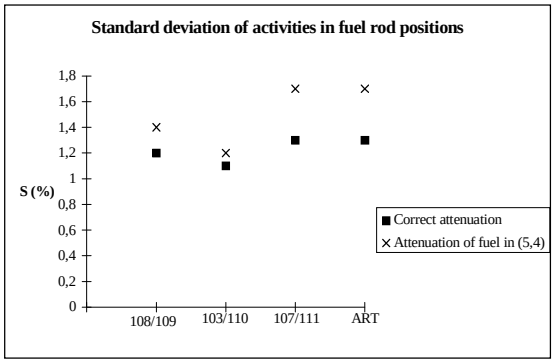

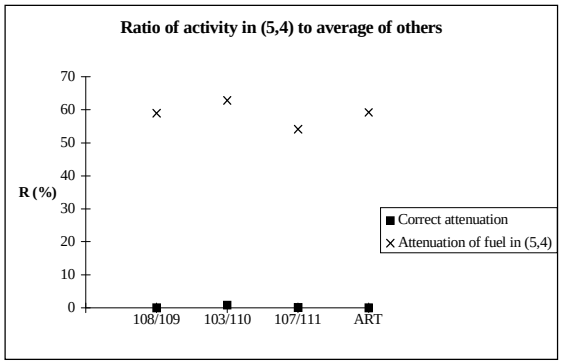

Figures 5.19-5.20. S and R under the assumption of correct attenuation and attenuation of fuel in the water channel. Note the drastically increased reconstructed activity in the position of the water channel under the assumption of attenuation of fuel.

Concluding this investigation, the reconstructed activity in the position of the water channel gets drastically higher when assuming attenuation of fuel, just as predicted in section 2.5. The value of R varies between 54 and 63 %, in the middle of the predicted interval, probably due to which projections being used. S also tends to get larger under the assumption of fuel in the water channel. This effect seems to appear from changes in the reconstructed activity in positions near the water channel, most affected by the wrong assumption.

5.7.2 Comparison between gamma energy 662 keV and 1274 keV

The simulations described so far have been made using a gamma energy of 662 keV, corresponding to the decay of Cs-137. The higher gamma energy of Eu-154 (1274 keV) implies larger penetrability. Therefore more information can be obtained from the inner parts of the assembly and the reconstructed activities should have the possibility of being more correct. The reconstructions in this investigation were all made using the EAC algorithm, 40 projections and 40 translations, $\Phi(0) = 6{,}0^o$ and $R_p = 0{,}05$. The simulated intensities were either from "Simul_Cs2" (662 keV) or "Simul_Eu2" (1274 keV), both simulating a 2 mm collimator and a water channel in position (5,4). The reconstructions were:

-EAC_Cs21_11_08: 662 keV, correct attenuation.
-EAC_Cs21_11_25: 662 keV, attenuation of fuel assumed in position (5,4).
-EAC_Eu21_11_01: 1274 keV, correct attenuation.
-EAC_Eu21_11_02: 1274 keV, attenuation of fuel assumed in position (5,4).

S and R for the mean activity values during the 30th iteration, can be found in table 5.19. R can also be found in figure 5.21.

Table 5.19. S and R under the assumption of correct attenuation and attenuation of fuel in the water channel.

	S (%)		**R (%)**	
	EAC_Cs21_11_08/25 (662 keV)	EAC_Eu21_11_01/02 (1274 keV)	EAC_Cs21_11_08/25 (662 keV)	EAC_Eu21_11_01/02 (1274 keV)
Correct attenuation	1,5	1,4	0,3	0,1
Attenuation of fuel in (5,4)	1,6	1,4	53,9	43,9

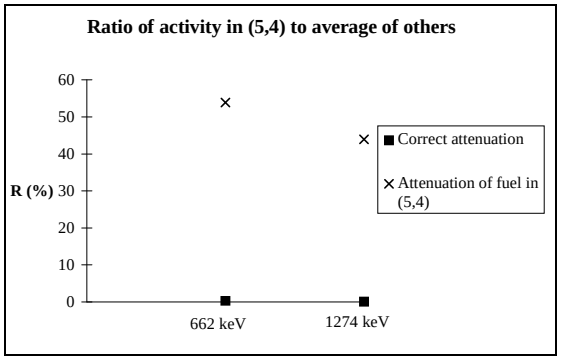

Figure 5.21. R under the assumption of correct attenuation and attenuation of fuel in the water channel. Note the smaller value of R for the higher gamma energy under the assumption of fuel in the water channel.

Just as predicted in section 2.5, the value of R is smaller for the reconstruction using the higher gamma energy. For both gamma energies, the values are in the middle of the predicted intervals. Since R seems to end up at a smaller value than the worst case predicted, even a higher value of S than the maximum 6 %, stated in section 2.6, can be accepted.

5.8 Number of projections and translations

An important subject in tomography is to determine the number of measurements needed to yield an acceptable reconstruction of the object, since it is desirable to limit the total measurement time. The reconstructions in this study have been made from simulated intensities using a 3 mm collimator from simulation "Simul_Cs3". Statistical variations with 1 % standard deviation in the simulated highest intensity measurement were added. The reconstructions were made from different sub-sets of the simulated intensities, chosen as evenly spaced assembly rotations and collimator translations. For all reconstructions, the views head-on a row of fuel rods were omitted, since the reconstructions in section 5.6 became better if an off-set angle was introduced. The reconstructions were made using the EAC algorithm with $R_p = 0{,}05$. The reconstructions were:

-EAC_Cs31_11_02:	40 projections and 60 translations. 100 iterations.
-EAC_Cs31_11_03:	40 projections and 30 translations. 200 iterations.
-EAC_Cs31_11_05:	40 projections and 20 translations. 125 iterations.
-EAC_Cs31_11_06:	30 projections and 20 translations. 150 iterations.
-EAC_Cs31_11_07:	24 projections and 20 translations. 200 iterations.
-EAC_Cs31_11_08:	30 projections and 30 translations. 125 iterations.
-EAC_Cs31_11_09:	24 projections and 30 translations. 150 iterations.
-EAC_Cs31_11_10:	20 projections and 30 translations. 200 iterations.
-EAC_Cs31_11_11:	30 projections and 15 translations. 200 iterations.
-EAC_Cs31_11_12:	24 projections and 15 translations. 250 iterations.
-EAC_Cs31_11_13:	30 projections and 12 translations. 250 iterations.
-EAC_Cs31_11_14:	60 projections and 10 translations. 200 iterations.
-EAC_Cs31_11_23:	30 projections and 40 translations. 120 iterations.
-EAC_Cs31_11_24:	24 projections and 40 translations. 120 iterations.
-EAC_Cs31_11_25:	40 projections and 15 translations. 200 iterations.
-EAC_Cs31_11_26:	30 projections and 60 translations. 100 iterations.
-EAC_Cs31_11_27:	24 projections and 60 translations. 100 iterations.
-EAC_Cs31_11_28:	60 projections and 30 translations. 100 iterations.
-EAC_Cs31_11_29:	60 projections and 20 translations. 150 iterations.

The number of iterations has been chosen large enough for the reconstructions to stabilise or, for the cases of slow convergence, the activity changes between consecutive iterations were considered negligible. The values of S and R have been calculated form the mean activities during the last iteration and can be found in tables 5.20 and 5.21. The effects of altering the number of projections have been visualised in figures 5.22 and 5.23 and the effects of altering the number of translations have been visualised in figures 5.24 and 5.25.

Table 5.20. S for various numbers of projections and translations.

	S (%)				
No of translations	60 projections	40 projections	30 projections	24 projections	20 projections
60	-	1,6	1,6	2,0	-
40	-	-	2,1	2,3	-
30	1,8	1,9	2,4	2,9	5,7
20	2,0	2,9	4,5	4,7	-
15	-	2,8	4,7	3,2	-
12	-	-	7,8	-	-
10	15,9	-	-	-	-

Table 5.21. R for various numbers of projections and translations.

	R (%)				
No of translations	60 projections	40 projections	30 projections	24 projections	20 projections
60	-	3,4	0,2	0,7	-
40	-	-	0,4	1,0	-
30	0,5	3,9	0,2	0,3	0,2
20	8,3	9,1	0,2	0,1	-
15	-	0,3	0,1	0,1	-
12	-	-	26,3	-	-
10	1,7	-	-	-	-

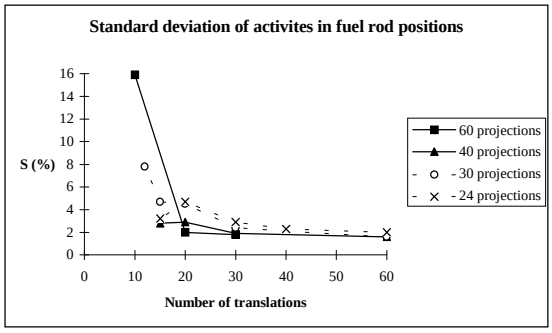

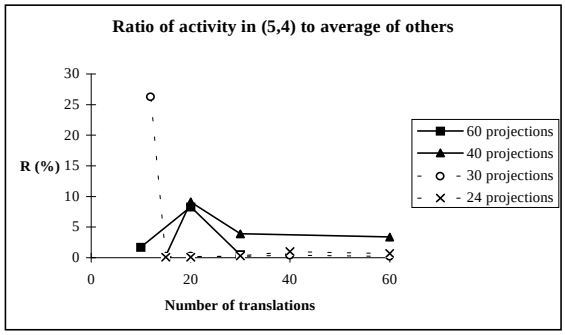

Figures 5.22 and 5.23. S and R as functions of the number of projections for various numbers of translations. Note the overall effect of smaller values of S and R with increasing number of translations.

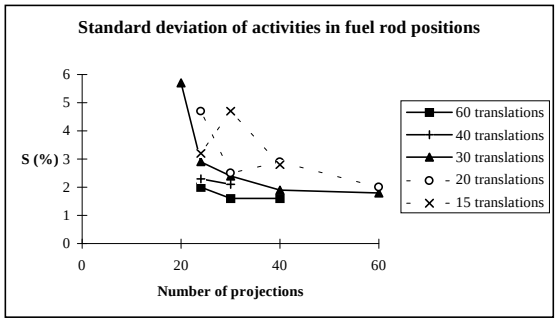

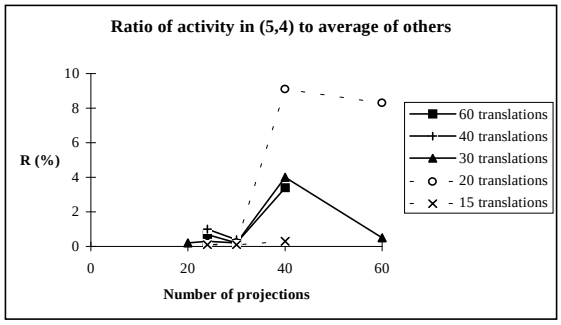

Figures 5.24 and 5.25. S and R as functions of the number of projections for various numbers of translations.

The results are in some ways ambiguous. Generally, the inclusion of more measurements results in a better reconstruction. This can be seen in figures 5.22, 5.23 and 5.24. In figure 5.25 though, there is an effect of getting larger values of R with increasing number of projections. There is also an implication of larger values of R when using 20 translations as well as 40 projections, possibly due to the inclusion

of too few measurements with large contributions from the inner parts of the assembly (see appendix 2). For most reconstructions though, R is below 6 %. According to section 2.6, with so small values of R, it is of more importance to keep S small. The analysis should therefore be concentrated on the tendencies in figures 5.22 and 5.24.

Figure 5.22 show a remarkable increase of S if the number of translations is decreased below 20, implying a distance of 9 mm between each measurement. For the simulated measurements, this is equal to the total width of sight at the assembly, penumbra included. To achieve better reliability of the reconstructions, the usage of at least about 30 translations is desirable. This conclusion results in the exclusion of the curves of 15 and 20 translations in figure 5.24. A threshold between 20 and 30 projections can then be seen, for which the smaller values show increasing values of S.

The recommendation from this study is thus to use at least 30 translations and 30 projections to yield reliable reconstructions. This makes a total number of measurements of at least 900. The discussion is only valid for the simulated measurement geometry, using a 3 mm collimator and 1 pixel per fuel rod.

5.9 Effects of assembly positioning

When performing the measurements, the rotation angle and the position of the assembly relative to the collimator and the detector have to be known for the contribution coefficients to be calculated correctly. The existing measurement equipment, described in section 2.2, does only offer means of determining rotations and translations relative to a reference position, having to be withheld from gamma-ray intensity measurements. The reference angle, 0^o, is chosen as the angle where the side of the assembly is orthogonal to the symmetry axis of the collimator. The reference translation is chosen as the position where the centre of the collimator points at the centre of the assembly.

In order to determine the effect of possible displacements upon the reconstructions, a study was performed based upon simulated intensities from simulation “Simul_Cs3_spec”. The intensities were simulated using a 3 mm collimator. 24 projections and 40 translations were used. Statistic variations with 1 % standard deviation in the highest intensity measurement were added. The reconstructions were made using the CAC algorithm, R_p = 0,50, 150 iterations and incorrectly assuming attenuation of fuel in the water channel. The reconstructions used in this study were:

-CAC_Cs31_113:	Correct position.
-CAC_Cs31_114:	Collimator translation displaced 1 mm.
-CAC_Cs31_115:	Collimator translation displaced 1 mm, assembly rotation displaced 1^o.
-CAC_Cs31_116:	Collimator translation displaced 2 mm.
-CAC_Cs31_117:	Collimator translation displaced 2 mm, assembly rotation displaced 1^o.
-CAC_Cs31_118:	Collimator translation displaced 3 mm.
-CAC_Cs31_119:	Assembly rotation displaced 1^o.
-CAC_Cs31_120:	Assembly rotation displaced 2^o.
-CAC_Cs31_121:	Assembly rotation displaced 3^o.
-CAC_Cs31_122:	Collimator translation displaced 2 mm, assembly rotation displaced 1^o. Only collimator translations -62 to +62 mm used.
-CAC_Cs31_123:	Collimator translation displaced 3 mm. Only collimator translations -62 to +62 mm used.

S and R for the mean activities during the last iteration can be found in tables 5.22-5.27 and in figures 5.26-5.31. The reconstructed activities from reconstructions CAC_Cs31_113, with correct positioning, and CAC_Cs31_117, with 2 mm translation and 1^o rotation displacement, can be found in appendix 5. The four corner rods are obviously most affected by the displacements. Therefore two different calculations of S and R have been made, namely including or excluding the corner rods.

Tables 5.22-5.24. S for various displacements.

S for correct rotation position (%)				
Translation displacement (mm)	0	1	2	3
Including corner rods	1,3	32,0	37,1	103,9
Excluding corner rods	1,4	14,5	12,7	19,8

S for correct translation position (%)				
Rotation displacement (^{o})	0	1	2	3
Including corner rods	1,3	6,2	20,2	89,7
Excluding corner rods	1,4	5,8	17,6	65,9

S for 1^o rotation displacement (%)			
Translation displacement (mm)	0	1	2
Including corner rods	6,2	24,1	181,3
Excluding corner rods	5,8	8,2	32,0

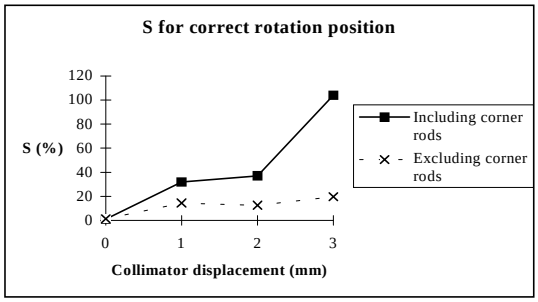

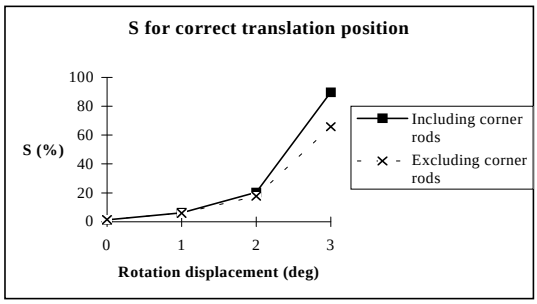

Tables 5.25-5.27. R for various displacements.

R for correct rotation position (%)				
Translation displacement (mm)	0	1	2	3
Including corner rods	60,6	76,4	97,7	94,9
Excluding corner rods	60,6	82,7	107,6	129,7

R for correct translation position (%)				
Rotation displacement (^{o})	0	1	2	3
Including corner rods	60,6	73,6	107,4	107,2
Excluding corner rods	60,6	74,1	110,8	132,5

R for 1^o rotation displacement (%)			
Translation displacement (mm)	0	1	2
Including corner rods	73,6	68,7	63,2
Excluding corner rods	74,1	73,0	119,2

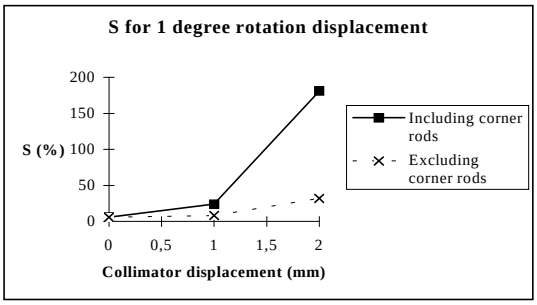

Figures 5.26-5.28. S for various displacements. Note the increasing values with larger displacements and also the smaller effect when excluding the corner rods.

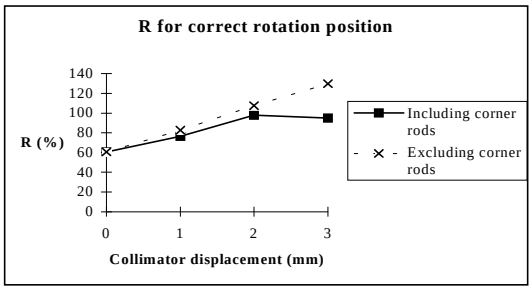

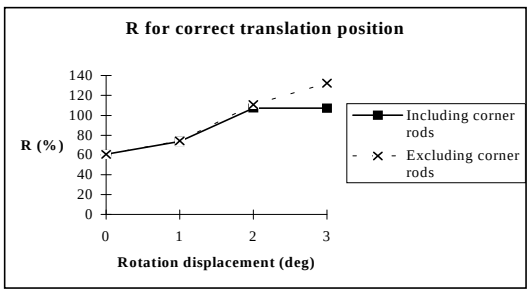

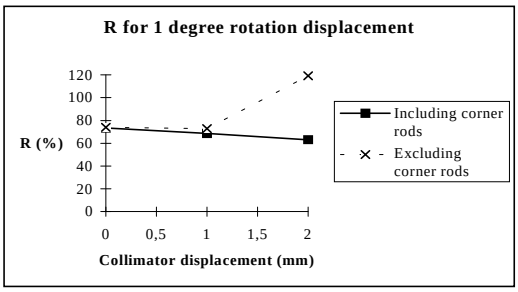

Figures 5.29-5.31. R for various displacements.

The enhancement of the reconstructed activities in the corner rods when displacements occur might be an effect of some peripheral positions measuring larger fractions of the corner rods than for the case of no displacements. This fact would effectively give a higher apparent activity of the corner rods. The final effect of the enhancement will be a strong increase of S. R will decrease, since the average activity is enhanced. As an attempt to deal with this problem, reconstructions were made using only central collimator translations, i. e. -62 to +62 mm. The results from these reconstructions are compared to the reconstructions with all translations included in tables 5.28-5.31 and in figures 5.32-5.35. In appendix 5, the reconstructed activity picture of EAC_Cs31_122, with only the central translations included, can be compared to EAC_Cs31_117, with all translations included.

Tables 5.28 and 5.29. S and R for 2 mm translation and 1^o rotation displacement.

S for 2 mm translation and 1^o rotation displacement (%)		
Collimator translations used	All	From -62 to +62 mm
Including corner rods	181,3	10,1
Excluding corner rods	32,0	10,4

R for 2 mm translation and 1^o rotation displacement (%)		
Collimator translations used	All	From -62 to +62 mm
Including corner rods	63,2	100,7
Excluding corner rods	119,2	100,8

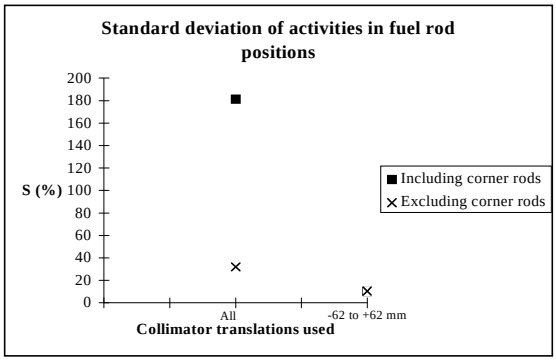

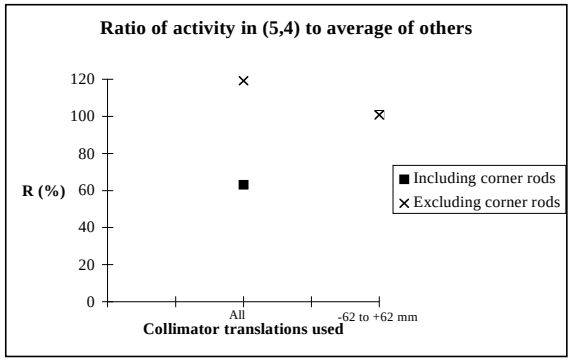

Figures 5.32 and 5.33. S and R for 2 mm translation and 1^o rotation displacement. Note the agreement between the cases of including and excluding the corner rods when using only the central translations.

Tables 5.30 and 5.31. S and R for 3 mm translation displacement.

S for 3 mm translation displacement (%)		
Collimator translations used	All	From -62 to +62 mm
Including corner rods	103,9	14,9
Excluding corner rods	19,8	15,2

R for 3 mm translation displacement (%)		
Collimator translations used	All	From -62 to +62 mm
Including corner rods	94,9	125,5
Excluding corner rods	129,7	125,0

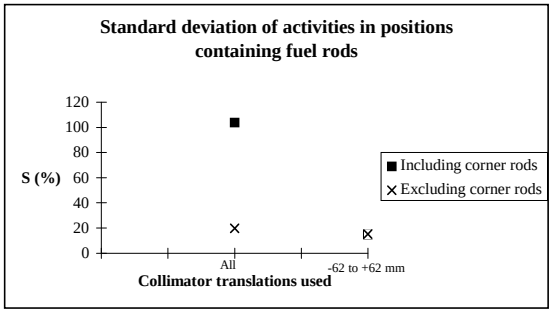

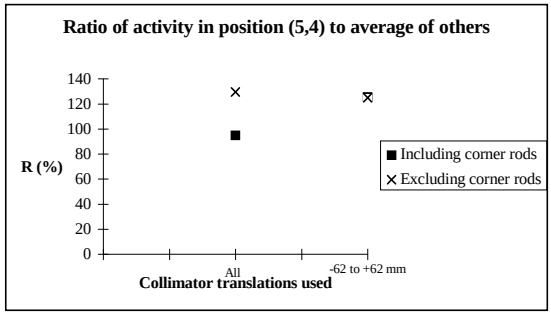

Figures 5.34 and 5.35. S and R for 3 mm translation displacement.

The reconstructions including only the central translations proved to be interesting, since the activities of the corner rods were not enhanced like for the reconstructions including all translations. This strategy

might also be useful to minimise effects of scattering, expected as similar enhancement of the intensities in the peripheral measurements.

From the results above clearly no large displacements can be allowed. At 1^o and 1 mm displacement it is still possible to detect a missing rod. However, the detection will become uncertain if the rods contain various activities, as is the case in reality. In a future measurement site the geometrical conditions must be determined with an even higher accuracy.

A displacement of the centre of rotation might also appear if the assembly is not centred in the rotation equipment. If this displacement is known, it can be corrected for the way described in appendix 3.

5.10 Choice of reconstruction algorithm

Three different reconstruction algorithms have been used for reconstructing the activity distribution from simulated intensities; the EAC, CAC and ART algorithms (see section 3.1). For some sets of data, reconstructions have been performed using all three algorithms, making a comparison between the algorithms possible. The sets of data used for the reconstructions were:

-40 projections and 30 translations from simulation “Simul_Cs3”
-30 projections and 20 translations from simulation “Simul_Cs3”
-28 projections and 40 translations from simulation “Simul_Cs3_spec”
-28 projections and 20 translations from simulation “Simul_Cs3_spec”
-24 projections and 20 translations from simulation “Simul_Cs3_spec”

The relaxation parameters found to be the best for each reconstruction in section 5.5 were used:

-EAC: $R_p = 0{,}05$
-CAC: $R_p = 0{,}50$
-ART: $R_p = (\text{ceil}(0{,}1*\text{iteration number}))^{-1}$

The only exception is the reconstruction from 40x30 simulated measurements using the CAC algorithm where $R_p = 0{,}40$. The results of the reconstructions can be found in tables 5.32-5.33, and in figures 5.36-5.37. For all reconstructions, the iterations were made until the activities of the pixels had stabilised.

Table 5.32. S using the three algorithms for various numbers of measurements.

	S (%)				
Algorithm	40x30	30x20	28x40	28x20	24x20
EAC	1,9	2,5	2,1	2,6	2,7
CAC	1,8	1,3	1,1	1,3	1,2
ART	1,4	1,4	1,1	1,3	1,3

Table 5.33. R using the three algorithms for various numbers of measurements.

	R (%)				
Algorithm	40x30	30x20	28x40	28x20	24x20
EAC	3,9	0,2	1,2	0,1	0,1
CAC	3,3	0,1	0,8	0,1	0
ART	3,2	0	0,2	0	0

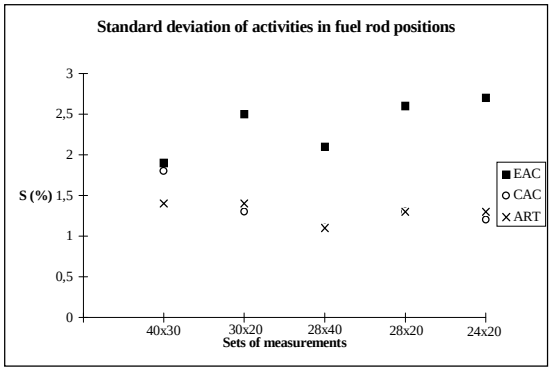

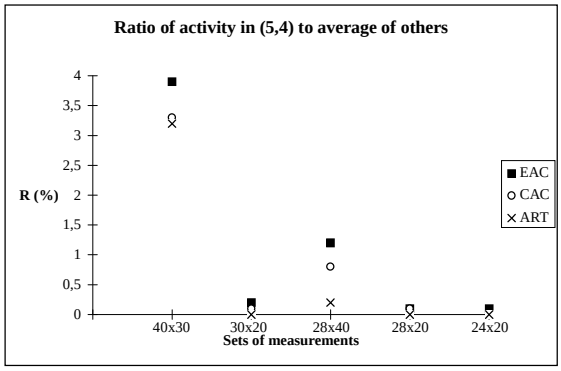

Figures 5.36 and 5.37. S and R using the three algorithms for various numbers of measurements. Note the smaller values of both S and R for the two contributional methods, CAC and ART.

For all reconstructions included in this study, the CAC and ART algorithms give smaller values of both S and R than the EAC algorithm. The ART algorithm seems to give slightly smaller values than the CAC algorithm, but on the other hand the reconstructions using the ART algorithm have had the advantage of using a varying relaxation parameter.

Probably the activity adjustments are preferably made using a contributional method. In this work though, most studies have been made using the EAC algorithm. The results of these studies are of general nature and should be applicable to reconstructions using the contributional methods, too.

6. Summary

The possibilities of detecting a missing rod in the inner parts of a nuclear fuel assembly, by means of tomographic measurements, have been examined. Algebraic tomographic algorithms have been used for the reconstructions. The algebraic algorithms rely on coefficients, describing the contribution from each picture element (pixel) to the total intensity in the detector in each measurement position. The contribution coefficients depend on attenuation and geometric conditions. Simulated gamma-ray intensity patterns from an 8x8 BWR fuel assembly with evenly distributed activity within and between the rods have been used for the reconstructions. The intensities have been simulated under the geometric conditions of an existing measurement equipment at CLAB in Oskarshamn, Sweden,

Two parameters were chosen to describe the quality of the reconstructions; S = the standard deviation of the reconstructed activities in the positions containing fuel rods and R = the ratio of the reconstructed activity in the position of a missing rod to the average of the reconstructed activities in the other positions. Theoretical considerations have been applied for determining the demands on the reconstructions for a missing rod to be confidently discerned. It has been discussed that the attenuation in the position of a missing rod must be considered unknown, leading to maximum values for both parameters of 6 %, under the assumption of a correct attenuation matrix.

In the reconstruction process, a start activity was chosen for every pixel. The reconstructed activities were then adjusted to show agreement with the simulated gamma-ray intensities. One iteration was considered completed when adjustments to all measurements had been made. The iterations were mostly continued until the pixel activities had stabilised. The mean values during the last iteration were used for the final results to yield activities best adapted to all measurements.

Three different algorithms have been used for the adjustments; the EAC algorithm, where the activities in all pixels contributing to the intensity are equally corrected, and the CAC and the ART algorithms, where the corrections are proportional to the contribution to the total intensity. The results of the reconstructions indicate that the contributional methods are to prefer. To decrease fluctuations during the activity corrections, a relaxation parameter can be used, with a value determined specifically for each reconstruction algorithm. A method of decreasing the relaxation parameter with increasing number of completed iterations showed the best results.

Strategies using various numbers of pixels have been tested, including 1x1, 4x4 and 8x8 pixels per unit cell. The reconstructions using 1x1 pixel per unit cell showed the best abilities of stabilising during the iterations. That pixel distribution was used for further studies with values of S and R

fulfilling the demands of the reconstructions,. The other methods can prove to be more useful for real measurements with varying activities within the rods.

The gamma energies of interest in this context is 661,6 keV, from the decay of Cs-137, and 1274,4 keV, from Eu-154. The larger penetrability of the 1274,4 keV gamma-rays enables more information from the inner parts of an assembly. In the reconstructions, smaller values of the parameters S and R were consequently yielded for the use of 1274,4 keV gamma-rays.

Geometric considerations were also made. The use of a wide collimator was shown to cause less quality on the information acquired and give rise to large values of S and R. It was also shown that the use of measurements with large contributions from the inner parts of the assembly increased the reliability of the reconstructions. The importance of the number of measurements for yielding small values of S and R was shown, with worse results using few measurements. For the simulated geometry, using a 3 mm collimator and 1 pixel per unit cell, at least about 1000 measurements per reconstruction was recommended, with about equal numbers of projections and translations. The knowledge of the exact position of the collimator and the detector relative to the assembly was found necessary for yielding good quality of the reconstructions.

The reconstructions from simulated intensities showed good possibilities of detecting a missing rod in the inner parts of a fuel assembly, with values of S and R well below the stipulated 6 %.

7. Discussions

The reconstructions in this work show good possibilities of detecting a missing rod in the central parts of the simulated fuel assembly. This fact can be interpreted as if the detection of a missing rod in a real measurement should be possible if all contributions to the measured intensity patterns are known. If the simulated intensity patterns are found to be in accordance with real conditions, the reconstruction algorithms developed in this work might prove to be applicable in their present appearance.

This work was based upon the geometric conditions of an existing measurement equipment at CLAB in Oskarshamn, Sweden. The equipment was built for gamma-scanning. It is therefore not optimised for tomographic measurements. It was concluded from the simulations that specified information from various parts of the assembly was useful. A more narrow geometry than the simulated is therefore expected to increase the possibility of yielding good quality of the reconstructions. A more narrow geometry is also expected to decrease the amount of scattered gamma quanta reaching the detector. A vision of a future detector arrangement can be found in figure 7.1.

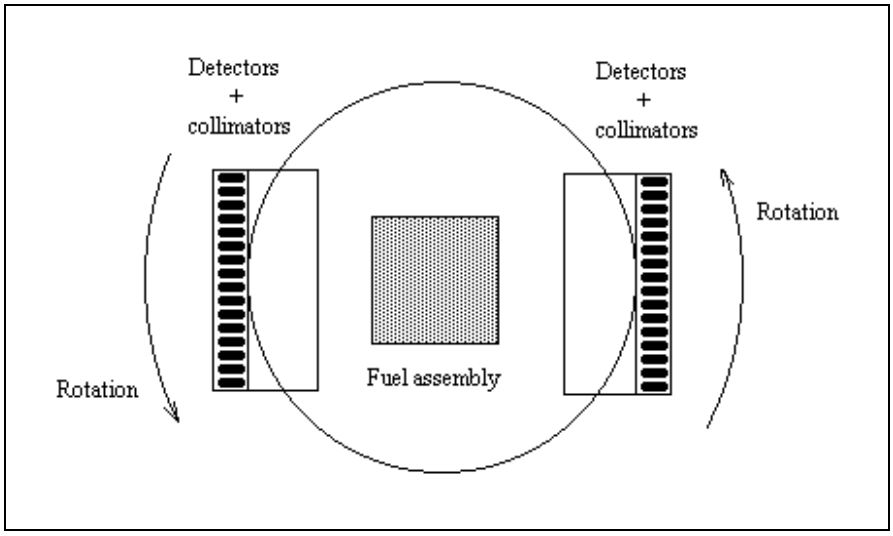

Figure 7.1. Vision of a future detector arrangement.

Future work should be made to verify the simulated intensities used for the reconstructions in this work. If further contributions to the intensities are found to be of importance, e. g. from elastically scattered gamma quanta, those should be included in the calculation of the contribution coefficients. Studies

should be made concerning the effects of varying activity concentration within and between the rods, the way expected for a real measurement situation.

8. Acknowledgements

This work has been financed by the Swedish Nuclear Power Inspectorate, SKI. The author also want to thank the supervisor Ane Håkansson and the examiner Anders Bäcklin, both from the Department of Radiation Sciences at Uppsala University, for their support.

9. References

(1) A. C. Kak, M. Slaney: *Principles of computerised tomographic imaging*, IEEE Press, New York, 1988.
(2) G. T. Herman: *Image reconstructions from projections*, Topics in Applied Physics, vol. 32, Springer-Verlag, Berlin, 1979.
(3) R. Duwe, P. Jansen: *Computer tomography of barrels with radioactive contents*, Nuclear Engineering and Design, vol. 130 (1), p. 89-102, 1991.
(4) A. Alexa, T. Craciunescu, G. Mateescu, R. Dobrin: *The tomographic maximum entropy method in the 3-D analysis of nuclear fuel pins*, Journal of Nuclear Materials, vol. 218, p. 139-142, 1995.
(5) C. M. Lederer, V. S. Shirley: *Table of Isotopes, 7th edition*, John Wiley & sons, New York, 1978.
(6) Philips: *Transmission of high-energy photons through various materials*.
(7) L. Råde, B. Westergren: *Beta, Mathematics handbook*, Studentlitteratur, Lund, 1990.
(8) A. Håkansson, A. Bäcklin: *Non-destructive assay of spent BWR fuel with high resolution gamma-ray spectroscopy*, May 1995, ISSN 1104-1374, ISRN SKI-R--95/19—SE

10. Appendices

Appendix 1. Determination of attenuation

Appendix 2. Determination of measurement positions with large contributions from the inner parts of the assemblies

Appendix 3. Displacement of the rotation centre

Appendix 4. Simulated intensities

Appendix 5. Examples of reconstructed activity pictures

Appendix 1. Determination of attenuation

Two methods, further described below, have been used for determining the attenuation of a gamma-ray between a pixel and the detector. For both methods, the direction of the ray within the fuel assembly is of interest. To make the determination of this direction possible, two coordinate systems are introduced; one system, (x,y), following the assembly rotation and one fixed system, (**X**,**Y**). Both systems have their origin in the assembly centre. The coordinate systems are shown in figure 10.1.

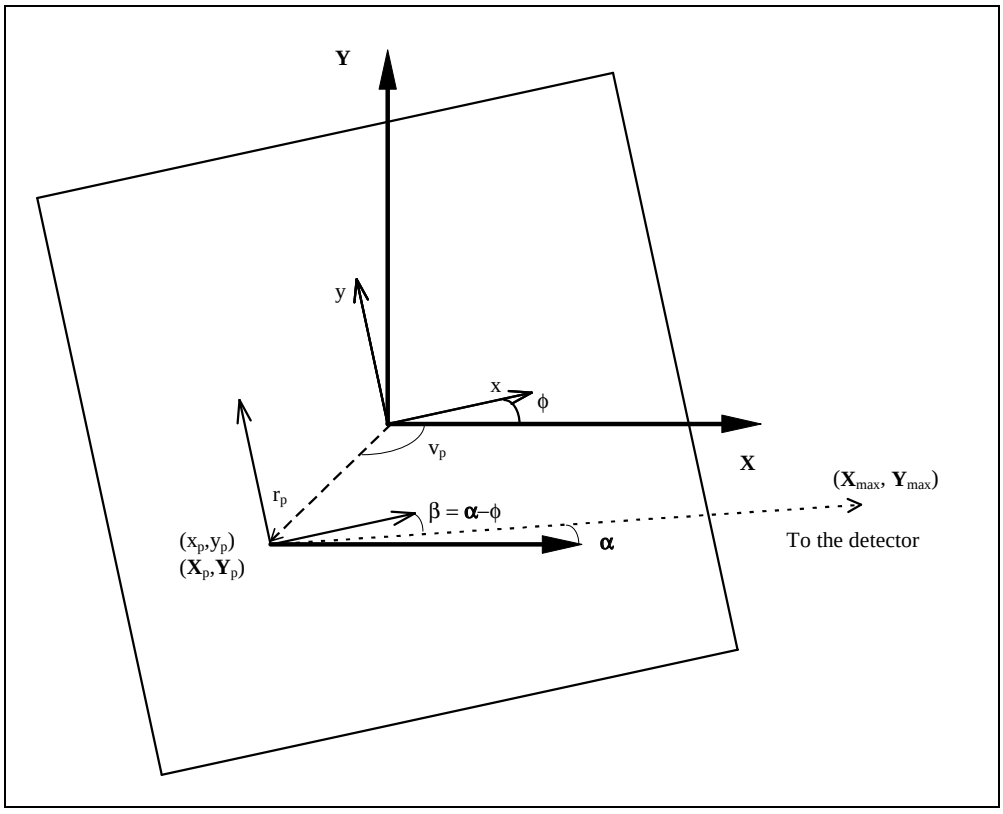

Figure 10.1. The coordinate systems used for the calculations.

The pixel coordinates are set in the (x,y)-system, and the transformation to the (**X**,**Y**)-system is made according to:

$$\mathbf{X}_p = r_p * \cos(\phi + v_p) \qquad \text{where} \qquad v_p = \arctan\left(\frac{x}{y}\right)$$

$$\mathbf{Y}_p = r_p * \sin(\phi + v_p) \qquad r_p = \sqrt{x^2 + y^2}$$

ϕ = rotation angle

The angle between the **X**-axis and the gamma ray is equal to: $\alpha = \arctan\left(\frac{\mathbf{Y}_{det} - \mathbf{Y}_p}{\mathbf{X}_{det} - \mathbf{X}_p}\right)$.

The possibility for a gamma-ray to reach the detector can be determined by knowing the size and position of the collimator, using the angle α. The angle between the ray and the x-axis, used for following the ray in the (x,y)-system, is then equal to $\beta = \alpha - \phi$. For both methods used for determining the attenuation, the rays are only followed until a chosen value of **X**, large enough for the ray to have left the assembly. From $\mathbf{X}_{max}$ the attenuation is approximately equal for all rays. The calculated attenuation should therefore be corrected with a scaling factor, but since only relative values of simulated intensities and reconstructed activities are of interest, this scaling factor is omitted.

Method 1: The assembly is stepped through in small steps adding attenuation in every step.

The assembly is divided into a narrow grid. The crossing of a ray through the grid is simulated in steps, where the nearest pixel centre is determined for every step, adding the attenuation of that pixel. The step, Δr, is set equal to the length of the side of a pixel. The principle is shown in figure 10.2, where a ray crossing a unit cell is visualised. For the calculations in this work, there are more gridpoints than in figure 10.2, typically 50x50 pixels per unit cell.

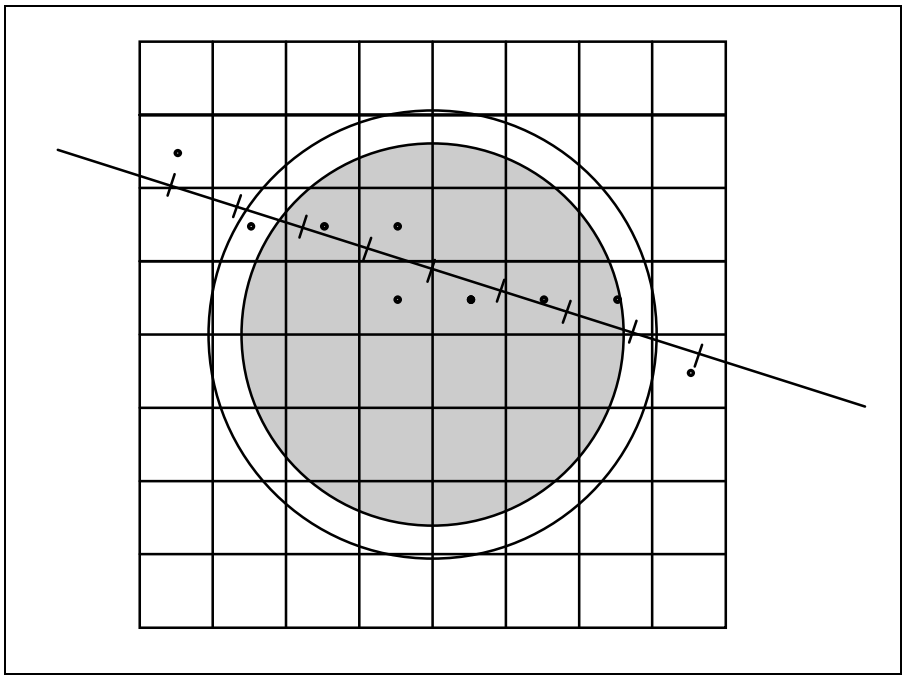

Figure 10.2. Determination of attenuation by traversing an assembly in small steps.

The ray is followed until $\mathbf{X}_{max}$- = (assembly side)*$\sqrt{2}$ mm. The coordinate system is shown in figure 10.1. The attenuation of the ray is calculated according to $e^{-\sum_i \mu_i * \Delta r}$

Method 2. Analytic determination.

The distance a ray has to travel through each material is determined analytically. This is made in the following steps:

1. The **Y**-coordinate, $\mathbf{Y}_{max}$, corresponding to $\mathbf{X}_{max}$ is determined.
2. The distance, $\mathbf{R}_{tot}$, between the pixel and ($\mathbf{X}_{max}$,$\mathbf{Y}_{max}$) is determined.
3. The straight-line equation, $y = k_b x + m_b$, of the beam in the (x,y)-system is determined.
4. Rods with **X**-coordinates of the centre larger than $\mathbf{X}_p$ are chosen.
5. The nearest distance between the ray and the rod centre is determined for the chosen rods.
6. If the nearest distance < the zircaloy radius, the ray's crossing points with the zircaloy's outer edge is determined.
7. If the nearest distance < the fuel radius, the ray's crossing points with the fuel's outer edge is determined.
8. The ray's travel length in fuel is calculated.
9. The ray's travel length in zircaloy is calculated.
10. The ray's crossing points with the edges of fuel and zircaloy in the source rod is determined.
11. The ray's travel lengths in fuel and zircaloy are calculated for the source rod.
12. The ray's total travel lengths in zircaloy and fuel is calculated.
13. The ray's travel length in water is calculated.
14. The attenuation of the ray is calculated.

In figure 10.3, the steps above are visualised. For clarity, step 4 and 5 is only visualised for some rods.

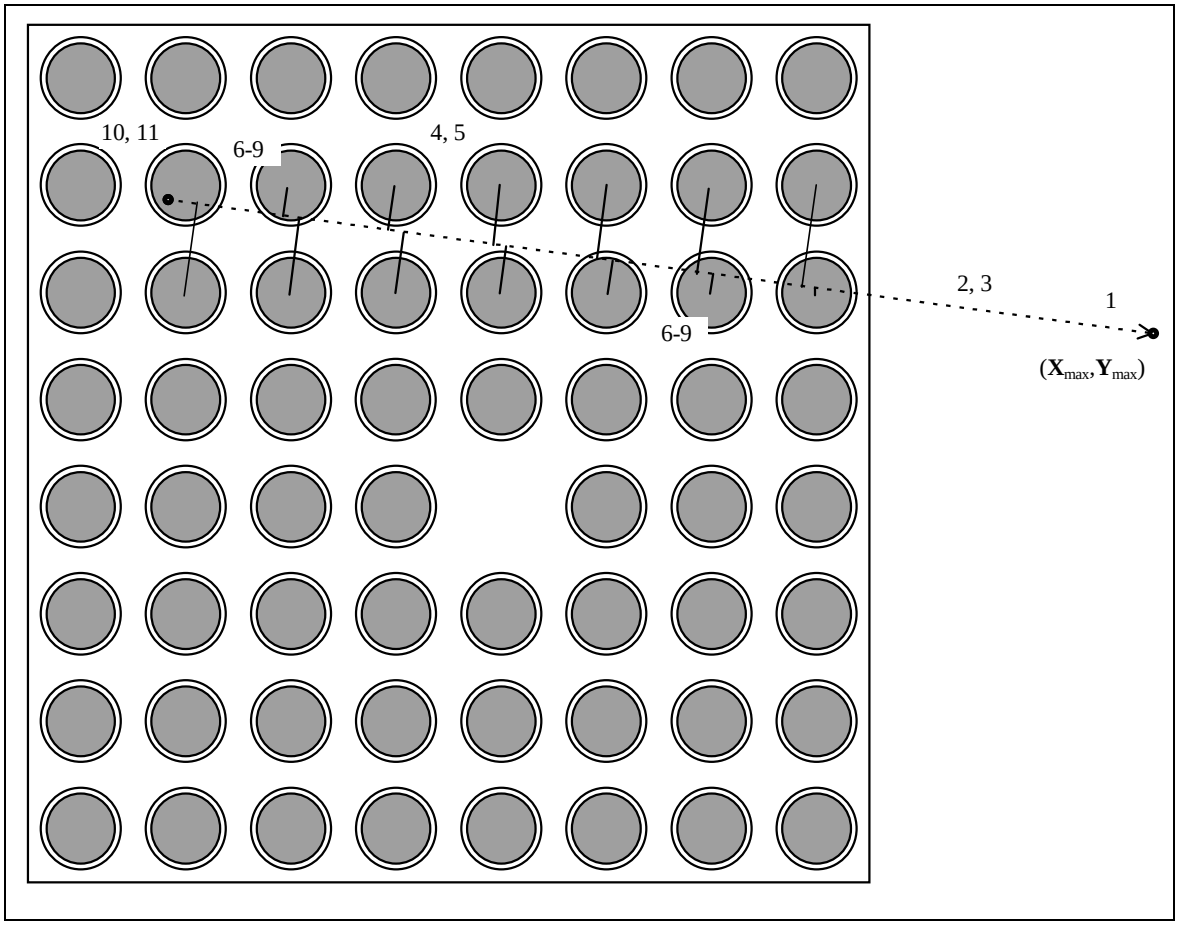

Figure 10.3. Analytic calculation of the contribution coefficients.

The details about the steps are the following:

1. $\mathbf{Y}_{max} = \mathbf{Y}_p + \frac{\mathbf{X}_{max} - \mathbf{X}_p}{\mathbf{X}_{det} - \mathbf{X}_p} * (\mathbf{Y}_{det} - \mathbf{Y}_p)$
2. $\mathbf{R}_{tot} = \sqrt{(\mathbf{X}_{max} - \mathbf{X}_p)^2 + (\mathbf{Y}_{max} - \mathbf{Y}_p)^2}$
3. $k_b = \tan \beta$
   $m_b = y_p - k_b * x_p$
4. $\mathbf{X}_c$ of the rod centres are determined by transformation from (x_c,y_c) and compared to $\mathbf{X}_p$.
5. The straight-line equation of the nearest line, $y = k_n * x + m_n$ is yielded from:
   $k_n = -k_b^{-1}$
   $m_n = y_c - k_n * x_c$
   The coordinates of the crossings between the ray and the nearest line:
   $x_{cross} = \frac{m_n - m_b}{k_b - k_n}$
   $y_{cross} = k_b * x_{cross} + m_b$
   The nearest distance to a rod centre is then equal to $\sqrt{(x_{cross} - x_c)^2 + (y_{cross} - y_c)^2}$
   (If $k_b = 0$, the crossing coordinates are: $x_{cross} = x_c$
   $y_{cross} = y_p$.)
6. The equation of the edge of the zircaloy is $(x - x_c)^2 + (y - y_c)^2 = r_{zirc}^2$
   The determination of the crossing points between zircaloy edge and $y = k_b * x + m_b$ yields a second degree equation with solutions:

$$x_{1,2} = -\frac{b}{2a} \pm \sqrt{\left(\frac{b}{2a}\right)^2 - \frac{c}{a}} \qquad \text{where} \qquad a = k_b^{\,2} + 1$$

$$y_{1,2} = k_b * x_{1,2} + m_b \qquad b = 2*(k_b*m_b - k_b*y_c - x_c)$$

$$c = x_c^{\,2} + y_c^{\,2} + m_b^{\,2} - r_{zirc}^{\,2} - 2*y_c*m_b$$

7. This step is equal to step 6, where r_{zirc} is to be exchanged to r_{fuel}.
8. The ray's travel length in fuel for each rod is equal to the distance between the fuel crossing points:
$$l_f = \sqrt{(x_{f1} - x_{f2})^2 + (y_{f1} - y_{f2})^2}$$
9. The ray's travel length in zircaloy for each rod is equal to the distance between the zircaloy crossing points minus the travel length in fuel:
$$l_z = \sqrt{(x_{z1} - x_{z2})^2 + (y_{z1} - y_{z2})^2} - l_f$$
10. Steps 6 and 7 are made for the source rod.
11. The **X**-coordinates of the ray's crossing points with fuel and zircaloy in the source rod are determined, and the biggest coordinate belongs to the crossing point in the direction towards the detector. The travel lengths are:
$$l_f = \sqrt{(x_f - x_p)^2 + (y_f - y_p)^2}$$
$$l_z = \sqrt{(x_z - x_p)^2 + (y_z - y_p)^2} - l_f$$
12. For the rods not crossed by the ray, the travel length is set to 0. The total travel lengths in fuel and zircaloy are:
$$l_{f,tot} = \Sigma\, l_f$$
$$l_{z,tot} = \Sigma\, l_z$$
13. The travel length in water is equal to $l_w = \mathbf{R}_{tot} - l_{f,tot} - l_{z,tot}$
14. The attenuation of the ray is then equal to $e^{-\mu_w * l_w + \mu_f * l_{f,tot} + \mu_z * l_{z,tot}}$

Comparison between method 1 and method 2.

To control the calculations, the contribution coefficients calculated using the two methods were compared for some detector positions. The test was made using 1 pixel per unit cell. The results were presented as contribution in per mil of total. Some of it can be found in figures 10.4 and 10.5.

Analytically determined coefficients

Y_{det}: 0.0160 m
Rotation angle: 0.00000 rad
Coefficients in per mil of total:

0	0	0	0	0	0	0	0
0	0	0	0	0	0	0	0
2	4	7	13	27	57	122	268
2	4	7	13	27	57	122	268
0	0	0	0	0	0	0	0
0	0	0	0	0	0	0	0
0	0	0	0	0	0	0	0
0	0	0	0	0	0	0	0

Pixel value 1000 (total) is above equal to: 0.13798557E-04

Y_{det}: 0.0160 m
Rotation angle: 0.38397 rad
Coefficients in per mil of total:

0	0	0	0	0	0	0	0
3	2	0	0	0	0	0	0
0	0	10	26	0	0	0	0
0	0	0	0	18	176	90	0
0	0	0	0	0	0	6	670
0	0	0	0	0	0	0	0
0	0	0	0	0	0	0	0
0	0	0	0	0	0	0	0

Pixel value 1000 (total) is above equal to: 0.86503987E-04

Y_{det}: 0.0160 m
Rotation angle: 0.78540 rad
Coefficients in per mil of total:

0	1	2	0	0	0	0	0
0	0	3	5	0	0	0	0
0	0	0	7	10	0	0	0
0	0	0	0	20	25	0	0
0	0	0	0	0	56	64	0
0	0	0	0	0	0	161	167
0	0	0	0	0	0	0	478
0	0	0	0	0	0	0	0

Pixel value 1000 (total) is above equal to: 0.76989550E-04

Figure 10.4. Contribution coefficients calculated using the analytic method for collimator translation +16 mm and assembly rotations 0^o, 22^o and 45^o.

Coefficients calculated by stepping through the assembly

Y_{det}: 0.0160 m
Rotation angle: 0.00000 rad
Coefficients in per mil of total:

0	0	0	0	0	0	0	0
0	0	0	0	0	0	0	0
1	3	6	12	26	56	123	274
1	3	6	12	26	56	123	274
0	0	0	0	0	0	0	0
0	0	0	0	0	0	0	0
0	0	0	0	0	0	0	0
0	0	0	0	0	0	0	0

Pixel value 1000 (total) is above equal to: 0.13505329E-04

Y_{det}: 0.0160 m
Rotation angle: 0.38397 rad
Coefficients in per mil of total:

0	0	0	0	0	0	0	0
3	2	0	0	0	0	0	0
0	0	10	26	0	0	0	0
0	0	0	0	18	176	89	0
0	0	0	0	0	0	6	670
0	0	0	0	0	0	0	0
0	0	0	0	0	0	0	0
0	0	0	0	0	0	0	0

Pixel value 1000 (total) is above equal to: 0.86466043E-04

Y_{det}: 0.0160 m
Rotation angle: 0.78540 rad
Coefficients in per mil of total:

0	1	2	0	0	0	0	0
0	0	3	5	0	0	0	0
0	0	0	8	10	0	0	0
0	0	0	0	20	25	0	0
0	0	0	0	0	57	64	0
0	0	0	0	0	0	161	167
0	0	0	0	0	0	0	477
0	0	0	0	0	0	0	0

Pixel value 1000 (total) is above equal to: 0.77089473E-04

Figure 10.5. Contribution coefficients calculated by stepping through the assembly for collimator translation +16 mm and assembly rotations 0^o, 22^o and 45^o.

Figures 10.4 and 10.5 show very good agreement between the two methods. The analytic method can be assumed to be most exact, since the travel lengths through the various materials are free from approximations. It should be noted that the inclusion of e. g. effects of elastic scattering can make the calculations more exact. Another benefit with the analytic method is the shorter calculations times compared to the first method. For the case of stepping through a grid of 400x400 pixels, the analytic method is about 3 times faster.

The simulated intensities were all calculated using the attenuation calculation method of stepping through the assembly, being the first method developed. The reconstructions were performed altering the two methods. In appendix 5, figure 10.10, a picture is shown of the reconstructed activity distribution obtained using the method of stepping through the assembly. It can be compared to figure 10.11, where a reconstructed picture is shown obtained using the analytic method, otherwise based upon exactly the same data. The similarity between the two pictures again indicate the agreement between the two methods of determining the attenuation.

Appendix 2. Determination of measurement positions with large contributions from the inner parts of the assemblies.

The first investigation in section 5.6 indicated possibilities of yielding more accurate reconstructions if measurements with large contributions from the inner parts of the fuel assemblies were used. Therefore a study of the contributions from the inner parts in different measurement positions was carried out. The study was made on a standard fuel assembly, shown in figure 2.1 in section 2.1, from simulated contributions using a 3 mm collimator. Since an assembly is symmetric in steps of 45^o (except for the position of the water channel), the study was limited to rotation angles between 0^o and 45^o. The collimator position was limited to translations between 0 and +16 mm. The angular step was 1^o, and the translation step was 1 mm. The largest contributions during the translations are shown in table 10.1 and figure 10.6 for various rotation angles.

Table 10.1. Largest contributions from rods in the 3rd, 4th and 5th row for varying rotation angles.

	Largest contributions during translations in per mil of total		
Angle (^{o})	3rd row	4th row	5th row
0	98	43	20
1	131	83	64
2	143	123	114
3	158	148	136
4	186	177	164
5	219	211	185
6	254	238	172
7	287	256	148
8	324	249	121
9	350	231	99
10	363	212	77
11	375	187	62
12	375	168	48
13	366	145	38
14	348	127	31
15	332	107	29
16	312	91	32
17	289	77	39
18	266	67	45
19	245	62	52
20	222	64	54
21	203	72	51
22	184	84	46
23	170	98	39
24	158	111	34
25	149	119	32
26	145	122	31
27	144	120	30
28	143	111	28
29	146	97	29
30	151	81	31
31	160	65	33
32	172	52	34
33	182	46	31
34	190	47	26
35	194	50	20
36	197	56	16
37	197	63	16
38	193	68	18
39	184	72	22
40	171	74	25
41	152	71	28
42	133	66	28
43	108	54	26
44	85	37	18
45	64	22	8

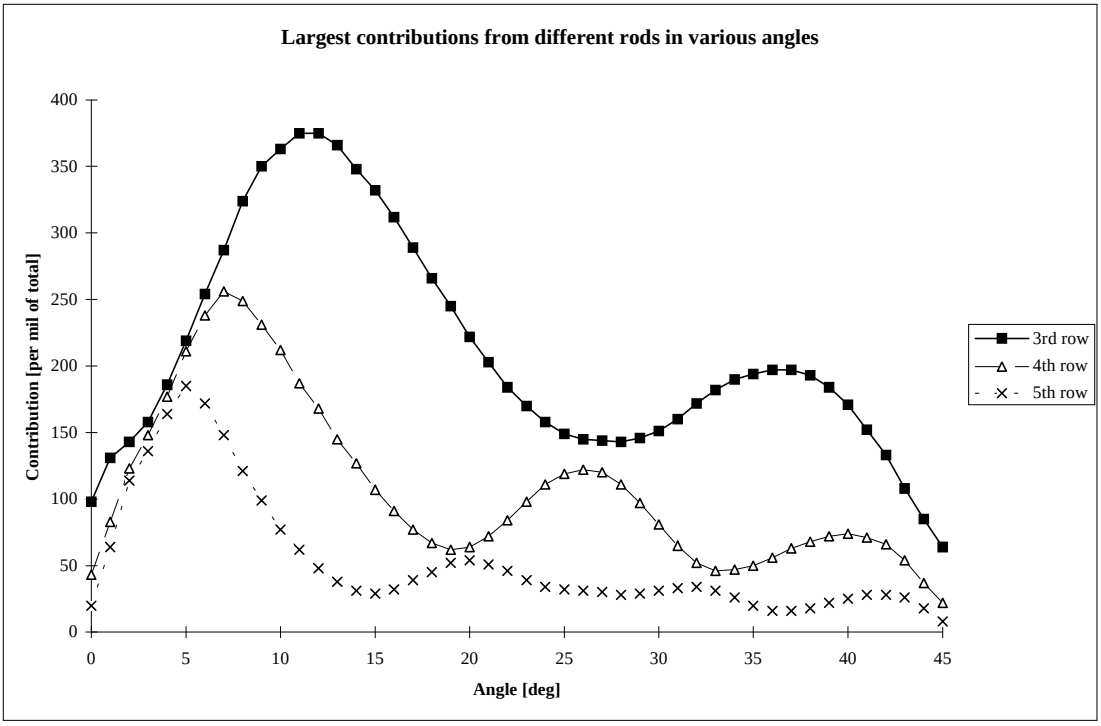

Figure 10.6. Largest contributions from rods in the 3rd, 4th and 5th row for varying projection angles.

The peaks in figure 10.6 were further investigated concerning corresponding collimator translations. The results can be found in table 10.2, rounded to whole mm. Symmetries have also been used for determining positions with maximum contributions for angles between 45° and 90°.

Table 10.2. Projection angles and collimator translations corresponding to peaks in figure 10.6.

Angle of peak [°]	Row	Collimator translations [mm]			
5	5th	-28	-12	4	20
7	4th	-26	-10	6	22
11 to 12	3rd	**-21**	**-5**	**10**	**26**
20	5th	-26	-11	4	19
26	4th	**-18**	-4	**10**	24
32	5th	-26	-12	2	16
36 to 37	3rd	-2	8	21	34
40	4th	**-11**	**1**	**13**	**25**
41 to 42	5th	**-10**	**2**	**14**	**26**
48 to 49	5th	-26	-14	-2	10
50	4th	-25	-13	-1	11
53 to 54	3rd	-34	-21	-8	2
58	5th	-16	-2	12	26
64	4th	-24	-10	4	18
70	5th	**-19**	-4	**11**	**26**
78 to 79	3rd	-26	-10	5	21
83	4th	**-22**	**-6**	**10**	**26**
85	5th	-20	-4	12	28

The results above were used for choosing a suitable set of measurement positions, using equally spaced angles and translations. According to section 5.8, at least about 900 measurements are needed to yield reliable reconstructions. The chosen set included 1120 measurement positions and can be found in table 10.3.

Table 10.3. Angles and translations chosen to give maximum contributions from the inner parts of a fuel assembly.

Chosen angles [^{o}]	Chosen translations [mm]
11	-78
26	-74
41	.
56	.
71	-18
86	-14
101	-10
116	-6
131	-2
146	2
.	6
.	10
356	14
	18
83	.
173	.
263	74
353	78

The number of chosen rotation angles is 28 and the number of translations is 40. The 24 first angles were chosen in steps of 15^o. Note the four extra angles, corresponding to maximum contribution from the fuel rods in the 4^{th} row. These four extra angles are omitted in some reconstructions. In table 10.2, the peak contribution positions within 1^o and 1 mm from a chosen measurement position are marked with bold figures.

Appendix 3. Displacement of the rotation centre

As pointed out in section 2.2, the rotation centre might not coincide with the centre of the fuel assembly. If this displacement is known, it can be accounted for. In order to determine a possible displacement of the rotation centre, the position of the centre of the assembly has been calculated as a function of displacement and rotation.

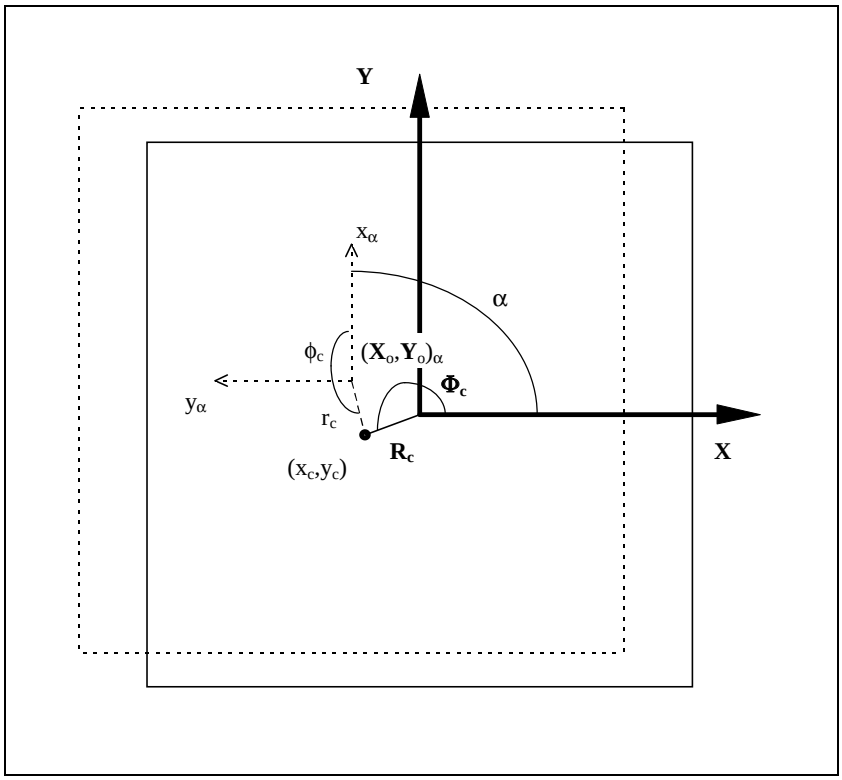

Figure 10.7. Rotation of the assembly for the case of a displaced rotation centre. In the figure, an example where the assembly has rotated the angle $\alpha = 90^o$ is marked.

Two coordinate systems, shown in figure 10.7, are used for the calculations. The same systems have been used for the determination of the attenuation (see appendix 1). The origins of the two systems coincide for the rotation angle $\alpha = 0$. The (**X**,**Y**)-system is an inertial system while the (x,y)-system follows the assembly during rotation, with the origin in the centre of the assembly. The position of the rotation centre will be independent of the rotation angle in both coordinate systems, implying $(x_c,y_c) = (\mathbf{X}_c,\mathbf{Y}_c)$. Consequently, the same goes for the polar coordinates $(r_c,\phi_c) = (\mathbf{R_c},\mathbf{\Phi_c})$. By starting out from the rotation centre, the position of the origin, $(\mathbf{X}_o,\mathbf{Y}_o)_\alpha$, of the (x,y)-system in the (**X**,**Y**)-system can be determined as a function of the rotation angle, α:

$$\mathbf{X}_o(\alpha) = \mathbf{X}_c + r_c*\cos(\alpha + (\phi_c - 180^o)) = x_c - r_c*\cos(\phi_c + \alpha)$$
$$\mathbf{Y}_o(\alpha) = \mathbf{Y}_c + r_c*\sin(\alpha + (\phi_c - 180^o)) = y_c - r_c*\sin(\phi_c + \alpha)$$

For rotation angles multiples of 90^o, the values of $\mathbf{X}_o$ and $\mathbf{Y}_o$ are described by the simple expressions:

$\mathbf{X}_o(0^o) = 0$	$\mathbf{Y}_o(0^o) = 0$
$\mathbf{X}_o(90^o) = x_c + y_c$	$\mathbf{Y}_o(90^o) = y_c - x_c$
$\mathbf{X}_o(180^o) = 2x_c$	$\mathbf{Y}_o(180^o) = 2y_c$
$\mathbf{X}_o(270^o) = x_c - y_c$	$\mathbf{Y}_o(270^o) = y_c + x_c$

From experimental data, the values of $\mathbf{Y}_o$ for these angles can be obtained. The displacement parameters x_c and y_c can then be calculated.

Appendix 4. Simulated intensities.

The simulated intensity patterns are here shown for assembly rotations 0^o and 45^o, using collimator widths 1, 2, 3 and 5 mm. The distance between consecutive simulated collimator translations is 1 mm. The simulated fuel assembly is described in section 4.3. The relative intensities can be found in tables 10.4-10.5 and in figures 10.8-10.9.

Table 10.4. Simulated relative intensities at 0^o assembly rotation for four different collimator widths.

Intensities at 0° rotation									
Translation [m]	1 mm collimator	2 mm collimator	3 mm collimator	5 mm collimator	Translation [m]	1 mm collimator	2 mm collimator	3 mm collimator	5 mm collimator
-0,090	0,00E+00	0,00E+00	0,00E+00	0,00E+00	0,001	0,00E+00	4,17E-01	2,76E+00	1,74E+01
-0,089	0,00E+00	0,00E+00	0,00E+00	0,00E+00	0,002	1,57E-01	1,71E+00	4,79E+00	1,94E+01
-0,088	0,00E+00	0,00E+00	0,00E+00	0,00E+00	0,003	7,94E-01	3,28E+00	7,40E+00	2,23E+01
-0,087	0,00E+00	0,00E+00	0,00E+00	0,00E+00	0,004	1,51E+00	5,02E+00	1,01E+01	2,61E+01
-0,086	0,00E+00	0,00E+00	0,00E+00	0,00E+00	0,005	1,72E+00	6,33E+00	1,28E+01	3,04E+01
-0,085	0,00E+00	0,00E+00	0,00E+00	0,00E+00	0,006	1,79E+00	7,02E+00	1,46E+01	3,43E+01
-0,084	0,00E+00	0,00E+00	0,00E+00	0,00E+00	0,007	1,81E+00	7,02E+00	1,57E+01	3,67E+01
-0,083	0,00E+00	0,00E+00	0,00E+00	0,00E+00	0,008	1,78E+00	7,15E+00	1,59E+01	3,76E+01
-0,082	0,00E+00	0,00E+00	0,00E+00	0,00E+00	0,009	1,81E+00	7,02E+00	1,57E+01	3,67E+01
-0,081	0,00E+00	0,00E+00	0,00E+00	0,00E+00	0,010	1,79E+00	7,02E+00	1,46E+01	3,43E+01
-0,080	0,00E+00	0,00E+00	0,00E+00	0,00E+00	0,011	1,72E+00	6,33E+00	1,28E+01	3,04E+01
-0,079	0,00E+00	0,00E+00	0,00E+00	0,00E+00	0,012	1,51E+00	5,02E+00	1,01E+01	2,61E+01
-0,078	0,00E+00	0,00E+00	0,00E+00	0,00E+00	0,013	7,94E-01	3,28E+00	7,40E+00	2,24E+01
-0,077	0,00E+00	0,00E+00	0,00E+00	0,00E+00	0,014	1,57E-01	1,71E+00	4,79E+00	1,95E+01
-0,076	0,00E+00	0,00E+00	0,00E+00	0,00E+00	0,015	0,00E+00	4,17E-01	2,77E+00	1,75E+01
-0,075	0,00E+00	0,00E+00	0,00E+00	0,00E+00	0,016	0,00E+00	7,66E-03	2,09E+00	1,66E+01
-0,074	0,00E+00	0,00E+00	0,00E+00	0,00E+00	0,017	0,00E+00	4,26E-01	2,79E+00	1,75E+01
-0,073	0,00E+00	0,00E+00	0,00E+00	0,00E+00	0,018	1,60E-01	1,73E+00	4,83E+00	1,95E+01
-0,072	0,00E+00	0,00E+00	0,00E+00	0,00E+00	0,019	8,06E-01	3,31E+00	7,45E+00	2,24E+01
-0,071	0,00E+00	0,00E+00	0,00E+00	0,00E+00	0,020	1,53E+00	5,06E+00	1,02E+01	2,62E+01
-0,070	0,00E+00	0,00E+00	0,00E+00	0,00E+00	0,021	1,72E+00	6,36E+00	1,28E+01	3,05E+01
-0,069	0,00E+00	0,00E+00	0,00E+00	0,00E+00	0,022	1,79E+00	7,04E+00	1,46E+01	3,44E+01
-0,068	0,00E+00	0,00E+00	0,00E+00	1,59E-01	0,023	1,81E+00	7,03E+00	1,58E+01	3,69E+01
-0,067	0,00E+00	0,00E+00	0,00E+00	9,68E-01	0,024	1,78E+00	7,16E+00	1,60E+01	3,77E+01
-0,066	0,00E+00	0,00E+00	0,00E+00	2,57E+00	0,025	1,81E+00	7,03E+00	1,58E+01	3,69E+01
-0,065	0,00E+00	0,00E+00	2,03E-01	4,99E+00	0,026	1,79E+00	7,04E+00	1,46E+01	3,44E+01
-0,064	0,00E+00	4,65E-03	1,05E+00	8,31E+00	0,027	1,72E+00	6,36E+00	1,28E+01	3,05E+01
-0,063	0,00E+00	4,26E-01	2,59E+00	1,25E+01	0,028	1,53E+00	5,06E+00	1,02E+01	2,62E+01
-0,062	1,60E-01	1,73E+00	4,83E+00	1,70E+01	0,029	8,06E-01	3,31E+00	7,45E+00	2,25E+01
-0,061	8,06E-01	3,31E+00	7,45E+00	2,15E+01	0,030	1,60E-01	1,73E+00	4,83E+00	1,96E+01
-0,060	1,53E+00	5,06E+00	1,02E+01	2,60E+01	0,031	0,00E+00	4,26E-01	2,79E+00	1,75E+01
-0,059	1,72E+00	6,36E+00	1,28E+01	3,05E+01	0,032	0,00E+00	9,32E-03	2,10E+00	1,66E+01
-0,058	1,79E+00	7,04E+00	1,46E+01	3,44E+01	0,033	0,00E+00	4,26E-01	2,79E+00	1,75E+01
-0,057	1,81E+00	7,03E+00	1,58E+01	3,69E+01	0,034	1,60E-01	1,73E+00	4,83E+00	1,96E+01
-0,056	1,78E+00	7,16E+00	1,60E+01	3,77E+01	0,035	8,06E-01	3,31E+00	7,45E+00	2,25E+01
-0,055	1,81E+00	7,03E+00	1,58E+01	3,69E+01	0,036	1,53E+00	5,06E+00	1,02E+01	2,62E+01
-0,054	1,79E+00	7,04E+00	1,46E+01	3,44E+01	0,037	1,72E+00	6,36E+00	1,28E+01	3,05E+01
-0,053	1,72E+00	6,36E+00	1,28E+01	3,05E+01	0,038	1,79E+00	7,04E+00	1,46E+01	3,44E+01
-0,052	1,53E+00	5,06E+00	1,02E+01	2,62E+01	0,039	1,81E+00	7,03E+00	1,58E+01	3,69E+01
-0,051	8,06E-01	3,31E+00	7,45E+00	2,25E+01	0,040	1,78E+00	7,16E+00	1,60E+01	3,77E+01
-0,050	1,60E-01	1,73E+00	4,83E+00	1,95E+01	0,041	1,81E+00	7,03E+00	1,58E+01	3,69E+01
-0,049	0,00E+00	4,26E-01	2,79E+00	1,75E+01	0,042	1,79E+00	7,04E+00	1,46E+01	3,44E+01
-0,048	0,00E+00	9,31E-03	2,10E+00	1,66E+01	0,043	1,72E+00	6,36E+00	1,28E+01	3,05E+01
-0,047	0,00E+00	4,26E-01	2,79E+00	1,75E+01	0,044	1,53E+00	5,06E+00	1,02E+01	2,62E+01
-0,046	1,60E-01	1,73E+00	4,83E+00	1,95E+01	0,045	8,06E-01	3,31E+00	7,45E+00	2,25E+01
-0,045	8,06E-01	3,31E+00	7,45E+00	2,25E+01	0,046	1,60E-01	1,73E+00	4,83E+00	1,95E+01
-0,044	1,53E+00	5,06E+00	1,02E+01	2,62E+01	0,047	0,00E+00	4,26E-01	2,79E+00	1,75E+01
-0,043	1,72E+00	6,36E+00	1,28E+01	3,05E+01	0,048	0,00E+00	9,31E-03	2,10E+00	1,66E+01
-0,042	1,79E+00	7,04E+00	1,46E+01	3,44E+01	0,049	0,00E+00	4,26E-01	2,79E+00	1,75E+01
-0,041	1,81E+00	7,03E+00	1,58E+01	3,69E+01	0,050	1,60E-01	1,73E+00	4,83E+00	1,95E+01
-0,040	1,78E+00	7,16E+00	1,60E+01	3,77E+01	0,051	8,06E-01	3,31E+00	7,45E+00	2,25E+01
-0,039	1,81E+00	7,03E+00	1,58E+01	3,69E+01	0,052	1,53E+00	5,06E+00	1,02E+01	2,62E+01
-0,038	1,79E+00	7,04E+00	1,46E+01	3,44E+01	0,053	1,72E+00	6,36E+00	1,28E+01	3,05E+01
-0,037	1,72E+00	6,36E+00	1,28E+01	3,05E+01	0,054	1,79E+00	7,04E+00	1,46E+01	3,44E+01
-0,036	1,53E+00	5,06E+00	1,02E+01	2,62E+01	0,055	1,81E+00	7,03E+00	1,58E+01	3,69E+01
-0,035	8,06E-01	3,31E+00	7,45E+00	2,25E+01	0,056	1,78E+00	7,16E+00	1,60E+01	3,77E+01
-0,034	1,60E-01	1,73E+00	4,83E+00	1,96E+01	0,057	1,81E+00	7,03E+00	1,58E+01	3,69E+01
-0,033	0,00E+00	4,26E-01	2,79E+00	1,75E+01	0,058	1,79E+00	7,04E+00	1,46E+01	3,44E+01
-0,032	0,00E+00	9,32E-03	2,10E+00	1,66E+01	0,059	1,72E+00	6,36E+00	1,28E+01	3,05E+01
-0,031	0,00E+00	4,26E-01	2,79E+00	1,75E+01	0,060	1,53E+00	5,06E+00	1,02E+01	2,60E+01
-0,030	1,60E-01	1,73E+00	4,83E+00	1,96E+01	0,061	8,06E-01	3,31E+00	7,45E+00	2,15E+01
-0,029	8,06E-01	3,31E+00	7,45E+00	2,25E+01	0,062	1,60E-01	1,73E+00	4,83E+00	1,70E+01
-0,028	1,53E+00	5,06E+00	1,02E+01	2,62E+01	0,063	0,00E+00	4,26E-01	2,59E+00	1,25E+01
-0,027	1,72E+00	6,36E+00	1,28E+01	3,05E+01	0,064	0,00E+00	4,65E-03	1,05E+00	8,31E+00
-0,026	1,79E+00	7,04E+00	1,46E+01	3,44E+01	0,065	0,00E+00	0,00E+00	2,03E-01	4,99E+00
-0,025	1,81E+00	7,03E+00	1,58E+01	3,69E+01	0,066	0,00E+00	0,00E+00	0,00E+00	2,57E+00
-0,024	1,78E+00	7,16E+00	1,60E+01	3,77E+01	0,067	0,00E+00	0,00E+00	0,00E+00	9,68E-01
-0,023	1,81E+00	7,03E+00	1,58E+01	3,69E+01	0,068	0,00E+00	0,00E+00	0,00E+00	1,59E-01
-0,022	1,79E+00	7,04E+00	1,46E+01	3,44E+01	0,069	0,00E+00	0,00E+00	0,00E+00	0,00E+00
-0,021	1,72E+00	6,36E+00	1,28E+01	3,05E+01	0,070	0,00E+00	0,00E+00	0,00E+00	0,00E+00
-0,020	1,53E+00	5,06E+00	1,02E+01	2,62E+01	0,071	0,00E+00	0,00E+00	0,00E+00	0,00E+00
-0,019	8,06E-01	3,31E+00	7,45E+00	2,24E+01	0,072	0,00E+00	0,00E+00	0,00E+00	0,00E+00
-0,018	1,60E-01	1,73E+00	4,83E+00	1,95E+01	0,073	0,00E+00	0,00E+00	0,00E+00	0,00E+00
-0,017	0,00E+00	4,26E-01	2,79E+00	1,74E+01	0,074	0,00E+00	0,00E+00	0,00E+00	0,00E+00
-0,016	0,00E+00	1,05E-02	2,07E+00	1,65E+01	0,075	0,00E+00	0,00E+00	0,00E+00	0,00E+00
-0,015	0,00E+00	4,09E-01	2,74E+00	1,74E+01	0,076	0,00E+00	0,00E+00	0,00E+00	0,00E+00
-0,014	1,54E-01	1,69E+00	4,74E+00	1,93E+01	0,077	0,00E+00	0,00E+00	0,00E+00	0,00E+00
-0,013	7,83E-01	3,25E+00	7,35E+00	2,22E+01	0,078	0,00E+00	0,00E+00	0,00E+00	0,00E+00
-0,012	1,50E+00	4,98E+00	1,00E+01	2,59E+01	0,079	0,00E+00	0,00E+00	0,00E+00	0,00E+00
-0,011	1,71E+00	6,29E+00	1,27E+01	3,02E+01	0,080	0,00E+00	0,00E+00	0,00E+00	0,00E+00
-0,010	1,78E+00	6,99E+00	1,45E+01	3,41E+01	0,081	0,00E+00	0,00E+00	0,00E+00	0,00E+00
-0,009	1,80E+00	6,99E+00	1,56E+01	3,65E+01	0,082	0,00E+00	0,00E+00	0,00E+00	0,00E+00
-0,008	1,77E+00	7,12E+00	1,59E+01	3,74E+01	0,083	0,00E+00	0,00E+00	0,00E+00	0,00E+00
-0,007	1,80E+00	6,99E+00	1,56E+01	3,65E+01	0,084	0,00E+00	0,00E+00	0,00E+00	0,00E+00
-0,006	1,78E+00	6,99E+00	1,45E+01	3,41E+01	0,085	0,00E+00	0,00E+00	0,00E+00	0,00E+00
-0,005	1,71E+00	6,29E+00	1,27E+01	3,02E+01	0,086	0,00E+00	0,00E+00	0,00E+00	0,00E+00
-0,004	1,50E+00	4,98E+00	1,00E+01	2,59E+01	0,087	0,00E+00	0,00E+00	0,00E+00	0,00E+00
-0,003	7,83E-01	3,25E+00	7,35E+00	2,22E+01	0,088	0,00E+00	0,00E+00	0,00E+00	0,00E+00
-0,002	1,54E-01	1,69E+00	4,74E+00	1,93E+01	0,089	0,00E+00	0,00E+00	0,00E+00	0,00E+00
-0,001	0,00E+00	4,09E-01	2,73E+00	1,73E+01	0,090	0,00E+00	0,00E+00	0,00E+00	0,00E+00
0,000	0,00E+00	8,84E-03	2,06E+00	1,64E+01					

Table 10.5. Simulated relative intensities at 45^o assembly rotation for four different collimator widths.

Intensities at 45° rotation									
Translation [m]	1 mm collimator	2 mm collimator	3 mm collimator	5 mm collimator	Translation [m]	1 mm collimator	2 mm collimator	3 mm collimator	5 mm collimator
-0,090	0,00E+00	0,00E+00	0,00E+00	5,00E-01	0,001	2,09E+00	8,37E+00	1,85E+01	4,54E+01
-0,089	0,00E+00	0,00E+00	0,00E+00	1,15E+00	0,002	2,09E+00	8,21E+00	1,72E+01	4,48E+01
-0,088	0,00E+00	0,00E+00	9,17E-02	2,23E+00	0,003	1,98E+00	7,45E+00	1,55E+01	4,32E+01
-0,087	0,00E+00	1,81E-02	4,22E-01	3,62E+00	0,004	1,68E+00	5,98E+00	1,39E+01	4,22E+01
-0,086	0,00E+00	1,86E-01	1,11E+00	5,32E+00	0,005	9,60E-01	4,91E+00	1,30E+01	4,18E+01
-0,085	6,00E-02	7,01E-01	2,04E+00	7,19E+00	0,006	6,87E-01	4,64E+00	1,28E+01	4,13E+01
-0,084	3,39E-01	1,31E+00	3,10E+00	9,10E+00	0,007	1,42E+00	5,18E+00	1,28E+01	4,08E+01
-0,083	5,80E-01	2,06E+00	4,24E+00	1,10E+01	0,008	1,79E+00	6,37E+00	1,38E+01	4,06E+01
-0,082	7,08E-01	2,60E+00	5,32E+00	1,26E+01	0,009	1,89E+00	7,45E+00	1,53E+01	4,14E+01
-0,081	7,50E-01	2,97E+00	6,15E+00	1,42E+01	0,010	1,93E+00	7,67E+00	1,67E+01	4,19E+01
-0,080	7,93E-01	3,05E+00	6,67E+00	1,51E+01	0,011	1,94E+00	7,67E+00	1,72E+01	4,18E+01
-0,079	7,82E-01	3,11E+00	6,74E+00	1,58E+01	0,012	1,98E+00	7,78E+00	1,70E+01	4,17E+01
-0,078	7,70E-01	3,05E+00	6,51E+00	1,62E+01	0,013	1,88E+00	7,58E+00	1,63E+01	4,11E+01
-0,077	7,31E-01	2,88E+00	5,92E+00	1,64E+01	0,014	1,89E+00	7,11E+00	1,47E+01	4,00E+01
-0,076	6,71E-01	2,43E+00	5,39E+00	1,67E+01	0,015	1,69E+00	5,99E+00	1,32E+01	3,89E+01
-0,075	5,03E-01	1,96E+00	5,12E+00	1,72E+01	0,016	1,06E+00	4,78E+00	1,21E+01	3,83E+01
-0,074	2,56E-01	1,83E+00	5,28E+00	1,80E+01	0,017	6,41E-01	4,33E+00	1,18E+01	3,79E+01
-0,073	3,70E-01	2,16E+00	5,75E+00	1,87E+01	0,018	1,03E+00	4,49E+00	1,17E+01	3,74E+01
-0,072	8,03E-01	2,78E+00	6,47E+00	1,96E+01	0,019	1,58E+00	5,48E+00	1,21E+01	3,72E+01
-0,071	9,82E-01	3,63E+00	7,49E+00	2,05E+01	0,020	1,68E+00	6,43E+00	1,35E+01	3,74E+01
-0,070	1,06E+00	4,09E+00	8,55E+00	2,16E+01	0,021	1,75E+00	6,90E+00	1,47E+01	3,79E+01
-0,069	1,09E+00	4,31E+00	9,30E+00	2,23E+01	0,022	1,75E+00	7,01E+00	1,55E+01	3,79E+01
-0,068	1,10E+00	4,33E+00	9,60E+00	2,26E+01	0,023	1,76E+00	6,96E+00	1,55E+01	3,77E+01
-0,067	1,09E+00	4,32E+00	9,41E+00	2,30E+01	0,024	1,77E+00	6,96E+00	1,50E+01	3,76E+01
-0,066	1,07E+00	4,20E+00	8,76E+00	2,31E+01	0,025	1,70E+00	6,62E+00	1,38E+01	3,66E+01
-0,065	1,00E+00	3,77E+00	7,94E+00	2,29E+01	0,026	1,62E+00	5,74E+00	1,24E+01	3,56E+01
-0,064	8,70E-01	3,05E+00	7,25E+00	2,31E+01	0,027	1,22E+00	4,59E+00	1,12E+01	3,48E+01
-0,063	4,70E-01	2,61E+00	7,10E+00	2,34E+01	0,028	5,96E-01	3,99E+00	1,07E+01	3,43E+01
-0,062	3,96E-01	2,68E+00	7,33E+00	2,38E+01	0,029	7,28E-01	3,93E+00	1,05E+01	3,39E+01
-0,061	8,05E-01	3,19E+00	7,78E+00	2,43E+01	0,030	1,32E+00	4,60E+00	1,08E+01	3,35E+01
-0,060	1,15E+00	4,01E+00	8,68E+00	2,50E+01	0,031	1,52E+00	5,61E+00	1,17E+01	3,36E+01
-0,059	1,23E+00	4,76E+00	9,77E+00	2,59E+01	0,032	1,55E+00	6,14E+00	1,30E+01	3,41E+01
-0,058	1,25E+00	5,02E+00	1,08E+01	2,66E+01	0,033	1,60E+00	6,30E+00	1,38E+01	3,43E+01
-0,057	1,28E+00	5,10E+00	1,12E+01	2,69E+01	0,034	1,58E+00	6,34E+00	1,40E+01	3,41E+01
-0,056	1,28E+00	5,08E+00	1,12E+01	2,70E+01	0,035	1,57E+00	6,26E+00	1,38E+01	3,39E+01
-0,055	1,26E+00	5,00E+00	1,06E+01	2,73E+01	0,036	1,57E+00	6,13E+00	1,28E+01	3,34E+01
-0,054	1,23E+00	4,64E+00	9,74E+00	2,70E+01	0,037	1,49E+00	5,44E+00	1,15E+01	3,22E+01
-0,053	1,11E+00	3,96E+00	8,83E+00	2,70E+01	0,038	1,26E+00	4,42E+00	1,04E+01	3,16E+01
-0,052	7,72E-01	3,20E+00	8,34E+00	2,72E+01	0,039	6,71E-01	3,67E+00	9,75E+00	3,10E+01
-0,051	4,18E-01	3,10E+00	8,47E+00	2,73E+01	0,040	5,63E-01	3,49E+00	9,44E+00	3,07E+01
-0,050	7,57E-01	3,40E+00	8,80E+00	2,78E+01	0,041	1,02E+00	3,86E+00	9,53E+00	3,04E+01
-0,049	1,25E+00	4,26E+00	9,55E+00	2,83E+01	0,042	1,31E+00	4,71E+00	1,03E+01	3,01E+01
-0,048	1,37E+00	5,19E+00	1,07E+01	2,93E+01	0,043	1,40E+00	5,43E+00	1,13E+01	3,06E+01
-0,047	1,39E+00	5,60E+00	1,18E+01	3,02E+01	0,044	1,44E+00	5,64E+00	1,23E+01	3,06E+01
-0,046	1,42E+00	5,72E+00	1,25E+01	3,05E+01	0,045	1,44E+00	5,71E+00	1,26E+01	3,06E+01
-0,045	1,44E+00	5,71E+00	1,26E+01	3,06E+01	0,046	1,42E+00	5,72E+00	1,25E+01	3,05E+01
-0,044	1,44E+00	5,64E+00	1,23E+01	3,06E+01	0,047	1,39E+00	5,60E+00	1,18E+01	3,02E+01
-0,043	1,40E+00	5,43E+00	1,13E+01	3,06E+01	0,048	1,37E+00	5,19E+00	1,07E+01	2,93E+01
-0,042	1,31E+00	4,71E+00	1,03E+01	3,01E+01	0,049	1,25E+00	4,26E+00	9,55E+00	2,83E+01
-0,041	1,02E+00	3,86E+00	9,53E+00	3,04E+01	0,050	7,57E-01	3,40E+00	8,80E+00	2,78E+01
-0,040	5,63E-01	3,49E+00	9,44E+00	3,07E+01	0,051	4,18E-01	3,10E+00	8,47E+00	2,73E+01
-0,039	6,71E-01	3,67E+00	9,75E+00	3,10E+01	0,052	7,72E-01	3,20E+00	8,34E+00	2,72E+01
-0,038	1,26E+00	4,42E+00	1,04E+01	3,16E+01	0,053	1,11E+00	3,96E+00	8,83E+00	2,70E+01
-0,037	1,49E+00	5,44E+00	1,15E+01	3,22E+01	0,054	1,23E+00	4,64E+00	9,74E+00	2,70E+01
-0,036	1,57E+00	6,13E+00	1,28E+01	3,34E+01	0,055	1,26E+00	5,00E+00	1,06E+01	2,73E+01
-0,035	1,57E+00	6,26E+00	1,38E+01	3,39E+01	0,056	1,28E+00	5,08E+00	1,12E+01	2,70E+01
-0,034	1,58E+00	6,34E+00	1,40E+01	3,41E+01	0,057	1,28E+00	5,10E+00	1,12E+01	2,69E+01
-0,033	1,60E+00	6,30E+00	1,38E+01	3,43E+01	0,058	1,25E+00	5,02E+00	1,08E+01	2,66E+01
-0,032	1,55E+00	6,14E+00	1,30E+01	3,41E+01	0,059	1,23E+00	4,76E+00	9,77E+00	2,59E+01
-0,031	1,52E+00	5,61E+00	1,17E+01	3,36E+01	0,060	1,15E+00	4,01E+00	8,68E+00	2,50E+01
-0,030	1,32E+00	4,60E+00	1,08E+01	3,35E+01	0,061	8,05E-01	3,19E+00	7,78E+00	2,43E+01
-0,029	7,28E-01	3,93E+00	1,05E+01	3,39E+01	0,062	3,96E-01	2,68E+00	7,33E+00	2,38E+01
-0,028	5,96E-01	3,99E+00	1,07E+01	3,43E+01	0,063	4,70E-01	2,61E+00	7,10E+00	2,34E+01
-0,027	1,22E+00	4,59E+00	1,12E+01	3,48E+01	0,064	8,70E-01	3,05E+00	7,25E+00	2,31E+01
-0,026	1,62E+00	5,74E+00	1,24E+01	3,56E+01	0,065	1,00E+00	3,77E+00	7,94E+00	2,29E+01
-0,025	1,70E+00	6,62E+00	1,38E+01	3,66E+01	0,066	1,07E+00	4,20E+00	8,76E+00	2,31E+01
-0,024	1,77E+00	6,96E+00	1,50E+01	3,76E+01	0,067	1,09E+00	4,32E+00	9,41E+00	2,30E+01
-0,023	1,76E+00	6,96E+00	1,55E+01	3,77E+01	0,068	1,10E+00	4,33E+00	9,60E+00	2,26E+01
-0,022	1,75E+00	7,01E+00	1,55E+01	3,79E+01	0,069	1,09E+00	4,31E+00	9,30E+00	2,23E+01
-0,021	1,75E+00	6,90E+00	1,47E+01	3,79E+01	0,070	1,06E+00	4,09E+00	8,55E+00	2,16E+01
-0,020	1,68E+00	6,43E+00	1,35E+01	3,74E+01	0,071	9,82E-01	3,63E+00	7,49E+00	2,05E+01
-0,019	1,58E+00	5,48E+00	1,21E+01	3,72E+01	0,072	8,03E-01	2,78E+00	6,47E+00	1,96E+01
-0,018	1,03E+00	4,49E+00	1,17E+01	3,74E+01	0,073	3,70E-01	2,16E+00	5,75E+00	1,87E+01
-0,017	6,41E-01	4,33E+00	1,18E+01	3,79E+01	0,074	2,56E-01	1,83E+00	5,28E+00	1,80E+01
-0,016	1,06E+00	4,78E+00	1,21E+01	3,83E+01	0,075	5,03E-01	1,96E+00	5,12E+00	1,72E+01
-0,015	1,69E+00	5,99E+00	1,32E+01	3,89E+01	0,076	6,71E-01	2,43E+00	5,39E+00	1,67E+01
-0,014	1,89E+00	7,11E+00	1,47E+01	4,00E+01	0,077	7,31E-01	2,88E+00	5,92E+00	1,64E+01
-0,013	1,88E+00	7,58E+00	1,63E+01	4,11E+01	0,078	7,70E-01	3,05E+00	6,51E+00	1,62E+01
-0,012	1,98E+00	7,78E+00	1,70E+01	4,17E+01	0,079	7,82E-01	3,11E+00	6,74E+00	1,58E+01
-0,011	1,94E+00	7,67E+00	1,72E+01	4,18E+01	0,080	7,93E-01	3,05E+00	6,67E+00	1,51E+01
-0,010	1,93E+00	7,67E+00	1,67E+01	4,19E+01	0,081	7,50E-01	2,97E+00	6,15E+00	1,42E+01
-0,009	1,89E+00	7,45E+00	1,53E+01	4,14E+01	0,082	7,08E-01	2,60E+00	5,32E+00	1,26E+01
-0,008	1,79E+00	6,37E+00	1,38E+01	4,06E+01	0,083	5,80E-01	2,06E+00	4,24E+00	1,10E+01
-0,007	1,42E+00	5,18E+00	1,28E+01	4,08E+01	0,084	3,39E-01	1,31E+00	3,10E+00	9,10E+00
-0,006	6,87E-01	4,64E+00	1,28E+01	4,13E+01	0,085	6,00E-02	7,01E-01	2,04E+00	7,19E+00
-0,005	9,60E-01	4,91E+00	1,30E+01	4,18E+01	0,086	0,00E+00	1,86E-01	1,11E+00	5,32E+00
-0,004	1,68E+00	5,98E+00	1,39E+01	4,22E+01	0,087	0,00E+00	1,81E-02	4,22E-01	3,62E+00
-0,003	1,98E+00	7,45E+00	1,55E+01	4,32E+01	0,088	0,00E+00	0,00E+00	9,17E-02	2,23E+00
-0,002	2,09E+00	8,21E+00	1,72E+01	4,48E+01	0,089	0,00E+00	0,00E+00	0,00E+00	1,15E+00
-0,001	2,09E+00	8,37E+00	1,85E+01	4,54E+01	0,090	0,00E+00	0,00E+00	0,00E+00	5,00E-01
0,000	2,18E+00	8,57E+00	1,87E+01	4,56E+01					

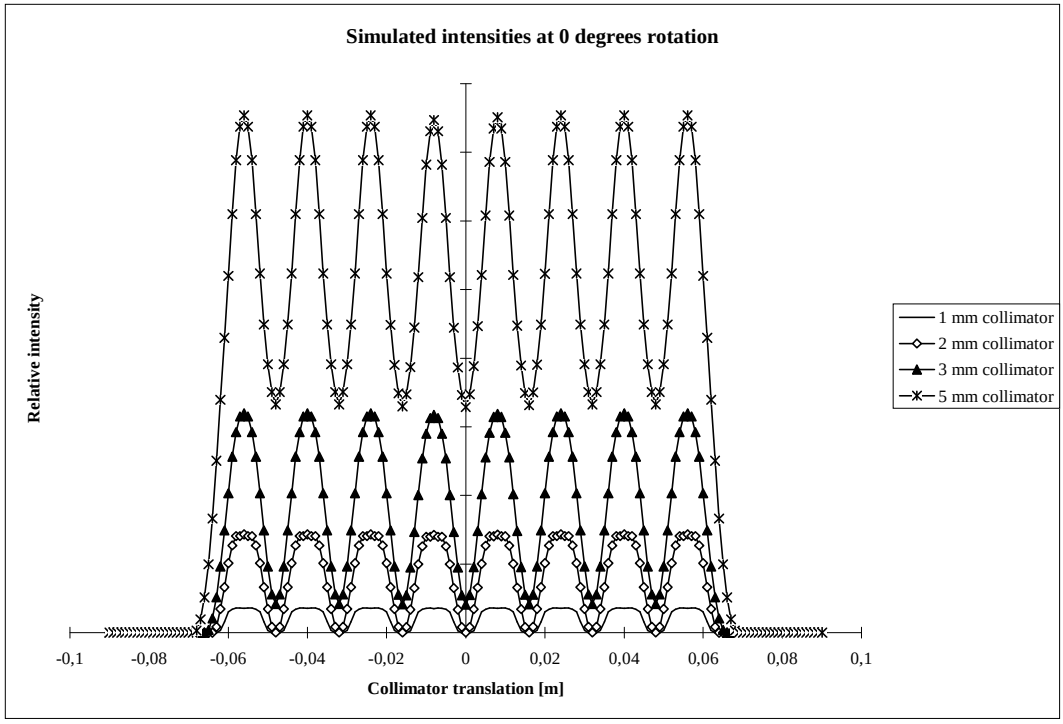

Figure 10.8. Simulated relative intensities at 0^o assembly rotation for four different collimator widths.

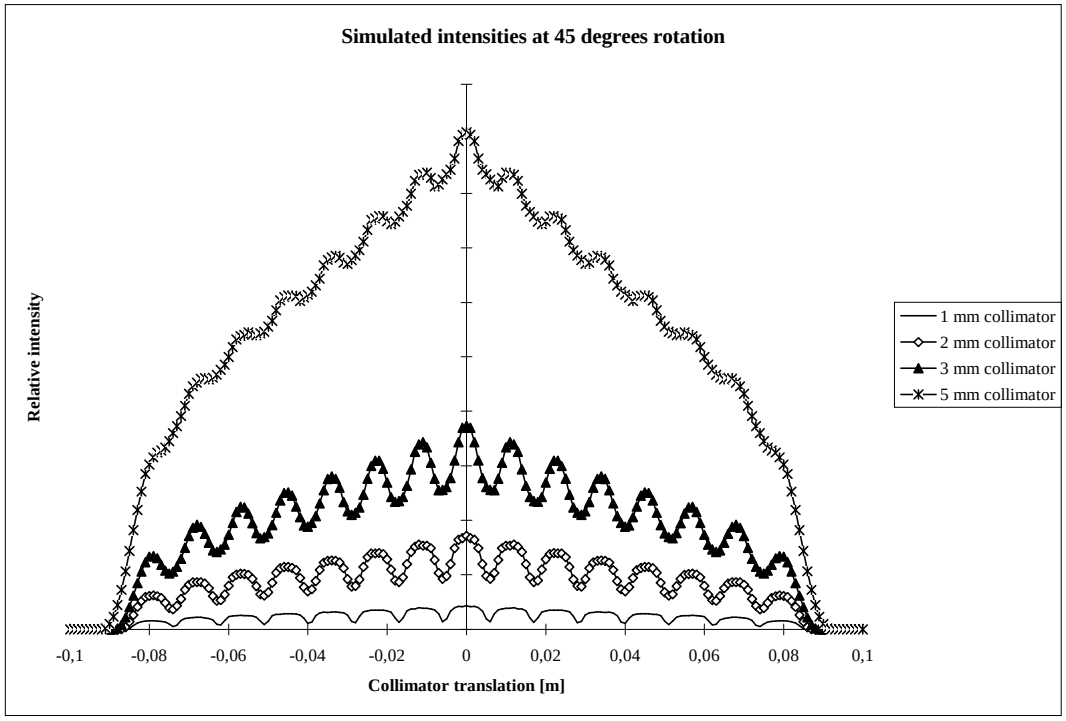

Figure 10.9. Simulated relative intensities at 45^o assembly rotation for four different collimator widths.

The water channel is hardly detectable by just studying the simulated intensities. The detection will be even harder for a real measurement including statistical noise. The intensity pattern is most distinct for the smallest values of the collimator width. For 45^o assembly rotation and a 5 mm collimator, the pattern is almost completely smeared out. As expected, the intensities are higher using wider collimators.

Appendix 5. Examples of reconstructed activity pictures

Iter 120, mean

948	926	935	931	942	932	931	945
919	938	937	931	945	955	923	933
928	967	900	932	932	919	907	936
937	933	899	992	927	958	915	932
934	904	999	906	11	882	940	931
947	935	947	912	962	938	950	940
935	921	905	970	938	942	929	930
934	936	942	932	927	936	926	941

Pixel value 999 is above equal to: 88232267.653

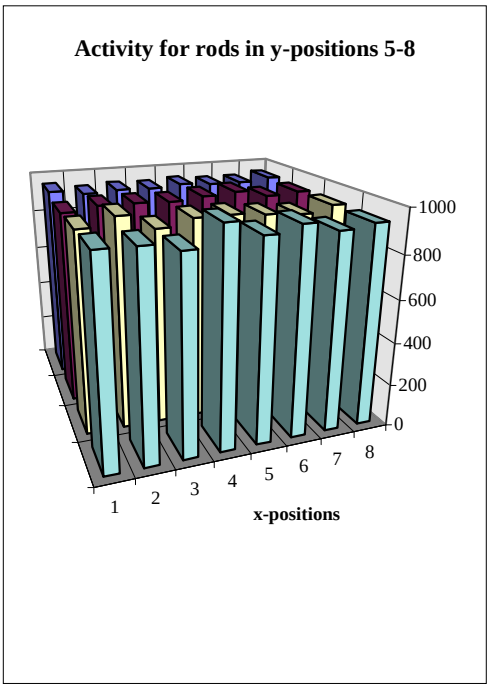

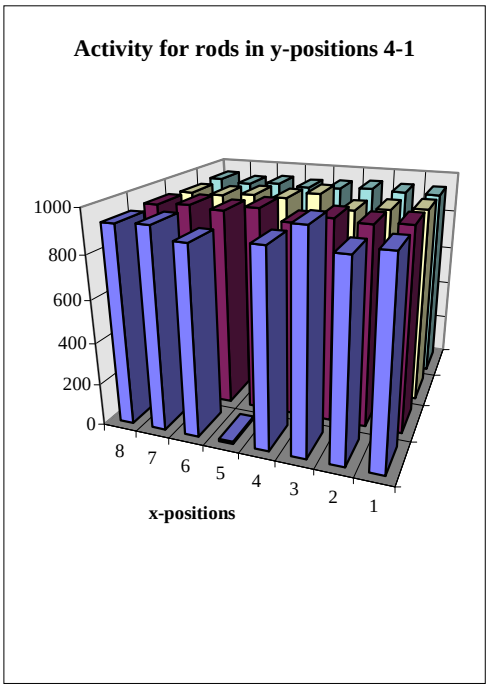

Average of all but (4,5):	934,2222
Value of (4,5):	11
Standard deviation for all but (4,5):	19,30659
Standard deviation for all but (4,5):	2,1%
Ratio of (4,5) to average of others:	1,2%
Ratio of (4,5) to minimum of others:	1,2%
Minimum of all but (4,5):	882
Ratio of minimum to average, (4,5) excluded:	94,4%
Maximum of all but (4,5):	999
Ratio of maximum to average, (4,5) excluded:	106,9%

Figure 10.10. Reconstruction EAC_Cs31_11_18.
Reconstructed using simulated intensities from "Simul_Cs3_spec".
28 projections and 40 translations.
The EAC algorithm, 120 iterations with relaxation parameter 0,05.
Attenuation calculated using the method of stepping through the assembly.

Iter 120, mean

949	926	938	932	943	933	934	946
921	939	937	933	947	959	924	934
929	970	903	932	937	921	907	939
938	934	903	995	930	958	918	933
935	907	999	909	17	886	941	932
950	934	950	917	962	941	954	940
936	922	908	971	940	943	930	932
935	938	942	933	927	939	927	942

Pixel value 999 is above equal to: 88219235.826

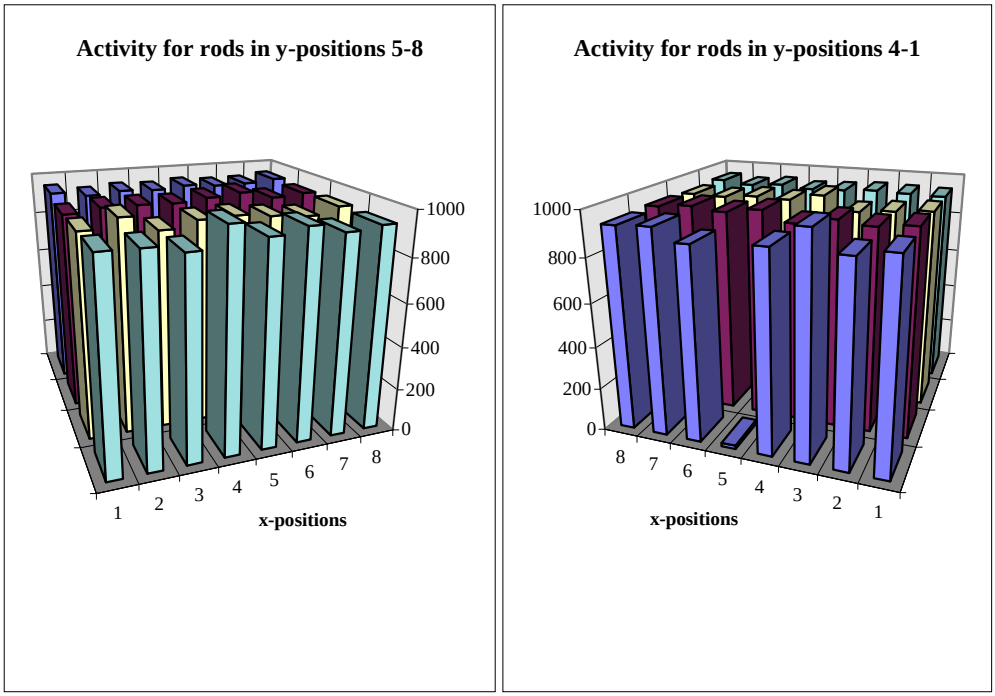

Average of all but (4,5):	935,9365
Value of (4,5):	17
Standard deviation for all but (4,5):	19,01033
Standard deviation for all but (4,5):	2,0%
Ratio of (4,5) to average of others:	1,8%
Ratio of (4,5) to minimum of others:	1,9%
Minimum of all but (4,5):	886
Ratio of minimum to average, (4,5) excluded:	94,7%
Maximum of all but (4,5):	999
Ratio of maximum to average, (4,5) excluded:	106,7%

Figure 10.11. Reconstruction "EAC_Analyt".
Reconstructed using simulated intensities from "Simul_Cs3_spec".
28 projections and 40 translations.
EAC algorithm, 120 iterations with relaxation parameter 0,05.
Attenuation calculated using the analytic method.

Iter 40, mean

780	778	776	774	781	778	769	790
799	749	801	795	780	781	781	789
745	844	738	759	862	718	843	757
834	656	849	816	649	963	673	812
720	944	556	790	88	714	836	761
857	586	999	677	823	705	792	783
716	923	642	894	721	822	757	782
841	710	841	735	802	764	792	777

Pixel value 999 is above equal to: 102345759.556

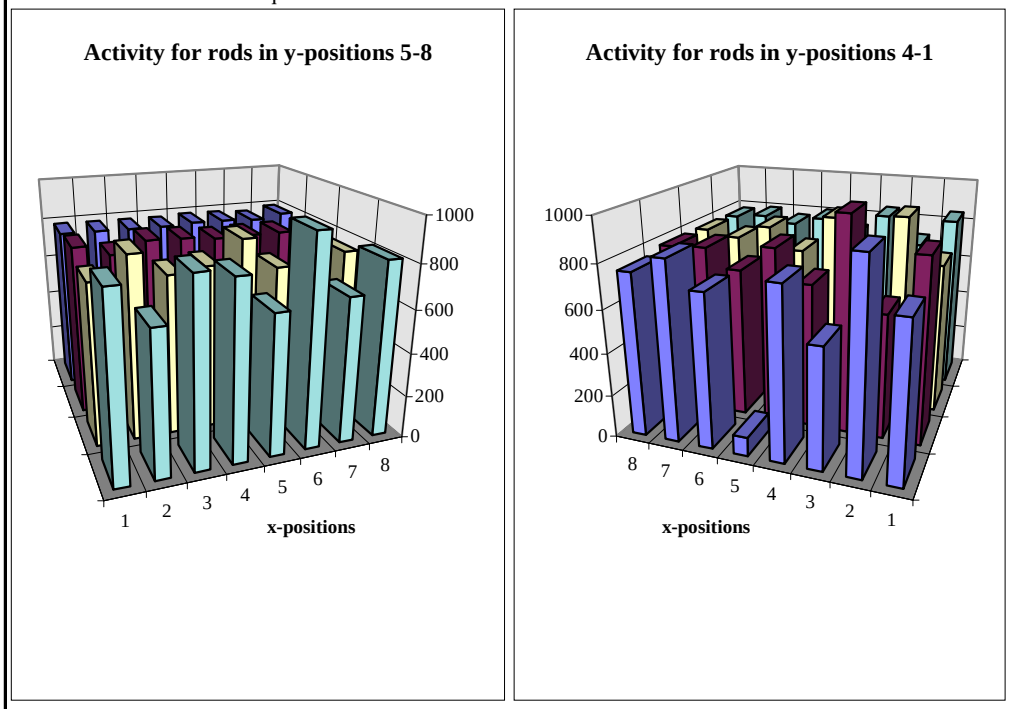

Average of all but (4,5):	779,0635
Value of (4,5):	88
Standard deviation for all but (4,5):	78,51516
Standard deviation for all but (4,5):	10,1%
Ratio of (4,5) to average of others:	11,3%
Ratio of (4,5) to minimum of others:	15,8%
Minimum of all but (4,5):	556
Ratio of minimum to average, (4,5) excluded:	71,4%
Maximum of all but (4,5):	999
Ratio of maximum to average, (4,5) excluded:	128,2%

Figure 10.12. Reconstruction EAC_Cs51_11_01, example of a reconstructed activity picture not fulfilling the demands of section 2.6..
Reconstructed using simulated intensities from "Simul_Cs5".
60 projections and 30 translations. $\Phi(0) = 3^o$.
EAC algorithm, 40 iterations with relaxation parameter 0,05.

Iter 150, mean

972	959	958	955	959	963	959	971
947	950	957	964	957	970	957	967
960	972	948	950	917	968	951	957
961	957	929	993	999	955	966	955
952	954	979	947	581	917	944	961
957	971	940	961	954	964	964	966
971	953	957	970	954	963	963	961
962	963	957	962	956	962	954	961

Pixel value 999 is above equal to: 86934315.629

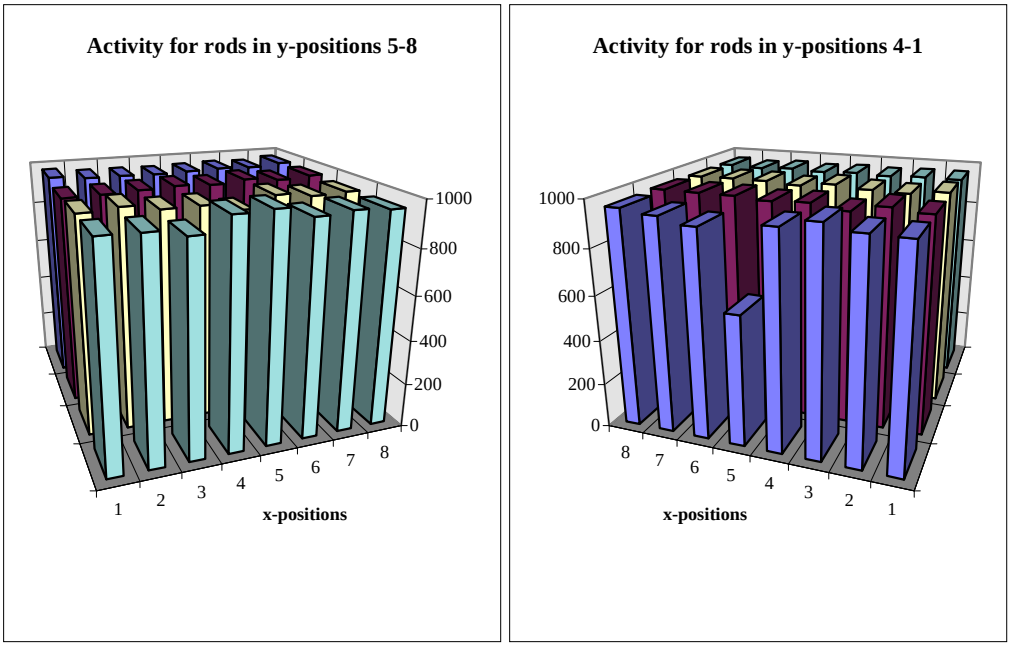

Average of all but (4,5):	958,77778
Value of (4,5):	581
Standard deviation for all but (4,5):	12,921551
Standard deviation for all but (4,5):	1,3%
Ratio of (4,5) to average of others:	60,6%
Ratio of (4,5) to minimum of others:	63,4%
Minimum of all but (4,5):	917
Ratio of minimum to average, (4,5) excluded:	95,6%
Maximum of all but (4,5):	999
Ratio of maximum to average, (4,5) excluded:	104,2%
Average of all but (4,5) and corners:	958,25424
Standard deviation for all but (4,5) and corners:	13,124687
Standard deviation for all but (4,5) and corners:	1,4%
Ratio of (4,5) to average of others except corners:	60,6%

Figure 10.13. Reconstruction CAC_Cs31_113, example of a reconstructed activity picture without rotation or translation displacements.
Reconstructed using simulated intensities from "Simul_Cs3_spec".
24 projections and 40 translations.
CAC algorithm, 150 iterations with relaxation parameter 0,50.

Iter 150, mean

975	34	28	34	50	62	54	999
54	76	81	72	77	71	77	34
62	71	84	87	72	86	81	28
50	77	73	109	108	86	73	35
34	71	88	102	78	71	76	50
28	82	84	76	87	86	70	63
34	75	70	78	71	82	77	55
963	55	62	50	35	28	34	981

Pixel value 999 is above equal to: 1249957555.574

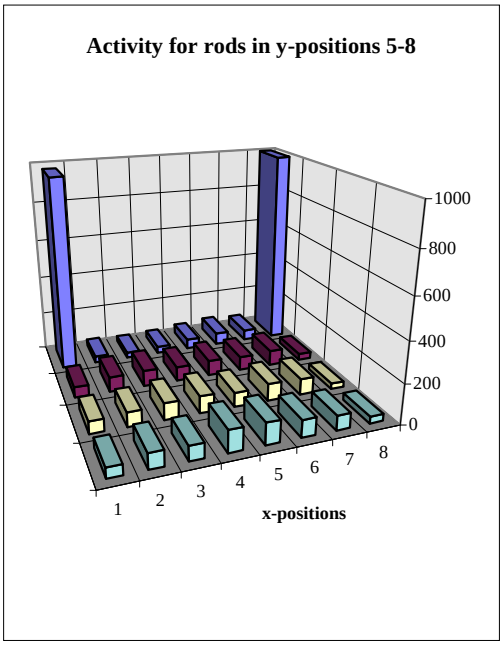

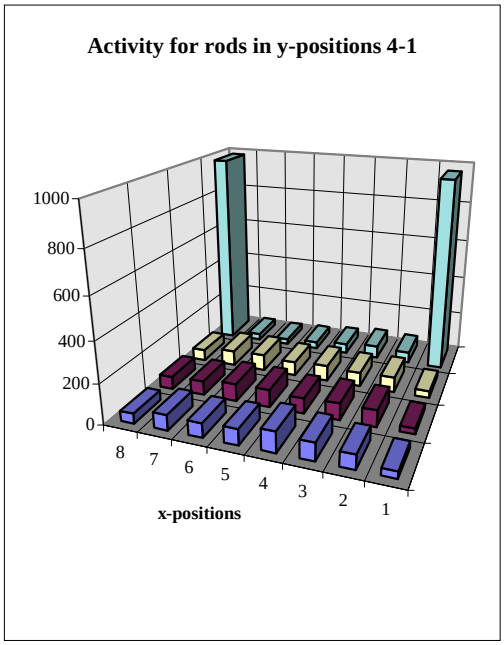

Average of all but (4,5):	123,46032
Value of (4,5):	78
Standard deviation for all but (4,5):	223,83638
Standard deviation for all but (4,5):	181,3%
Ratio of (4,5) to average of others:	63,2%
Ratio of (4,5) to minimum of others:	278,6%
Minimum of all but (4,5):	28
Ratio of minimum to average, (4,5) excluded:	22,7%
Maximum of all but (4,5):	999
Ratio of maximum to average, (4,5) excluded:	809,2%
Average of all but (4,5) and corners:	65,423729
Standard deviation for all but (4,5) and corners:	20,933473
Standard deviation for all but (4,5) and corners:	32,0%
Ratio of (4,5) to average of others except corners:	119,2%

Figure 10.14. Reconstruction CAC_Cs31_117, reconstructed activity picture with 2 mm translation and 1^{o} rotation displacement.
Reconstructed using simulated intensities from "Simul_Cs3_spec".
24 projections and 40 translations.
CAC algorithm, 150 iterations with relaxation parameter 0,50.

Iter 150, mean

708	718	722	685	663	649	642	714
642	652	667	650	636	671	661	719
646	675	724	729	716	740	664	718
665	642	728	999	990	725	656	688
683	645	746	928	703	709	635	663
720	680	720	754	737	740	667	651
720	651	667	652	643	674	661	644
707	648	646	664	687	721	712	706

Pixel value 999 is above equal to: 135270260.402

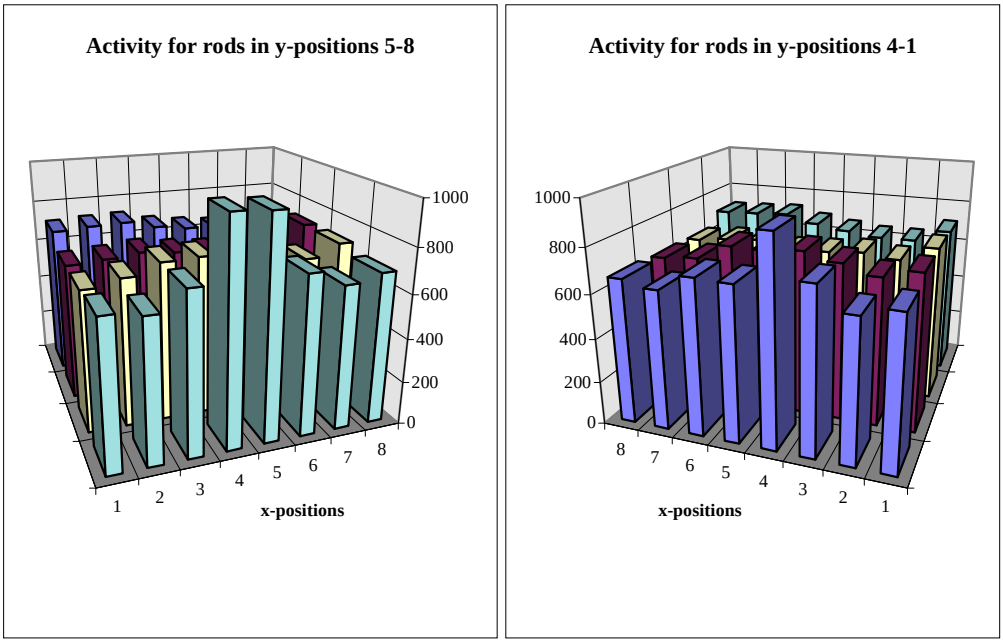

Average of all but (4,5):	698,1746
Value of (4,5):	703
Standard deviation for all but (4,5):	70,226513
Standard deviation for all but (4,5):	10,1%
Ratio of (4,5) to average of others:	100,7%
Ratio of (4,5) to minimum of others:	110,7%
Minimum of all but (4,5):	635
Ratio of minimum to average, (4,5) excluded:	91,0%
Maximum of all but (4,5):	999
Ratio of maximum to average, (4,5) excluded:	143,1%
Average of all but (4,5) and corners:	697,45763
Standard deviation for all but (4,5) and corners:	72,507702
Standard deviation for all but (4,5) and corners:	10,4%
Ratio of (4,5) to average of others except corners:	100,8%

Figure 10.15. Reconstruction CAC_Cs31_122, reconstructed activity picture with 2 mm translation and 1^{o} rotation displacement, only central translations used.
Reconstructed using simulated intensities from "Simul_Cs3_spec".
24 projections and 40 translations.
CAC algorithm, 150 iterations with relaxation parameter 0,50.